Experiments with a Separated Beam Atom Interferometer

by

Christopher Russell Ekstrom

B.S. Physics, University of Washington (1988)

Submitted to the Department of Physics in
partial fulfillment of the requirements
for the degree of

Doctor of Philosophy

at the

Massachusetts Institute of Technology

September, 1993

© Massachusetts Institute of Technology, 1993
All rights reserved.

Signature of the Author _____
Department of Physics
September 1993

Certified by _____
David E. Pritchard
Professor of Physics
Thesis Supervisor

Accepted by _____
George F. Koster
Chairman, Department Committee
on Graduate Studies

Science
MASSACHUSETTS INSTITUTE
FEB 08 1994

Experiments with a Separated Beam Atom Interferometer

by

Christopher R. Ekstrom

Submitted to the Department of Physics
on September, 1993, in partial fulfillment of the
requirements for the degree of Doctor of Philosophy

Abstract

Several experiments have been performed with an atom interferometer built from three 200 nm period amplitude diffraction gratings arranged into a Mach-Zender geometry. The interfering beams are physically isolated from each other with a metal foil.

The first experiment is a measurement of the electric polarizability of the ground state of sodium. This produced a result that is a factor of six more accurate than previous experimental work. The second experiment is a spin rotation experiment performed with the ground Zeeman states of the sodium atom. A final separated beam experiment is a scattering experiment where a gas target is inserted into one of the beams of the interferometer. The forward scattering of the beam that travels through the target represents the complex index of refraction of the gas for matter waves.

The near field imaging of amplitude diffraction gratings is investigated with the sodium beam and two of the diffraction gratings. This is the atom optics analog of the Talbot effect.

The final experiment described in this thesis is the preparation and diffraction of an intense molecular beam of sodium dimers.

Thesis Supervisor: Dr. David E. Pritchard
Title: Professor of Physics

To

Gretchen, Janice, and Philip

pity this busy monster, manunkind

not. Progress is a comfortable disease:
your victim(death and life safely beyond)

plays with the bigness of his littleness
-electrons deify one razorblade
into a mountainrange;lenses extend

unwish through curving wherewhen till unwish
returns on to itself.
A world of made
is not a world of born-pity poor flesh

and trees,poor stars and stones,but never this
fine specimen of hypermagical

ultraomnipotence. We doctors know

a hopeless case if-listen:there's a hell
of a good universe next door;let's go

-e. e. cummings

Table of Contents

Symbols used in this thesis

The following is a list of the symbols used in this thesis. I have tried to make symbol definitions consistent throughout the document. The included papers, however, may use different conventions.

p	diffraction grating period
λ_{dB}	de Broglie wavelength
m	mass
v	velocity
θdiff	diffraction angle
θ_i	i^{th} grating rotation angle
C	contrast
	generic constant
h_i	height of i^{th} grating
x_i	transverse position of i^{th} grating
y_i	vertical position on i^{th} grating
φ	phase
a	arbitrary parameter
P(a)	distribution function of a
Ω	angular rotation of interferometer
k	wave vector of the atom
k_0	wave vector of the atom in the absence of a potential
U(x)	a spatially dependent potential
E	energy of the atom
	electric field
T(dx)	spatial translation operator
α	electric polarizability
b	classical impact parameter
$\Delta(b)$	semiclassical phase shift at impact parameter b
z	axial coordinate in machine and scattering problems
β	open fraction of a diffraction grating
l	distance between gratings
d	source to first grating distance
s	separation of diffracted beams at the detector
n	diffraction order number
N	normalization constant

Introduction

In this introduction I will attempt to set the stage for this thesis. I will discuss a little of the history of interferometers in general, and atom interferometers in particular. I will give a list of the interferometer experiments that have been carried out in other labs in the second section. The last section will be a short list of the experiments we have performed with our interferometer, and the other atom optics experiments that will be covered in this thesis.

I.1 A little history

I will now give a brief history of interference experiments with an emphasis on ones that impact or foreshadowed atom interferometers.

Previous Interferometers

Many different types of optical interferometers were demonstrated shortly before the turn of the century. They include devices by Fizeau [FIZ62], Fabry and Perot [FAP99], and Michelson [MIC82]. These devices had an immediate and far ranging application in several areas of experimentation. A classic example is the experiment by Michelson and Morley [MIM87].

With the revelations of wave-particle duality contained in quantum mechanics, the paradigm for thinking about matter wave interferometers had arrived. Matter wave interference was in some sense discovered then, with the realization that amplitudes of matter states had to be added coherently, giving rise to interference terms. A simple example is single slit, double slit or multiple slit diffraction.

The first matter wave interferometer realized in the lab used electrons as the interfering particles. Two such devices were demonstrated nearly

simultaneously in 1954. One device used a three crystal geometry [MSS54]. In the paper describing this interferometer, it was argued that building a Young's two slit interferometer with electrons would be "almost impossible". Ironically, just such a device was demonstrated later that year [MOD54], using a single wire biprism.

The first neutron interferometer was demonstrated in 1962 [MAS62]. This was a biprism made out of glass, and was not used for much else but the demonstration. Although several different types of neutron interferometers have been demonstrated, the real workhorse of neutron interferometry is the perfect crystal interferometer [RTB74]. This type of interferometer uses three silicon crystals, usually parts of the same monolithic piece of single crystal silicon. There have been many experiments performed with these devices. These include: coherent spinor rotation [RZB75], measurement of the Sagnac effect using the earth's rotation[WSC79], gravitationally induced phase shifts [COW75].

The extensive work with neutrons in particular has provided much of the ground work for how to think about atom interferometers, and good ideas about what to do with them.

Atom Interferometers

Diffraction of He and H_2 off of LiF surfaces was first observed in 1930 [ESS30]. The first atom interferometers were demonstrated in the last few years.

There have been three demonstrations that rely on microfabricated structures as diffractive elements. A Young's double slit experiment was realized with a supersonic atomic beam of metastable helium atoms [CAM91] and later with metastable neon atoms dropped from a magneto-optical trap [SST92]. In addition, our group demonstrated a three grating atom interferometer [KET91] with much the same topology as the three crystal electron and neutron interferometers. There is another type of three grating interferometer that relies on the near field imaging of amplitude gratings [CLA92].

Several other interferometers have been demonstrated that rely on light forces to split, redirect, and recombine an atomic beam. Three Raman pulses ($\pi/2,\pi,\pi/2$) were used to demonstrate an interferometer with a tossed ball of atoms from a magneto-optical trap [KAC91]. The same group has also

implemented a four zone interferometer with a tossed magneto-optical trap[WEI93]. Two groups have demonstrated interferometers that are based on four traveling wave laser interaction regions with an atomic beam [RKW91,SSM92]. One of these groups [ERT93] has also implemented a similar temporal interferometer in a magneto-optical trap.

Recently it has become common to consider experiments using the separated gyrating or oscillating fields technique of Ramsey as longitudinal interferometers. A device of this type has been demonstrated with metastable helium atoms [MPV91].

I.2 What have atom interferometers been used for?

Atom interferometers have several things going for them. They have much shorter wavelengths than optical interferometers, and typically much longer transit times. They also have easily addressable internal structure in the interfering particles.

There are several problems with atom interferometers as well. The beam splitters typically impart small transverse momentum changes to the atom. This implies either very small diffraction angles, or the use of very slow atoms. There is also no achromatic beam splitter for atoms analogous to the partially silvered mirror for light, where the splitting angle does not depend on velocity.

The short wavelength and long transit times of atom interferometers have been exploited in two experiments in Steven Chu's laboratory at Stanford. The first of these experiments uses stimulated Raman transitions [KWR91] as ground state to ground state beam splitters in a three pulse interferometer. This experiment demonstrated impressive sensitivity to little g, the local acceleration of gravity [KAC91, KAS92]. In another experiment, a four zone type interferometer (with additional π pulses added) demonstrated impressive precision in measuring the recoil shift of an atom emitting a photon [WEI93]. This experiment could be used to determine plank's constant divided by the mass of the atom.

The group at PTB has demonstrated the sensitivity of their interferometer to rotations, and has found qualitative agreement with theory [RKW91]. Their entire apparatus was rotated at up to .1 Hz.

The group at Bonn has shifted the fringes in their interferometer through the differential Stark shift of the calcium intercombination line [RSS93]. They verified the quadratic dependence of the phase shift on the field, and measured the differential polarizability to 12%.

The group in Tokyo has shifted the fringes of their Young's double slit experiment with a gradient electric field [SST92].

I.3 What have we done?: outline of this thesis

This brings us to what we have done with our interferometer. That is the subject of this thesis. In chapter one I will describe the interferometer geometry, the apparatus, and the construction of the diffraction gratings. The second chapter describes the experimental procedures and data analysis required to run the interferometer. The third chapter will provide a brief introduction to the theory needed to deal with analyzing the various experiments.

Chapter four describes the first experiment we performed with the interferometer, a measurement of the ground state polarizability of sodium. The core of this chapter is a paper that has been submitted to Physical Review Letters. Chapter five covers an experiment we have named magnetic rephasing. This is the coherent rotation of all of the projections of a spin 2 and a spin 1.

The sixth chapter describes a measurement of the index of refraction of a gas for matter waves. The matter waves in question are in one of the separated beams of the interferometer.

Chapter seven and eight deal with topics outside of basic atom interferometery. Chapter seven deals with a study of the near field imaging of amplitude diffraction gratings called the Talbot effect. Our first results in molecular optics are covered in chapter eight.

Chapter nine is a short shopping list of future experiments for the interferometer.

1 The device and apparatus

In this chapter, I will discuss the experimental apparatus and the basic form of the interferometer. The apparatus has been reviewed recently in the most recent thesis from this experiment [KEI91] and I will therefore give only a rough outline of the device, with more detail applied to portions that have since been improved, rebuilt, or replaced.

1.1 The interferometer

Geometry

The interferometer has a Mach-Zender geometry, and is based around three microfabricated diffraction gratings. These three gratings are spaced evenly down the beam line and are used as beam splitters and mirrors. A basic drawing of the interferometer appears in Figure 1.1.

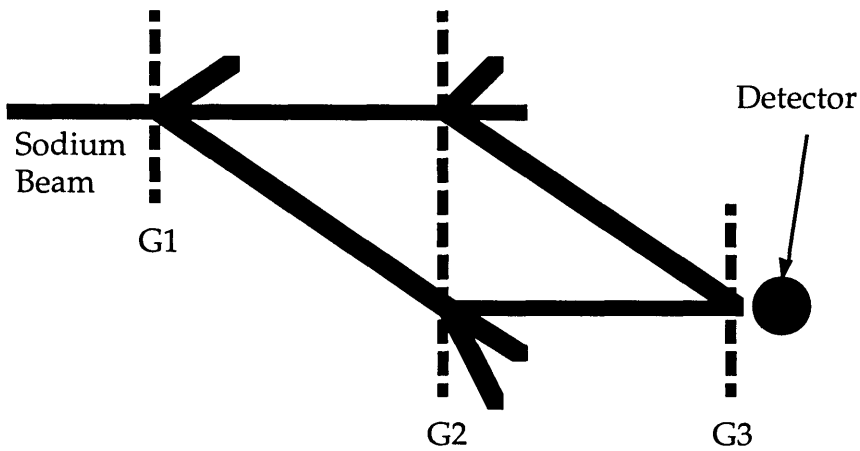

Figure 1.1: The basic geometry of the interferometer.

A beam of sodium atoms is produced by a seeded supersonic source using argon as a carrier gas. Two 20 micron wide slits collimate the beam with a

divergence of 24 milliradians. The typical mean velocity of the beam is 1050 m/s, with a 3.4% velocity width.

The beam is then diffracted by a 200 nm period amplitude diffraction grating. The diffraction angle between orders is 83 microradians. These gratings are formed from holes cut in a thin silicon nitride film. The first grating acts as a beam splitter, the zeroth and first orders of which are used in the interferometer. The second grating intercepts the two split beams and acts as the two mirrors. The first diffracted order of the zeroth order beam and the minus-first diffracted order of the first order beam are directed towards each other. These two beams intersect at the plane of the third grating. The intersecting beams produce a spatial modulation of the beam intensity across the beam that has the same period as the diffraction gratings. This is illustrated in Figure 1.2.

Because the gratings are amplitude transmission structures, we can use the third grating as a mask to detect the interference pattern. By changing the relative position of the third grating with respect to the first and second, and observing the total transmitted intensity through the third grating, we can map out this interference pattern. The atoms are detected by surface ionization on a 50 micron wide hot wire detector.

The properties and production of the diffraction gratings are described in section 1.3.

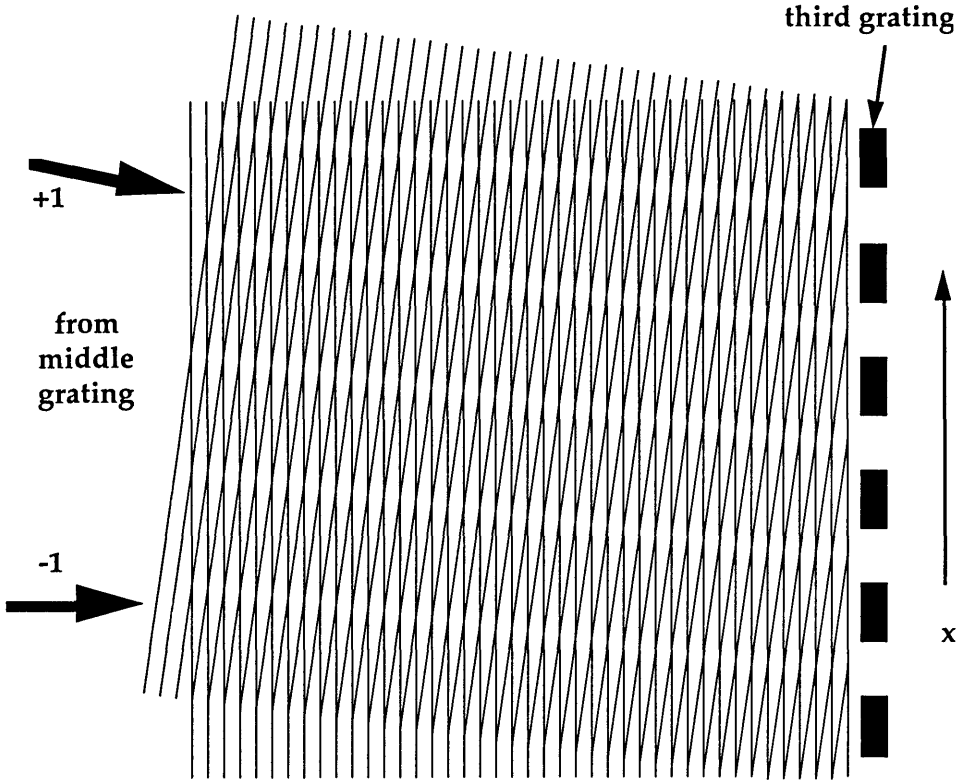

Figure 1.2: Phase fronts from the two interfering beams intersecting at the plane of the third grating. By translating the third grating with respect to the interfering beams, the transmitted intensity oscillates.

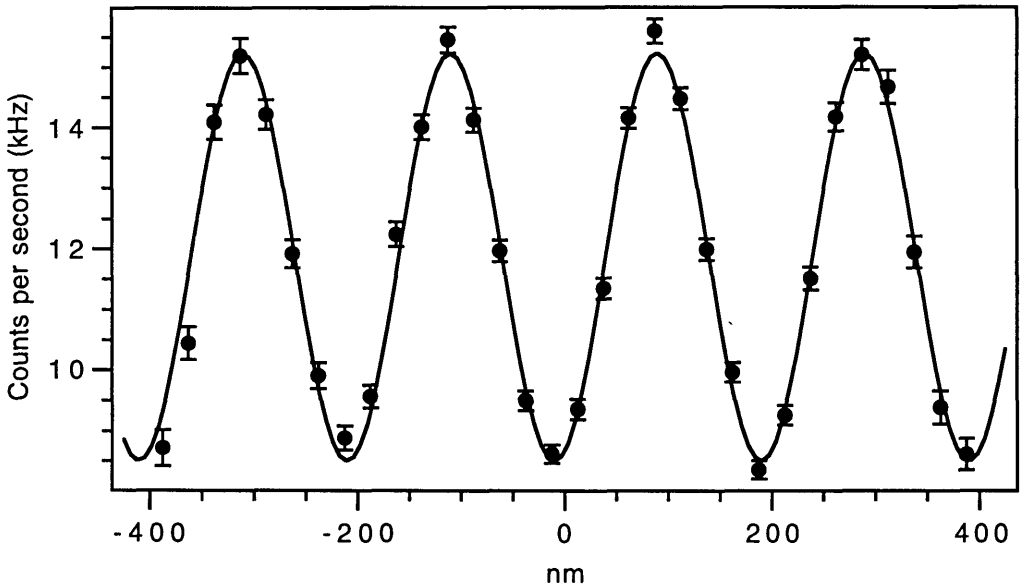

Figure 1.3: Interference fringes from 20 seconds of data. Each point represents 1/2 second of data. The fit to the interference fringes allows us to determine the phase of the interference pattern to 6 milliradians in 1 minute.

Theoretical implications

Most of the theoretical implications of this interferometer geometry are spelled out in [CAL75]. The most important one is that since the path length difference is zero for the central fringe appears at the same position for all velocities, or "colors"; this is called a white fringe. It is easy to see that all velocities will produce the same period fringes at the plane of the third grating. The angle between the two beams as they approach the third grating is the same as the diffraction angle from the first grating. Because for a given velocity, the diffraction angle is set by the grating period and the de Broglie wavelength, if two beams intersect with that angle and deBroglie wavelength, they should produce fringes with the same period as the original diffraction grating. This is true irrespective of the velocity. The fact that, while the envelope of the beam shifts with velocity, the location of the fine fringes within that envelope do not, has no simple model. Checking whether this was the case was the original motivation for the numerical modeling of the interferometer described elsewhere [KEI91,TUR91,TPK92].

1.2 The atomic beam machine

The atomic beam is produced by a seeded supersonic source with argon used as the carrier gas. The beam is collimated and ultimately detected on a hot wire detector.

Source

The source has been replaced with one that is similar in spirit, but with a much more robust implementation. The basic principle is that sodium metal is contained in a stainless steel box with an argon inlet that maintains two atmospheres of pressure. The box is heated to around 700 Celsius (~20 Torr of sodium). The argon and sodium mixture expands through a 70 micron diameter hole into vacuum, producing a supersonic expansion. A skimmer is placed after the nozzle, inside the shock wave, forming a typical seeded supersonic source.

The entire source and source flange have been replaced. The source is hung from a flange mounted on the end of the source chamber. The source can be moved on a three point "optics mount" from outside which allows alignment with the beam skimmer (Beam Dynamics model 1, 0.5 mm orifice)

and control of the nozzle-skimmer distance. The 70 micron nozzle is produced by Apertura, a small local company.

The entire stainless steel source envelope is either swaged or welded together. Elimination of the brazing on the previous source allows higher temperatures without worrying that the source will explode at any moment. The current design should be capable of operation up to 1000 Celsius, the limit of the heaters (Aerorod coaxial heaters). All of the thermocouples have been replaced with ARI coaxial thermocouples, which are much more reliable than the spot welded thermocouples used previously.

The argon carrier gas handling system has also been altered. There are now two gas purifiers between the gas bottle and the source. They were introduced because of worries about contamination of the sodium in the source by water and oxygen, both of which will form sodium oxides in the oven. At high temperatures, sodium oxides are quite corrosive, and will eat stainless steel. In the old source, the stainless steel gas inlet lines have been known to completely corrode away inside the oven. The conversion to oxides also uses up sodium, may reduce the amount of clean sodium surface producing sodium vapor in the oven, and may cause the nozzle or gas inlet to clog.

The first purifier is a heated getter (Supelco high capacity gas purifier #2-3800) that pumps out water and oxygen very efficiently but does not pump argon. This is the same material that is used in high vacuum getter pumps. One getter element should last for about 10 cylinders of 99.995% pure argon.

The second purifier is a glass tube filled with chemicals that react with oxygen and water (Supelco OMI-1 indicating purifier). This has the advantage of changing color when the chemical charge is spent, telling us that it and the first purifier need to be refreshed. This is no small advantage, because if you have to remember to change the first purifier's charge after 2 years, it just won't happen (for proof, look at the rough pump trap elements and water filters in the lab).

The combination of the two purifiers yields argon that has water and oxygen impurities of a few ppb. The source recently ran out of sodium and had to be refilled. When the oven was opened, the inside was very clean and there was no evidence of corrosion.

Vacuum system

The vacuum system is largely unchanged from David Keith's thesis [KEI91] and I will only give a brief outline of its form to provide landmarks for subsequent discussions of the machine. A rough schematic of the vacuum system is shown in Figure 1.4.

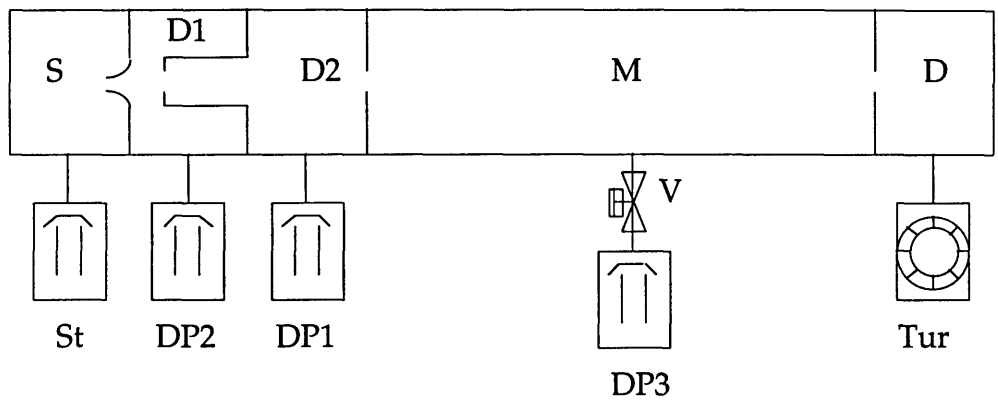

Figure 1.4: The vacuum system. The five differentially pumped chambers are, in order: source (S), differential chamber 1 (D1), differential chamber 2 (D2), main chamber (M), and the detector chamber (D). The pumps for each chamber are described in the text. The pneumatic gate valve (V) is shown above the main chamber diffusion pump.

The vacuum envelope consists of five differentially pumped chambers. The first chamber houses the atomic beam source. It is pumped by a high throughput diffusion pump (4" Stokes model 150, 500 l/s). The argon load from the source into this chamber is ~0.5 Torr l/s, giving a typical pressure of several to 10 microns. The aperture into the next chamber is a beam skimmer (Beam Dynamics model 1) that allows roughly 0.3% of the gas load from the source into the first differential pumping chamber.

The next two chambers provide differential pumping. The first differential pumping chamber is pumped by a NRC 10" unbaffled diffusion pump (4,200 l/s). The pressure is typically 1-3x10^{-6} Torr. The beam travels in this chamber for only about 20 cm. The opening into the second differential pumping chamber is the first collimation slit (20 μm x 3 mm).

The second chamber is pumped by a 4" diffusion pump (800 l/s) hung from a water cooled elbow. The pressure is typically 5-9x10^{-7} Torr, and the beam is in

this chamber for 50 cm. The aperture into the main chamber is ~1 cm and can be sealed with a homemade Plexiglas gate valve.

The main chamber is ~150 cm long and contains the second collimation slit and all of the rest of the interferometer except the detector. The vacuum system for this chamber is discussed in the next section, and gives typical pressures of 1-3x10^{-7} Torr. The aperture into the detector chamber is ~1 cm and can also be sealed with a homemade Plexiglas gate valve.

The detector chamber is pumped with a Varian V80 turbo pump and also has a liquid nitrogen pumping surface. The combination gives pressures of 2-5x10^{-8} Torr. The turbo pump is hung by its own weight on a 6" conflat vacuum bellows to reduce vibrations transferred to the machine.

main chamber

The main chamber vacuum system has been improved in three ways: new pumping fluid in the diffusion pump, a pneumatic gate valve over the pump, and a new pumping strategy designed to minimize back streaming into the chamber.

Previously, the canonical pumpdown strategy was as follows: rough out the chamber with the roughing pump through the diffusion pump until a pressure of about 50 milliTorr (long rough times up to a day were thought to be acceptable), turn on the diffusion pump and let it start up, then pump the chamber down to high vacuum. There are several things wrong with this prescription. The first is that at pressures below ~150 milliTorr, roughing pumps start to back stream significant amounts of rough pump oil. The second is that when starting up, a diffusion pump back streams a lot of diffusion pump oil. These facts, coupled with the fact that we had destroyed several sets of gratings by slowly clogging them with oil, necessitated a change.

An obvious solution to oil clogging the gratings is to use a turbo pump on the main chamber. We have not done this because we would need to use a very low vibration pump and isolate the vibrations from the machine. We have not done this because it would be expensive, and the new operating procedures allow better than one half of a year of operating time on a single set of gratings.

The first change was to move from DC704 diffusion pump oil to DC705, which has much lower base vapor pressure and back streaming rates. It is also one of the few oils that exhibits no "creep" along surfaces. The next was to install a pneumatic gate valve over the pumping stack (NRC 4" belly pump + chevron water baffle). The gate valve is powered by a dedicated nitrogen cylinder and has its own interlock controller. This controller is a latchable relay that must have line power, and a "true" signal from the diffusion pump interlock (temp + rough pressure + water flow). The gate valve will shut on a power failure, and will not reopen until a reset button is pushed on the front panel. This protects us from the all too frequent power failures at MIT.

The final change was a change in pump down procedure. The chamber is roughed out with a second mechanical pump with the gate valve closed, and the diffusion pump on. At a pressure of 200 milliTorr, the secondary roughing line is closed, and the gate valve is opened. This minimizes total back streaming into the chamber [OHA88], and has significantly extended the lifetime of a set of gratings in the main chamber. A recent set of gratings went from an open fraction of 45% to 23% over the course of 9 months of regular use.

Detector

There have been several improvements to the detector. These changes have been more in implementation than in concept. The hot wire alloy, bakeout regime, and oxygenation procedure have been changed. We have added a set of knife edges to limit the vertical height and alter the vertical location of the beam at the detector. Finally, we are using a more robust mounting system for a different model channeltron that requires lower voltages.

We are using a 50 micron diameter pure rhenium wire to ionize the sodium atoms. This has a higher melting point (3180 Celsius) than previous alloys such as Ir and Pt/Ir. This allows us to bake out the wire much hotter by heating it with a large current running through it, reducing the background and noise spikes.

The mounting system for the channeltron has been altered to accept a Galalieo model 4860 channeltron. This model comes well mounted on a plate and requires a lower voltage of 2.4 kV. The charge amplifier/pulse

height discriminator/line driver electronics (Amptek model A101) has been moved outside of the detector chamber in an effort to clean up the vacuum.

I will now describe the current theory on how the bakeout process works. The wire comes with a large number of impurities not only on the surface, but also in the bulk. The bakeout quickly removes the surface impurities. The bulk impurities diffuse out of the wire over a longer time scale of days. By baking out at a higher temperature, the bulk impurities near the surface are heavily depleted. The temperature is then stepped down to the final operating temperature in several stages.

The oxide layer on the wire appears to be unstable for a bakeout current above 250 mA in our 50 μm wire. This is a problem because the oxide has a larger work function than the bare metal and leads to more efficient ionization of the sodium atoms. We replenish the oxide layer by leaking pure oxygen (Matheson grade, 99.997%) to a detector chamber pressure of $1\text{-}2\text{x}10^{-5}$ Torr, with the wire at 200 mA for 1 minute.

After a bakeout and replenishing the oxide layer, we have seen wires with less than 1 ms time responses and background count rates of only 10 cps. I must admit that much of the wire preparation is based on "feel" and black magic. A great method for producing good wires may not work next year, and "the last word" in detector wire alloys has been spoken many times.

1.3 The diffraction gratings

The basic grating construction method has not changed from when it was developed by David Keith [KEI91]. I went to the National Nanofabrication Facility at Cornell University in October of 1991 to build more gratings. These gratings were used in all of the work described in this thesis. The goals of the construction run were to produce finer period gratings and to optimize the process for greatest grating coherence. The grating coherence is the regularity the structure; it must have the same period and have parallel bars over the entire grating. A paper that appeared in Applied Physics B concerning grating construction and atom optics with nanofabricated structures follows.

Atom Optics Using Microfabricated Structures

Christopher R. Ekstrom, David W. Keith, and David E. Pritchard

Department of Physics, and

Research Laboratory of Electronics, MIT

Cambridge, MA 02139

We present a novel method for fabricating precisely positioned small openings in thin silicon nitride membranes. Several optical elements for atoms have been constructed, including amplitude diffraction gratings and zone plates, and the results of experiments using these devices are presented. A method for creating a blazed diffraction grating is discussed.

Atom optics[1, 2] refers to two things: a new point of view in which atoms in atomic beams are thought of and manipulated like photons in light beams, and a growing collection of techniques and devices for performing this manipulation. While some demonstrations of atom optics are over 20 years old - including diffraction of atoms from crystal surfaces[3], single slit diffraction[4], and hexapole focusing lenses[5, 6] - advances in laser and nanofabrication technology have lead to numerous recent demonstrations of various types of diffraction gratings[7, 8, 9] and zone plates[10, 11]. Other recent developments include the demonstration of atom mirrors using light and specially prepared surfaces[12, 13]. Recent theoretical developments suggest that momentum transfer by light offers several new possibilities for the construction of coherent beam splitters for atoms[14]. It now appears that the field of atom optics is developed well enough to allow the construction of devices containing several elements working together[15, 16].

This paper concerns optical elements for atoms made from thin membranes with precisely positioned openings for the atoms to pass through. These are

essentially amplitude transmission devices - the optical analog of holes cut in black paper. The short wavelength of atomic deBroglie waves demand sub-micron size holes, requiring the use of nanofabrication techniques. Although we have used both gold and silicon nitride nanofabricated devices, here we describe only techniques for the construction of the latter. Construction of the gold gratings has been described elsewhere by its originators[17, 18, 19, 20].

The first section of this paper describes details of the new fabrication process. The subsequent three sections discuss, in turn, the construction and performance of our atom diffraction gratings, a technique to employ electric fields to produce "blazed" diffraction gratings, and results from an imaging experiment using a zone plate. We conclude by offering several speculative comments about the future of atom optics using microfabricated structures.

1. FABRICATION

We have developed a fabrication technique to make thin (100-200 nm) silicon nitride membranes with precisely patterned holes of arbitrary shape. The membrane is stretched flat against the surface of a conventional 0.25 mm thick silicon wafer which has windows cut in it behind the patterned portions of the membrane. The pattern of holes is determined by an electron beam writer, and the overall process has been used to make patterns with minimum dimensions as small as 50 nm and overall pattern sizes up to 3 x 0.2 mm. An important feature of our fabrication process is that there are few limits to the pattern that may be written on the window except those imposed by the requirement that the membrane be self-supporting. The technique has been used to construct gratings with periods from 400 to 100 nm, as well as single slits, double slits, and cylindrical zone plates. All of the construction using this method was performed at the National Nanofabrication Facility at Cornell University.

Low stress silicon nitride membranes were chosen over gold and doped silicon as a structural material for several reasons. Gold has little structural strength, which is important for the construction of large scale, uniform structures. Fabrication of doped silicon films[21] requires a poisonous and corrosive silicon etch (ethylene diamine: pyrocatechol) and silicon epitaxial growth facilities. High stress films can distort or break when they are perforated. The tensile stress of silicon nitride films can be reduced

continuously from 1.2 GPa to less than 100 MPa by varying the growth parameters (the ratio of dichlorosilane to ammonia) of the low-pressure chemical vapor deposition (LPCVD) system[22] with some decrease in tensile strength; we used a stress of ~120 MPa, which virtually eliminated problems of ruptures during fabrication.

The fabrication begins (Fig. 1) with the deposition of low stress silicon nitride on both sides of a double polished <100> silicon wafer. The silicon nitride is deposited by low pressure chemical vapor deposition (LPCVD). A layer of standard optical photoresist is applied to what will be the back of the chip, and the pattern of windows is exposed on the wafer. After development, the nitride on the back is removed from the exposed areas of the wafer with a reactive ion etch (RIE) of CF_4.

The wafer is then immersed in hot KOH which etches each window entirely through the silicon wafer, leaving a suspended nitride "window pane" on the front of the wafer. This etch removes material with strong preference along certain crystal planes of the silicon, so the dimensions of the window on the front side of the wafer can be accurately controlled, provided the window pattern is aligned to the crystal planes of the substrate.

A 120 to 210 nm layer of Plexiglas (PMMA) is then applied to the front side of the wafer. To prevent distortions due to charging of the PMMA, a thin layer of gold is also evaporated onto the wafer. The e-beam writer (a JEOL JBX5DII) then writes the desired pattern into the PMMA. The areas in the PMMA that have been exposed by the e-beam writer have their molecular structure damaged, so they can then be washed away with a mixture of methyl isobutyl ketone (MIBK) and isopropanol (IPA). This leaves a pattern of PMMA that has not been exposed to the e-beam on the nitride window. Up to this point in the processing, all of the steps are standard, well known microfabrication techniques.

The new feature of our method is a direct process for transferring the PMMA pattern onto the nitride window. We have developed a reactive ion etch recipe[23] that etches nitride faster than PMMA, so we can use the PMMA as a mask when etching through the nitride window. Using reactive ion etching techniques is essential since wet chemical processes etch non-directionally

and can also damage the structures due to forces from surface tension. The residual PMMA is then removed in an oxygen reactive ion etch.

The principal advantage of this procedure is that the pattern transfer to the membrane is performed in one step. This increases reliability, shortens processing time, and yields higher resolution. Other pattern transfer techniques, such as lift-off, which require a transfer of the pattern using a metal coating as an intermediary, are more complicated, and provide a less direct transfer of the pattern.

There are several difficulties when writing large area gratings with electron beam writing. When writing larger area gratings, it is hard to keep the grating bars parallel and the period constant over the entire area. The e-beam writer writes large area patterns by writing small fields (~80 μm square) and then moving the sample and "stitching" them together into a large pattern. The translation stage that holds the sample is positioned by a laser interferometer to an accuracy of ~2 nm.

In the writing process, several sources of stitching errors occur, which can be divided in two types: those that are independent and those that are dependent upon the time between when the adjacent fields were written. There are several sources of time independent stitching errors. If, for example, the sample is not mounted in the plane of motion of the translation stage, the e-beam pattern is projected onto a different plane than intended. This causes the edges of adjacent fields to be systematically misaligned and introduces periodic "noise" into the actual large scale pattern. Another source of time independent errors is due to the software correction of imperfections in the e-beam writer's electron optics. The system corrects for improper scaling, rotational misalignment, and distortions within the writing field; mis-corrections, as with sample tilt, produce periodic errors.

Field stitching errors which depend on time turn out to be much more of a problem, and appear to be due to thermal drifts during the writing process. Temperature variations can alter the distance between the reference mirrors of the position monitoring interferometer and the sample, or can distort the e-beam writer housing, moving the lenses and steering the beam. These changes will lead to errors in the final position of the e-beam relative to the sample, and will generally increase with writing time.

We have studied these two classes of errors by writing patterns of verniers across field boundaries with and without time delays. The errors which are independent of writing time are on the scale of 20 nm if care is taken in aligning the sample in the sample holder, as this reduces the amount of software correction for scaling and rotation. The thermal drifts can, however, give errors as large as 80 nm over 10 minutes, a typical time to write a large grating pattern. Reducing these time dependent errors then becomes a problem of minimizing the time it takes to write a grating.

To reduce the writing time, one can use higher e-beam currents or stronger e-beam resist/developer combinations, as the latter requires a lower amount of e-beam exposure for the resist to be reliably removed. Unfortunately, both approaches result in lower resolution; higher beam currents give larger spot sizes, and stronger developers don't resolve fine structures as well. Best results were obtained with 2 nA of beam current, and a 1:1 mixture of MIBK:IPA as the developer, which reduced writing times for 140 nm period gratings to approximately 2 minutes for a 1.5 x 0.05 mm size grating.

2. DIFFRACTION GRATINGS

One of the most interesting and versatile atom optics devices is the diffraction grating, which can serve as an atomic beam splitter or recombiner. An elegant way to realize a phase grating for atoms is by the use of a standing wave of near-resonant laser light[7]. Amplitude transmission gratings, however, have the advantages of simplicity and the ability to diffract atomic and molecular species which do not have strong laser-accessible transitions. Both types of gratings may also be used to construct a three grating interferometer[16, 24].

One of the problems faced in the construction of any device using one or more diffraction gratings is the total fraction of the incident beam intensity that is transmitted. This would be maximized if the gratings could be made free standing over the entire usable beam height of several millimeters but, unfortunately, a transverse support structure has to be added to stabilize the grating bars. This support structure absorbs a significant amount of beam intensity because it covers 20% to 50% of the area of our gratings. We have found that, for a given support structure coverage, the unsupported span

length of the fine grating bars should be kept as small as possible, with several microns of unsupported length being acceptable for a 50 nm wide grating bar.

The width of the slots between the grating bars as a fraction of grating period (i.e. the "open fraction") is another important characteristic of the grating. It is possible to obtain high resolution pictures of fabricated gratings with a scanning electron microscope, but we have found that these pictures do not always correspond to how the gratings "look" to the atomic beam; we have occasionally found gold gratings which looked good in the electron microscope but were "opaque" to atoms (these gold gratings were not metal coated before inspection, so the SEM may not have seen material in the slots). The best diagnostic that we have to investigate the open fraction seen by the atoms is the atomic diffraction pattern itself. Figure 2 shows diffraction patterns produced by 200 nm period gratings built with different methods and having different open fractions. The diffracted sodium beam has a deBroglie wavelength of 16 pm. The open fraction of the diffraction gratings seen by the atoms determines the relative heights of the diffracted orders, as the modulation of the intensity in each order is given by the single slit pattern formed by each slot between grating bars.

The fits shown in figure 2 convolve the theoretical diffraction pattern and an instrumental profile that is determined by a gaussian fit to the zero order diffraction peak. The relative heights of the various diffracted orders are thus determined by one variable, the open fraction of the grating. Although adjustment of the open fraction value gives a clear best fit with only ~1% uncertainty in the value, it is not possible to fit the diffraction data to within experimental error. Additional averaging in the fit due to the 12% velocity width of our atomic beam does not significantly reduce the strong disagreement in the heights of orders that we predict to be strongly suppressed using the best fit to the open fraction. The most likely source of this disagreement is due to small variations in the size and placement of the actual openings in the grating; this noise causes the opening to vary from the average size (which would produce essentially zero amplitude in the strongly suppressed order). We feel that the open fraction that we get from the fitting process represents a good "mean open fraction" value for the grating.

3. BLAZED GRATINGS

In addition to varying the open fraction of the grating, the intensity in the various diffracted orders could be selectively increased by using blazed gratings. In classical optics, the intensity of the various diffracted orders produced by a blazed diffraction grating is tailored by systematically varying the plate thickness so that the phase of the transmitted wave varies across each grating element. Analogously, to make a blazed grating for atoms, we need to vary the phase of the atomic wave function over the opening between grating bars.

We propose to create this phase shift by applying electric fields that vary in magnitude over the width of the slots in the diffraction grating. These electric fields could be created by metallizing the front and back of the grating and then applying a voltage between the metal electrodes (Fig. 3). The electric field in the slots causes energy shifts in the atoms (the DC Stark Shift). The potential (U) is much smaller than the incident energy (E) of the atoms (U/E = 10^{-3} - 10^{-4}), so an eikonal approximation[25] can be used to calculate the phase shift given to an atom traveling through the slot in the z direction a distance x from the center. In this approximation

$$\phi(x) = \int_x k\,dz - \int_x k_o\,dz \approx \frac{1}{\hbar v_o}\int_x U(x,z)dz \quad ,$$

where v_0 is the incident atomic velocity, and k_0 is the k vector of the atoms when U=0. Focusing or defocusing of the atoms (i.e. blazing of the grating) results because ϕ depends on x.

We have calculated the effects of such a blazing potential for a 200 nm thick grating on a sodium beam with a deBroglie wavelength of 16 pm. The phase shift across the slot $\phi(x)$ fits a parabola to within 4%, except for ~1/12 of the slot width closest to either slot edge (near the electrodes). The use of a parabolic functional form in our calculations was motivated by the desire for a simple form that would fit the data and allow an analytic solution of the single slit integral. We calculated the single slit diffraction pattern analytically for one such slot, allowing for the spatially varying phase shift (the fitted parabola), as a function of the applied voltage. This modified single slit pattern then is used a form factor to determine the intensities in the various diffracted orders. The results of our calculations appear in figure 4, where we show the intensities in various diffracted orders as a function of

applied voltage. Because the phase shift is symmetric about the center of the slot, the positive and negative diffracted orders have the same intensities.

An advantage of blazing is that it allows the use of wider slots for a given grating period, because the intensity in the diffraction pattern can be tuned with the applied voltage as intensity normally sent to the zero order is diffracted into higher orders. This results in more total transmitted intensity due to the lower overall opacity of the grating, as well as the larger intensities in the higher orders. This can be seen in figure 4, where the first order diffraction of the 80% open grating at a blazing voltage of 2.8 volts is approximately 1.6 times that of an unaltered 50% open grating. Intensities in higher orders can be increased even more dramatically. For example, the second order diffraction of the 80% open grating at 3.3 volts is almost as large as the first order diffraction in the unaltered 50% grating (which has the largest first order peak of any unblazed grating).

4. ZONE PLATES

Zone plates for atoms have been constructed[10, 11, 21], demonstrated[10], and studied[11] by several groups. Both spherical[11, 21] and cylindrical[10] zone plates have been built. We give here a discussion of our experimental results first presented elsewhere[10]. The objective of the experiment was to image an aperture (of one of our collimation slits) onto our detector using a cylindrical zone plate. The atomic beam was a seeded supersonic nozzle beam of sodium in an argon carrier gas. The expansion of the carrier gas gave the beam of sodium a narrow velocity distribution ($\Delta v/v$ = 12%), and a wavelength of 16 pm. The beam illuminated a 20 μm wide collimation slit (Fig. 5). A cylindrical zone plate (130 μm wide by 500 μm tall) was placed 1.5 m after the slit, and imaged the slit onto the detector plane, located 0.9 m downstream. The sodium atoms were detected after they surface ionized on a moveable 25 μm hot wire.

We have performed a complete numerical simulation of the performance of our zone plate using a procedure which has been described in detail elsewhere[26, 27]. Briefly, we calculate the sum of amplitudes at the detector plane generated by a point of the illuminated collimation slit passing through all the open parts of the zone plate, then sum the intensities for different locations in the slit and over a distribution of velocities.

The result of this simulation appears in figure 6, together with the experimental results. The curves were adjusted by using only the mean position and total intensity of the experimental and calculated images. The experiment was not set up in a way to make it possible to get an accurate figure for the amount of incident intensity in the image. The experimental results show a clear central peak, indicative of considerable focusing by the zone plate. The measured image, however, has more smoothing and greater width than calculated. There are several factors that could artificially enhance the observed image width. A narrowing of all open areas by a constant amount would cause the intensity of the zero order pedestal to fall off roughly as the inverse of the distance from the center of the image (but would not appreciably widen the central peak). A narrowing of this type large enough to account for the almost total suppression of intensity at the edge of the zero order pedestal is larger than we feel is reasonable to attribute to the fabrication process. A slight bend or tilt in the detector wire could also broaden the predicted sharp edges.

One thing that is obvious from the simulation of the cylindrical zone plate lens is that an unblazed amplitude zone plate is a very inefficient piece of atom optics, making an image containing only about 11% of the intensity as the image formed by an ideal lens. Thus, in our experiment, the pattern expected from a non focusing aperture with the same width as the zone plate exceeds the peak intensity expected with the zone plate in place (see figure 6). This intensity loss would seem to rule out the practical use of zone plate lenses except in a few special applications (e.g. to make an achromatic atom lens[2] or an atom microscope).

The performance of an amplitude zone plate is determined almost entirely by the size of the smallest feature s (the size of the slots or bars at its outer edge). This determines the maximum first order diffraction angle for a deBroglie wavelength λ_{dB}, of $\theta_m = \lambda_{dB}/2s$, and directly determines the f-number, $f = 1/2\theta_m = s/\lambda_{dB}$. The focal spot size is $\lambda_{dB}f \cong s$, so it is not improved (unlike the f number) by using a slow atomic beam (we have assumed $s << \lambda_{dB}$). The maximum transverse momentum transfer of the lens is $p_\perp = h/2s$, corresponding to a maximum transverse temperature that can be focused[28] of $p_\perp^2/2m$ (~42 μK for sodium atoms, assuming s = 50 nm).

FUTURE DIRECTIONS

There are several promising areas to explore with fabricated amplitude structures for atom optics. These include better diffraction gratings with smaller periods and larger areas, blazed diffraction gratings, and more general atom holograms.

We have recently completed an attempt to construct fine period, large area diffraction gratings for our atom interferometer experiments. We have constructed grating periods as small as 100 nm that have ~35 nm free standing bars. To write smaller periods at more reasonable grating open fractions will require less e-beam current to get a smaller spot size. Since this will increase the writing time, thermal drifts in the e-beam writer will become a severe problem. Perhaps moving to a field emission version of the e-beam writer or a return to optical holographically written gratings using UV light[17, 18, 19, 20, 29] will be necessary to make uniform large area gratings with fine periods.

As the far field diffraction patterns produced by gratings, single slits, and double slits are simply the Fourier transform of the pattern itself, there is no reason not to tailor the e-beam written pattern to make more complicated images in the far field (or indeed in the intermediate field). With the addition of lenses and slow, bright atomic beams, one has all of the tools to do holographic atom printing onto a substrate[30]. This would be analogous to reduction printing in standard photolithography. With the rapidly growing collection of atom optics elements, atom beam experiments may soon be used even in the construction of micro-structures.

We would like to thank Mark Shattenburg and Hank Smith for introducing us to the opportunities and intricacies of nanofabrication, and to acknowledge the discussions and help in the lab from the staff at NNF, Mike Rooks and Bob Soave in particular. We would also like to thank Alex Martin for careful and valuable readings of this manuscript. This work was supported by ARO grant DAAL03-89-K-0082, ONR grant N00014-89-J-1207, and JSEP grant DAAL03-89-C-0001.

REFERENCES

1. V. I. Balykin, V. S. Letokov: *Phys. Today* , 1989 (1989).

2. D. E. Pritchard: "Atom Optics", J. C. Zorn, R. R. Lewis, Eds., ICAP 12 (American Institute of Physics, Ann Arbor, MI, 1991), pp. 165-174.

3. I. Estermann, O. Stern: *Z Phys.* **61**, 95 (1930).

4. J. A. Leavitt, F. A. Bills: *Am. J. Phys.* **37**, 907 (1969).

5. H. Friedburg, W. Paul: *Z. Phys.* **130**, 493 (1951).

6. H. Friedburg, W. Paul: *Naturwissenschaften* **38**, 159 (1951).

7. P. L. Gould, G. A. Ruff, D. E. Pritchard: *Phys. Rev. Lett.* **56**, 827 (1986).

8. D. W. Keith, M. L. Schattenburg, H. I. Smith, D. E. Pritchard: *Phys Rev Lett* **61**, 1580-1583 (1988).

9. O. Carnal, A. Faulstich, J. Mlynek: *Appl. Phys. B* **53**, 88 (1991). The microstructures used in this work were constructed by Heidenhaim Inc. (Traunreut, Germany).

10. D. W. Keith, M. J. Rooks: *J. Vac. Sci. Technol. B* **9**, 2846 (Nov/Dec 1991).

11. O. Carnal, M. Sigel, T. Sleator, H. Takuma, J. Mlynek: *Phys Rev. Lett.* **67**, 3231 (1991). The microstructures used in this work were constructed by Heidenhaim Inc. (Traunreut, Germany).

12. J. J. Berkhout, et al.: *Phys. Rev. Lett.* **63**, 1689-92 (1989).

13. R. B. Doak: *Opt. Soc. of Am. Tech. Digest* **15**, 250 (1989).

14. Personal Communication with P. Meystre

15. O. Carnal, J. Mlynek: *Phys. Rev. Lett.* **66**, 2689 (1991). The microstructures used in this work were constructed by Heidenhaim Inc. (Traunreut, Germany).

16. D. W. Keith, C. R. Ekstrom, Q. A. Turchette, D. E. Pritchard: *Phys. Rev. Lett.* **66**, 2693 (1991).

17. E. H. Anderson, C. M. Horowitz, H. I. Smith: *Appl. Phys. Lett.* **43**, 874 (1983).

18. N. M. Ceglio, A. M. Hawryluk, R. H. Price: *Proc. SPIE Int. Soc. Opt. Eng.* **316**, 134 (1981).

19. A. M. Hawryluk, N. M. Ceglio, R. H. Price, J. Melngailis, H. I. Smith: *J. Vac. Sci. Technol.* **19**, 897 (1981).

20. H. I. Smith, E. H. Anderson, A. M. Hawryluk, M. L. Shattenburg: in *X-Ray Microscopy*(Springer-Verlag, Berlin, 1983), vol. 43,.

21. D. M. Tennant, et al.: *J. Vac. Sci. Technol. B* **8**, 1975 (1990).

22. Personal communication with M. Rooks and B. Soave.

23. The RIE recipe is 42 sccm CF_4 and 5 sccm H_2 at 15 mTorr with 100 Watts of RF power, yielding 340 Volts of dc bias.

24. V. P. Chebotayev, B. Y. Dubetsky, A. P. Kasantsev, V. P. Yakovlev: *J. Opt. Soc. Am. B* **2**, 1791 (1985).

25. L. D. Landau, E. M. Lifshitz: in *Quantum Mechanics (Non-relativistic Theory)*(Pergamon Press, 1977), vol. 3, pp. 538.

26. Q. A. Turchette, D. E. Pritchard, D. W. Keith: *Submitted to JOSA B* , (1991).

27. Q. A. Turchette: S. B., MIT (1991).

28. This value is incorrectly given as 20 μK in reference 2.

29. Personal communication with H. I. Smith, S. C. Hector, M. L. Shattenburg, and E. H. Anderson

30. Sodium gratings on silicon substrates have been produced by M. Prentiss et al.

Figures

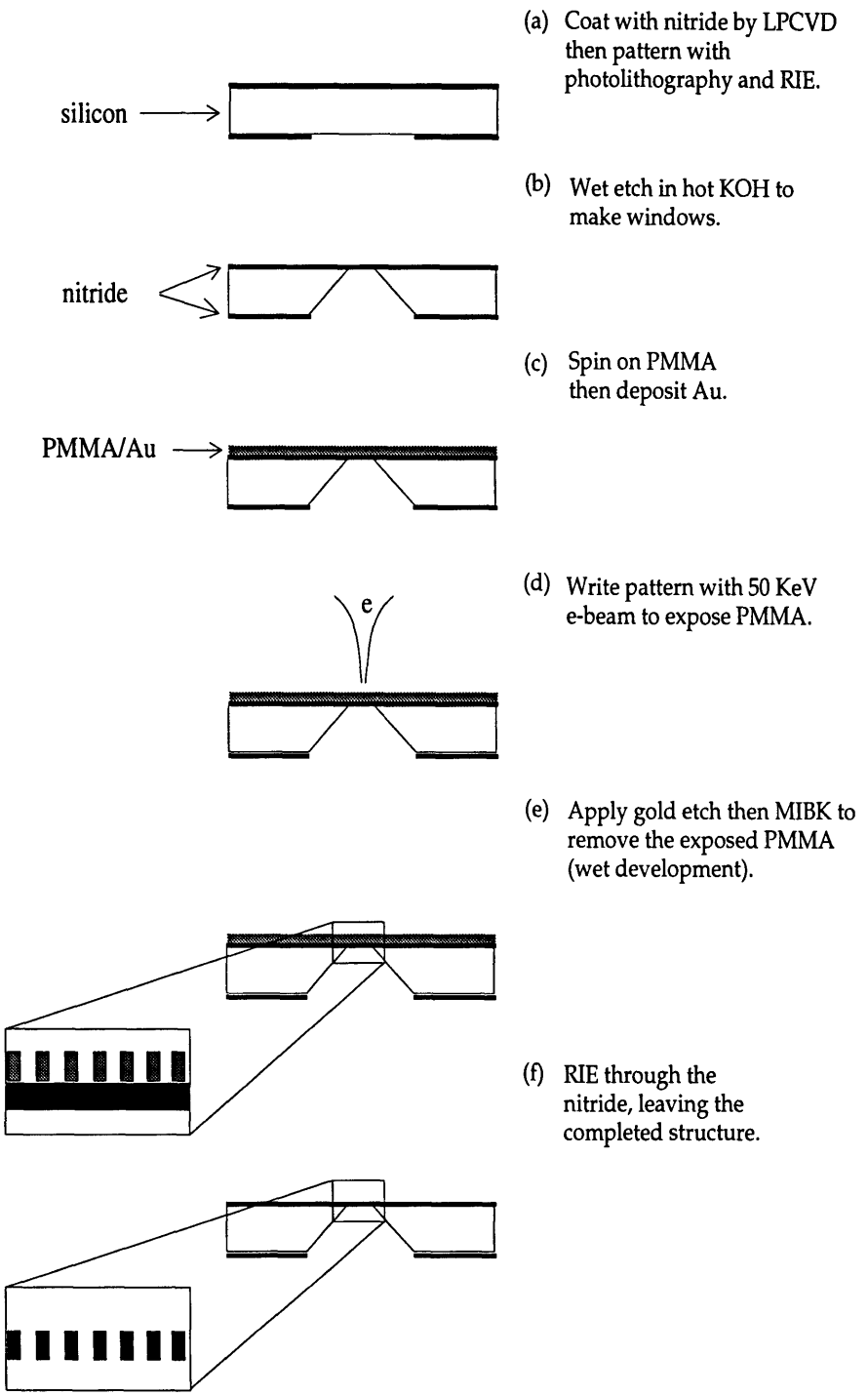

Figure 1. Construction steps to produce a patterned, free standing silicon nitride membrane.

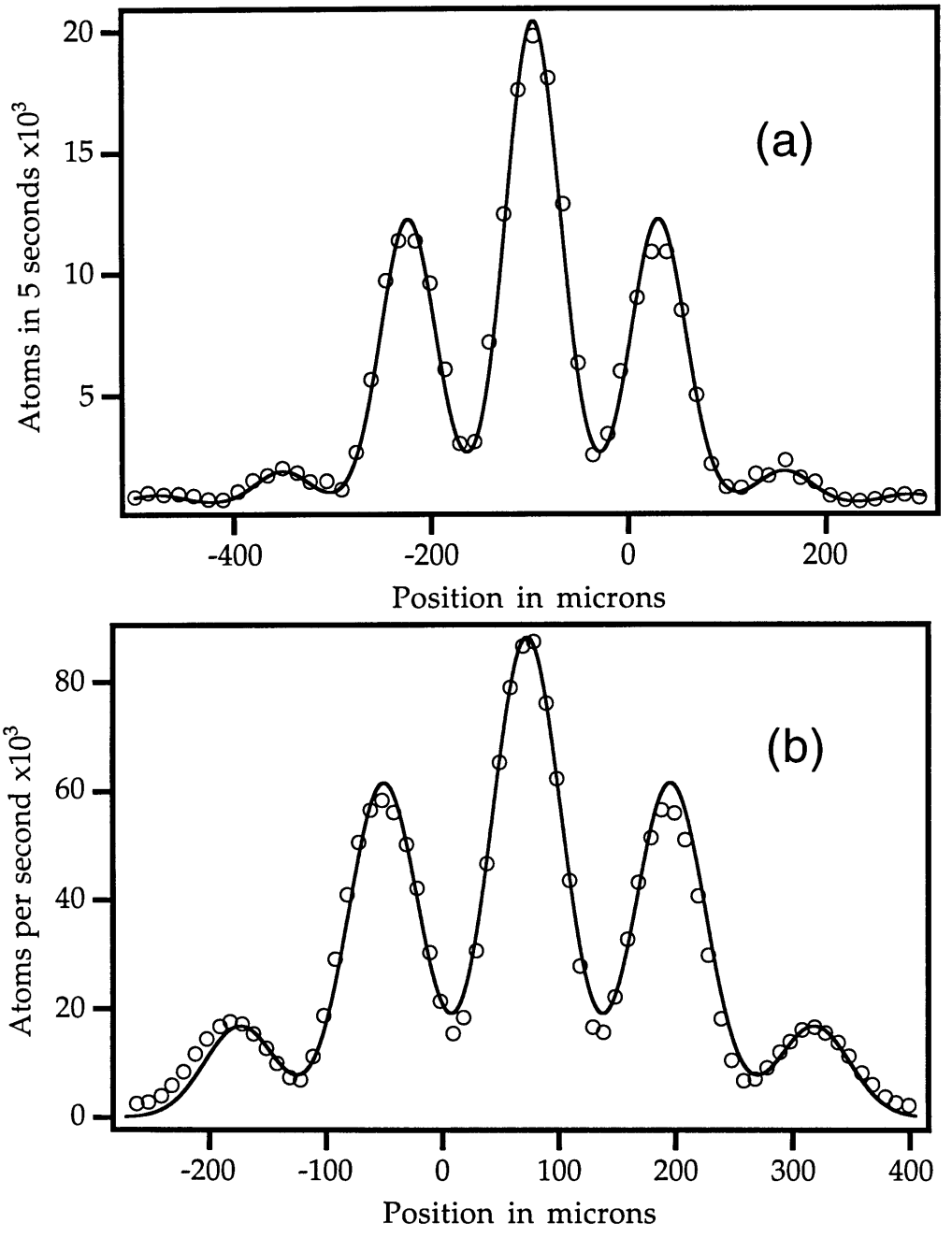

Figure 2. Diffraction of an atomic beam from a free standing 200 nm period diffraction grating. The data in (a) was taken with a gold grating built at the MIT Submicron Structures Lab. The theoretical fit is for an open fraction of 39%. The data in (b) was taken with a silicon nitride grating constructed at the National Nanofabrication Facility at Cornell University. The fit is for an open fraction of 33%.

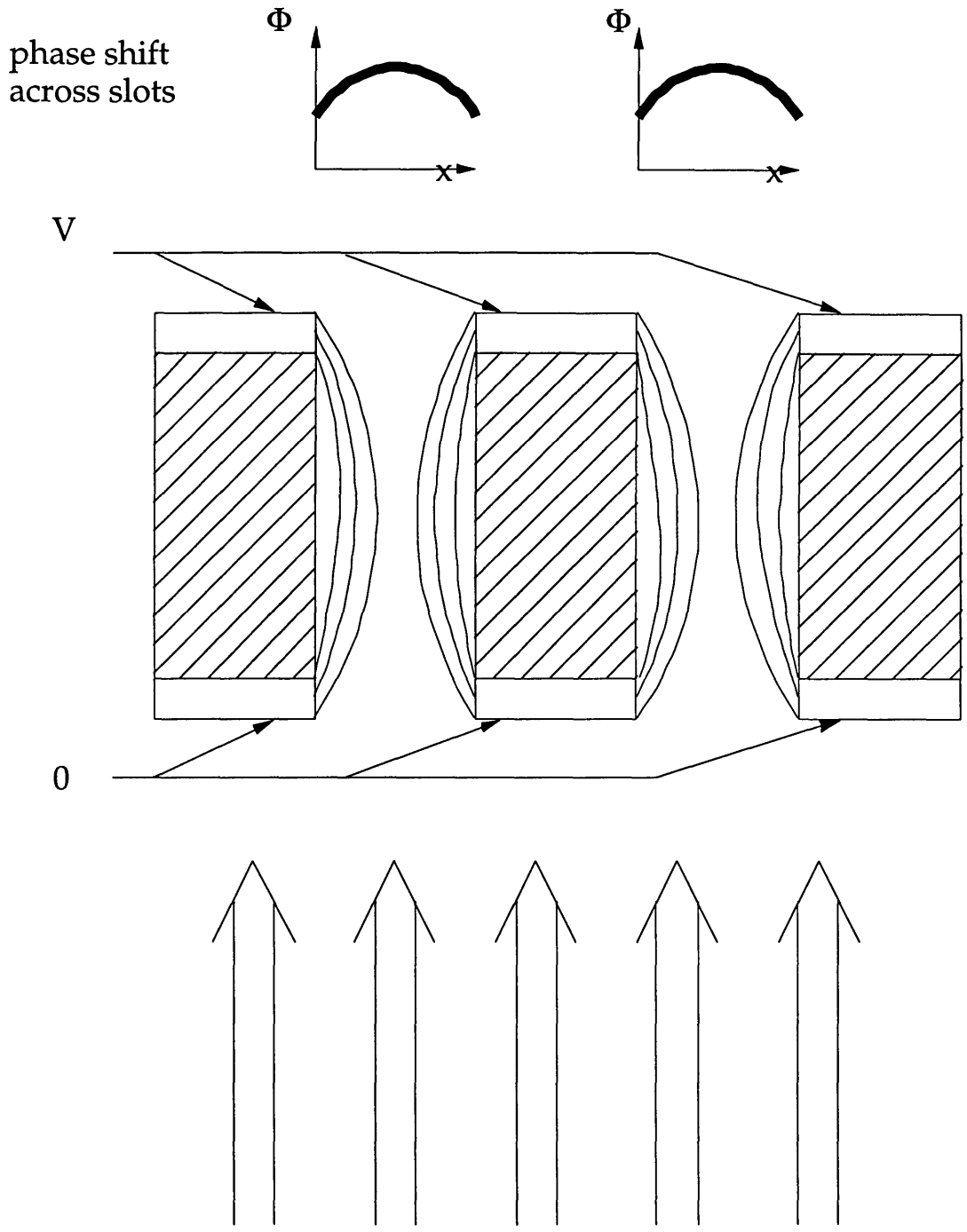

Figure 3. Cross section of several grating bars of a blazed atom grating. Hatched areas are silicon nitride. The potential difference (V) to produce the electric fields is applied between the front and the back electrodes. The electric field lines, shown between the grating bars, lead to varying phase shifts at different positions across each slot (insets).

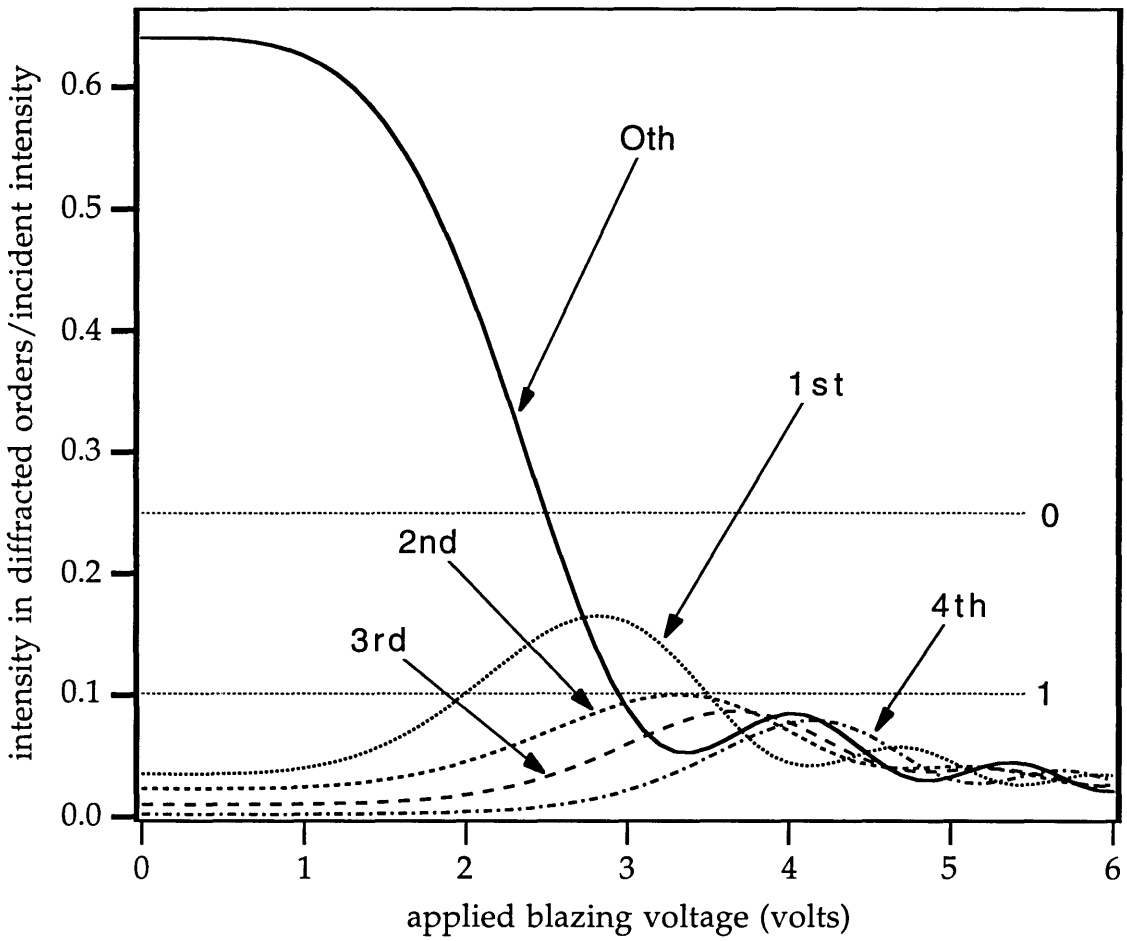

Figure 4. Predicted intensity in various orders of our sodium beam diffracting through a 200 nm thick blazed grating with an open fraction of 80%. The horizontal axis represents the voltage applied between the front and the back of the grating. The two horizontal dotted lines represent the intensities of the zero and first order maxima (labeled by 0 and 1 respectively) of an unaltered 50% open grating.

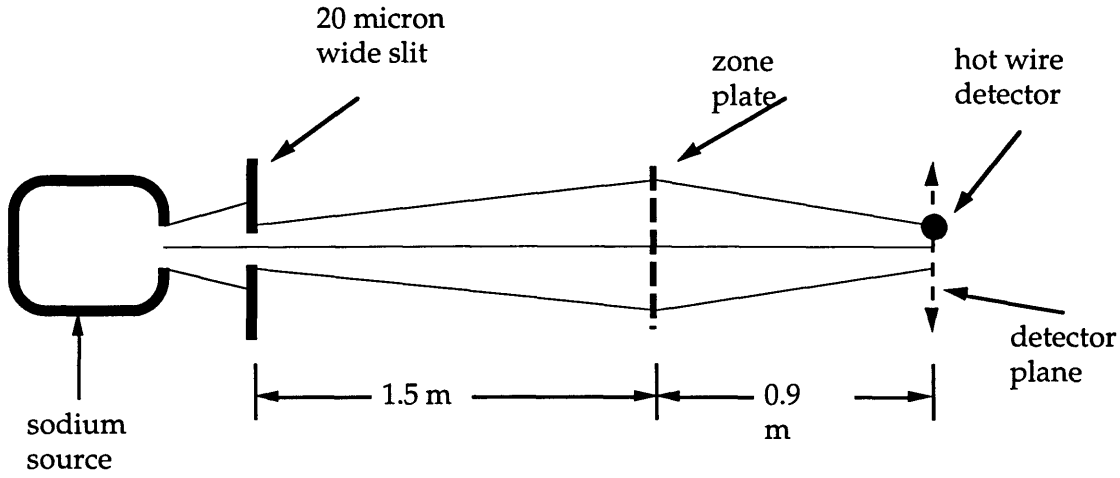

Figure5. Experimental setup used for imaging a 20 um wide slit onto our hot wire detector using a cylindrical zone plate.

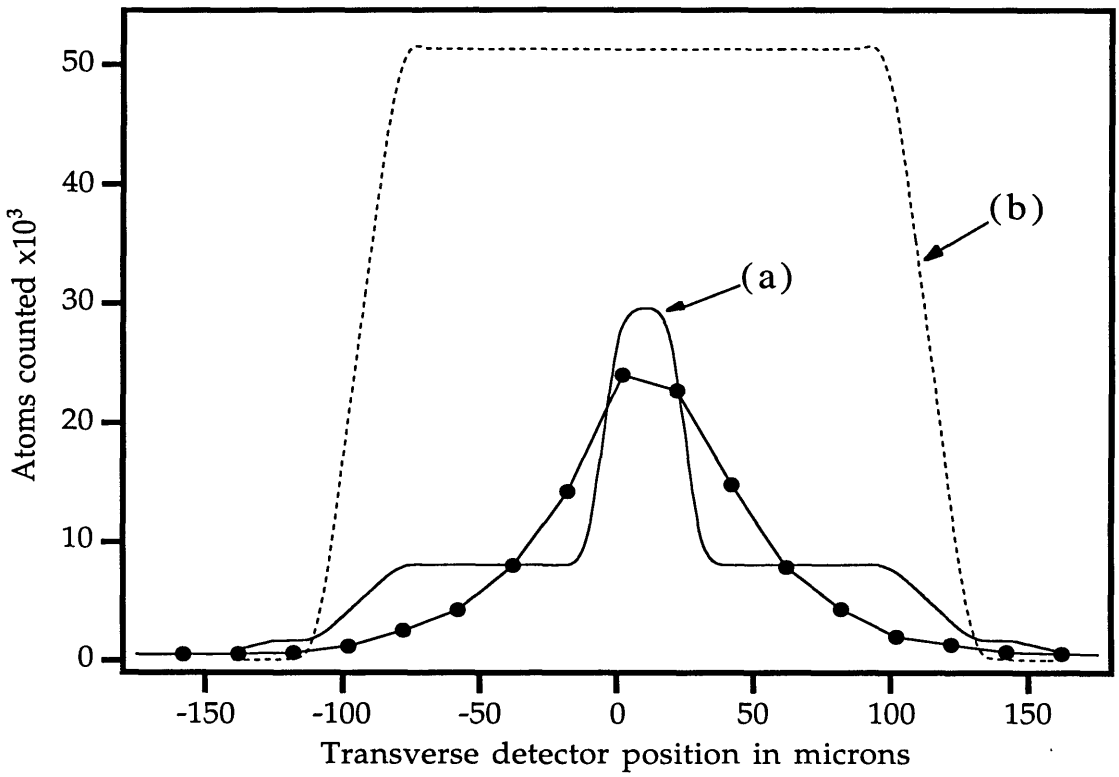

Figure 6. Experimental data (points) showing the image formed by a zone plate lens (the line joining the points is solely to guide the eye). Curve a is the theoriticaly predicted pattern formed by the lens (assuming a 1/2 density support structure), and b is the pattern predicted if the zone plate is replaced by a slit of identical size. The curves were adjusted by using only the mean position and total intensity of the experimental and calculated images.

1.4 The interaction region

Besides getting the interferometer running with 200 nm period gratings, the most significant step in realizing the physics in this thesis was getting a barrier between the beams of the interferometer.

The interaction region consists of a stretched foil that is held between two side plates. The foil is spaced from the side plates with insulating spacers. The 2 mm thick spacers are made from alumina and have been ground to be very flat. Just how flat they are is covered in section 4.6.

The foil must be very flat to fit between the beams in the interferometer. The materials that have been successfully used are 10 micron thick copper foil and 12 micron thick metalized mylar. The foil is cut with a sharp scalpel into a "butterfly" shape as shown in Figure 1.5. This shape was chosen to pull wrinkles in the foil out to the area that will not be used in the final interaction region. The foil is then clamped and carefully stretched to flatten it. The foil is clamped between the spacers, side plates, and clamping pieces in an assembly jig. The clamping pieces are tightened together, and the resulting assembly can then be removed from the jig and mounted in the machine. An exploded view of the interaction region is shown in Figure 1.6. One key to preserving the flatness of the foil while the assembly is clamped is to round

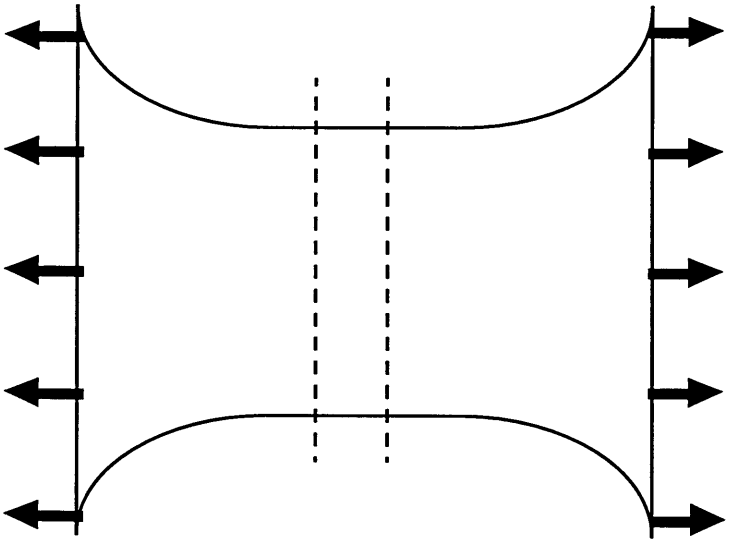

Figure 1.5: The foil is stretched from both sides to remove wrinkles. The area inside the dotted lines is used in the final interaction region.

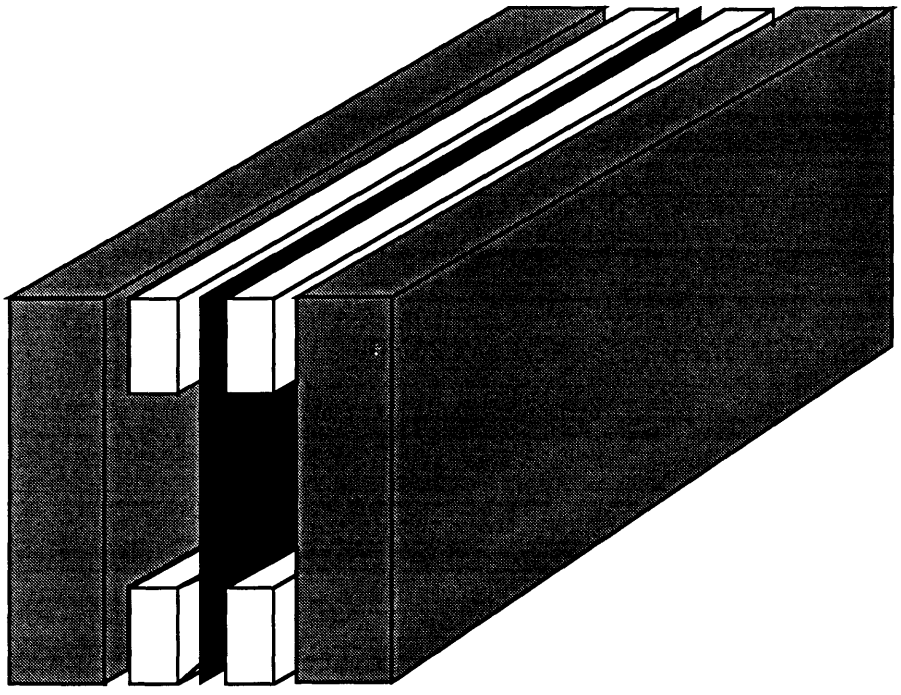

Figure 1.6: Exploded view of the interaction region. The foil is black. The insulating alumina spacers are shown in white, and the aluminum side plates are gray. The split atomic beams of the interferometer enter from the front of the page and pass on either side of the foil.

over the edge of the spacer that touches the foil on the inside of the assembly.

The interaction region is mounted on a complicated stack of manipulators which is located immediately after the second grating. All of the manipulators for both the interaction region and the second grating hang from of the same vacuum flange. The manipulators provide transverse translation to move the foil into or out of the beam line with .25 micron accuracy. The rotation about the beam axis is necessary to align the foil to the beam over its height. Rotation about the vertical axis (y axis) allows the plane of the foil to be aligned parallel with the atomic beam. All of these motions are controllable from outside the vacuum envelope.

1.5 The position servo

Up to this point, no mention has been made of how the relative transverse positions of the gratings are measured. They are monitored and controlled with a laser interferometer servo system. The laser interferometer built around four phase diffraction gratings, and has the same topology as the atom

interferometer. Figure 1.7 shows the laser interferometer, atom interferometer, and the position servo system.

The same laser interferometer position servo and position monitor is being used as was described in David Keith's thesis [KEI91]. Because they have the same topology, the laser interferometer changes phase in the same manner as the atom interferometer. The phase of the interference pattern of either interferometer is

$$\varphi = \frac{2\pi}{p}(x_1 - 2x_2 + x_3),$$

where p is the grating period of the interferometer in question, and x_i is the position of the i^{th} grating. The optical gratings have a period of 333.3 lines/mm. The signal from the optical interferometer is filtered through a feedback network and sent to a piezeo-electric transducer (PZT) that alters the position of the second grating. This allow us to lock the optical interferometer signal to the side of a fringe, fixing the relative position of the three grating platforms. By altering the reference voltage in the feedback

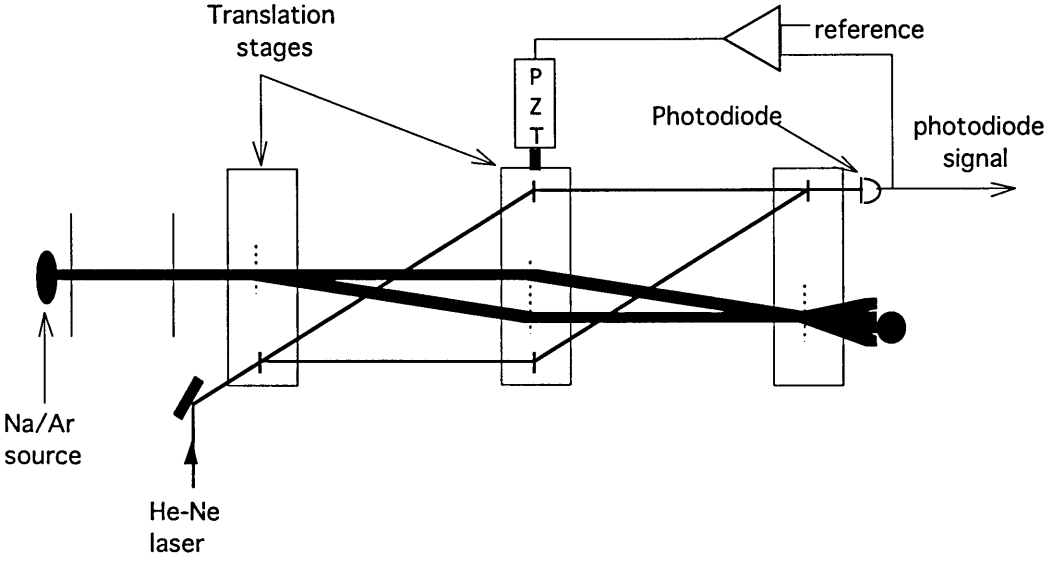

Figure 1.7: The atom interferometer with laser interferometer position servo and monitor shown. Not to scale.

network, we can alter the relative displacement of the three gratings. The value of the error signal in the lock loop tells us the relative position of the three platforms. By scanning across several atom interferometer fringes, and

then correlating the transmitted intensity with relative grating position, we see the fringe pattern shown in Figure 1.3.

We now operate the lock loop with slightly different parameters, and with slightly different goals. The change in operating procedure is made possible by having an atom detection system that is an order of magnitude faster than before.

The lock loop is now used almost exclusively as a position monitor. This is because we have a detector that will successfully "track" position changes that happen on a millisecond time scale. This means that what we care about is the amount of residual noise above several hundred Hertz. Below several hundred Hertz, we just record what the relative position of the three gratings was in a short time bin (almost always 2 msec) and how many atoms went through the interferometer when it was in that configuration.

Fast noise is a problem. The detector will not be able to track the noise, and we will lose contrast. The solution was to lower the closed loop gain on the lock loop. When the gain is increased in the lock loop, the rms width of the residual motion decreases until oscillations occur. This decreased rms vibration, however, has more power at high frequencies than the original vibration spectrum. This is just what we can not tolerate. What we do is to lock much less tightly, and keep most of the noise power at lower frequencies. At very low frequencies, the noise is almost totally suppressed due to the very high DC loop gain in the system. This leaves us with most of the noise in a "trackable" frequency band, and also gives us the necessary DC (phase) stability.

2 Experimental procedures and data collection

This chapter will cover the basic steps and considerations involved in aligning the machine, taking the data, and analyzing it. It will also cover analysis of the diffraction pattern from a single diffraction grating.

2.1 Transverse alignment of the beam machine

The gross transverse alignment of the machine is performed with the aid of a surveying telescope. The telescope is positioned to look down the beam line and a light is positioned behind a window in the end of the detector chamber. The beam line is determined roughly by the location of several bulkheads, vertical height limiters, the detector box, the interaction region, the Stern-Gerlach magnet, and any other things that are in there for whatever particular experiment is set up. To learn this procedure, there is no substitute for aligning the machine several times with someone who knows what to look for.

The gratings are located in windows that are 1.5 mm high, and 50 to 200 microns wide. They must all be aligned vertically with each other by moving them in their mounts and checking the result by looking through the telescope. Unfortunately, the entire flange with grating positioners must be removed to do this, making it difficult and time consuming. Rough transverse alignment is performed by looking down the beam line and moving the translator motors from the computer. The transverse alignments of the collimation slits, interaction region, and detector are performed in the same way.

There are many movements that can be controlled by the computer. These motions are actuated by DC motors and quadrature position sensors. I will

describe the movable elements in order down the beam line. The second collimation slit can be translated across the beam (x axis), and rotated around the beam axis (z axis). Immediately after the second collimation slit, there is a vertical height limiter that can be opened symmetrically about the beam axis. The first diffraction grating can be moved across the beam and rotated around the beam line as well. The second grating can be moved across the beam line, and in addition there is a fine control of this motion actuated by a piezo-electric transducer. The interaction region can be moved across the beam line, rotated about the beam line, and rotated about the vertical axis out of the interferometer plane (y axis). The third grating can be moved across the beam and rotated around the beam. A second beam height limiter is located just before the detector, and it can be opened and translated vertically (y axis). The detector can be moved across the beam line.

The first collimation slit can be moved across the beam line by hand from outside the vacuum envelope.

There are several other adjustments that must be made by hand with the main chamber vented. All of the grating holders can be translated vertically and the second grating can be rotated about the beam axis. The first vertical height limiter can be positioned vertically on the beam line. In practice, once the limiter is in place, it is used as one vertical height reference for determining the beam line.

The rough rotational and tilt alignment of the interaction region are also done optically with the telescope. The interaction region is manipulated until the septum appears as a fine vertical line.

Fine alignment of the various parts of the interferometer are performed using the transmitted sodium beam as a diagnostic.

2.2 Rotational alignment of the diffraction gratings

The three gratings must all be aligned with respect to each other around the beam line (z axis). The fine diffraction grating bars must be rotated until they are parallel to each other and aligned vertically (y axis). This problem was not analyzed in enough generality in David Keith's thesis [KEI91]. That analysis did not take into account possible paths through the interferometer that changed height. To analyze the problem of how the contrast in the interferometer is degraded with rotations I choose a coordinate system with

the z axis in the beam direction, the x axis is across the plane of the interferometer, and the y axis runs up the grating bars. While this derivation logically belongs in chapter 3, I have included it here to make clear the problems of rotationally aligning the interferometer.

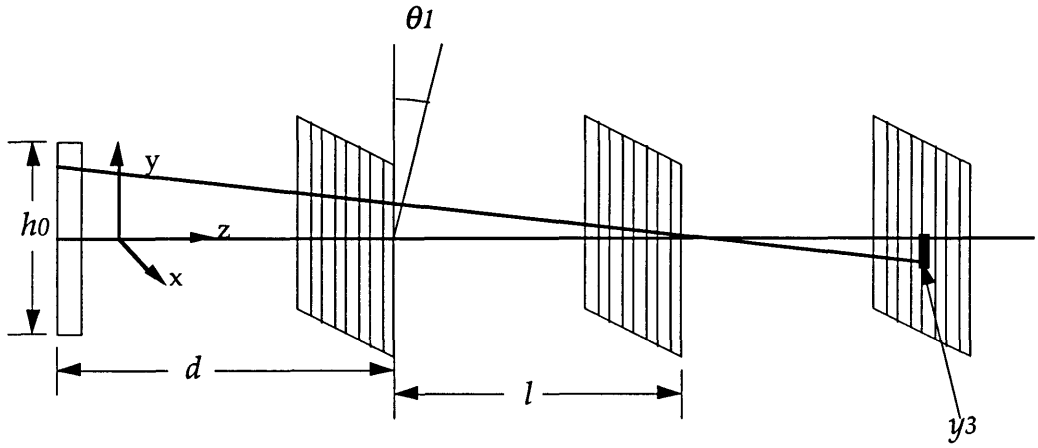

Figure 2.1: Geometry for the calculation of interferometer contrast as a function of grating rotation.

For the following derivation, the height of the source is $h0$ and the height of the detector at the third grating plane is $h3$. Coordinates will be labeled by subscripts that denote the grating that they are measured at with the index 0 indicating the source plane. The source is a distance d from the first grating, and there is a distance l between gratings. The rotations of the gratings are given by θ_i. The geometry of the problem is illustrated in Figure 2.1

The calculation starts with the basic formula for the phase shift from translation of the gratings.

$$\varphi = \frac{2\pi}{p}(x_1 - 2x_2 + x_3)$$

A point y on a grating appears to have been shifted over by (for small angles)

$$x_i = \theta_i y_i .$$

If we consider a ray through the interferometer that originates at a height $y0$ at the source, and ends at a height $y3$ on the third grating, it has an angle ξ down or up through the interferometer given by

$$\xi = \frac{y_3 - y_0}{d + 2l},$$

which fixes the height that the ray intersects the first and second gratings to be

$$y_1 = y_0 + \xi d$$
$$y_2 = y_3 - \xi l.$$

With all of these ingredients, we can find out the phase shift of the interference pattern for each ray through the height of the interferometer in terms of the angles of the gratings, the source point location, and the third grating (detector) point location. The result is:

$$\varphi(\theta_1, \theta_2, \theta_3, y_0, y_3) = A(\theta_1, \theta_2) y_0 + B(\theta_1, \theta_2, \theta_3) y_3,$$

where

$$A = \frac{2\pi b}{p}(\theta_1 - \theta_2)$$
$$B = \frac{2\pi}{p}\left(a(\theta_1 - 2\theta_2 + \theta_3) + b(\theta_1 - \theta_2)\right)$$

I have defined two dimensionless geometric factors a and b as follows:

$$a = \frac{d}{d + 2l}$$
$$b = \frac{2l}{d + 2l}.$$

It is clear that there are only two independent angular variables in the problem. The natural ones for us to use are $\alpha_1 = \theta_1 - \theta_2$ and $\alpha_3 = \theta_3 - \theta_2$, because we can rotate the first and third gratings while the interferometer is running.

The interference pattern for a given ray looks like

$$\cos\left(kx - \varphi(\theta_1, \theta_2, \theta_3, y_0, y_3)\right)$$

To find the total reduction in contrast, this interference pattern must be averaged over all source and detector point heights. The result of these averages gives a relative contrast of

$$C(\theta_1, \theta_2, \theta_3; h_0, h_3) = \left| \frac{\sin\left(\frac{A(\theta_1, \theta_2) h_0}{2}\right)}{\frac{A(\theta_1, \theta_2) h_0}{2}} \right| \left| \frac{\sin\left(\frac{B(\theta_1, \theta_2, \theta_3) h_3}{2}\right)}{\frac{B(\theta_1, \theta_2, \theta_3) h_3}{2}} \right|.$$

A typical plot of relative contrast plotted against α_1 and α_3 is shown in Figure 2.2.

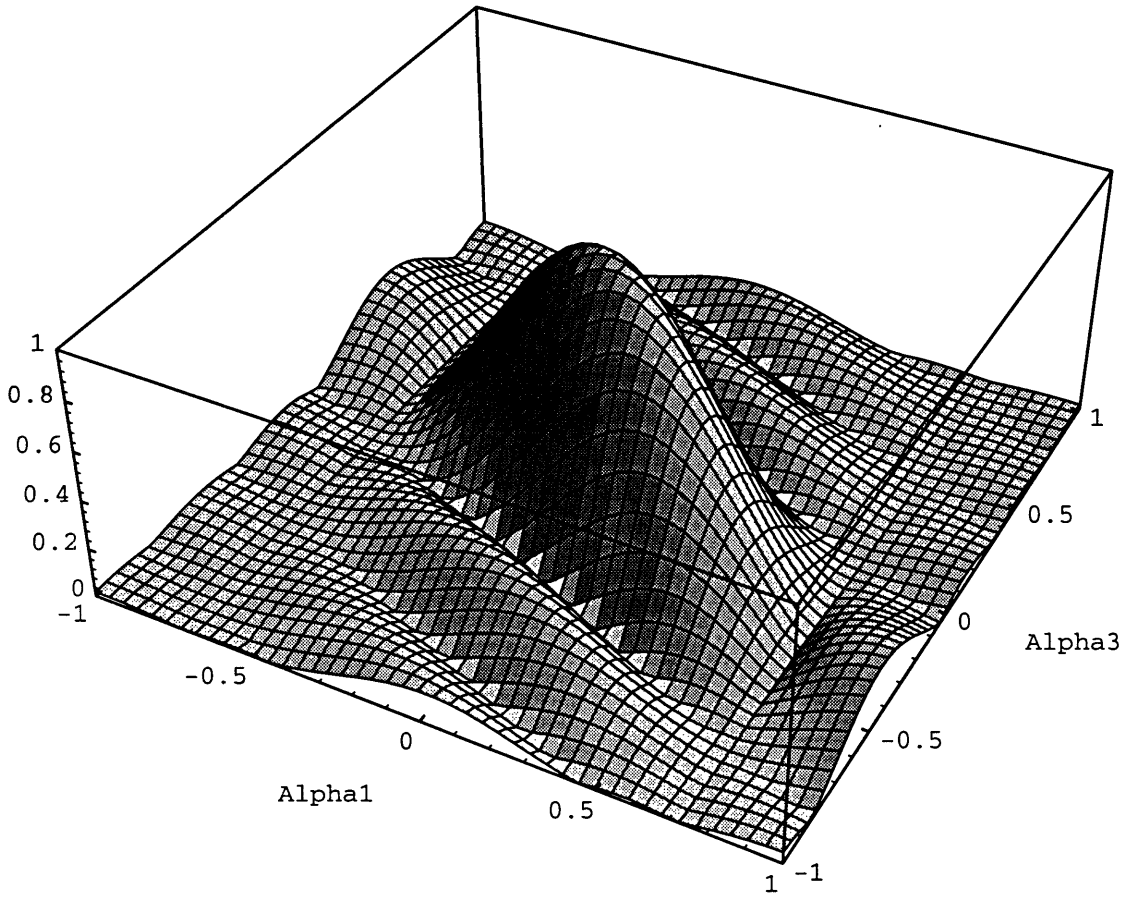

Figure 2.2: Relative contrast as a function of the two angular variables $\alpha_1 = \theta_1 - \theta_2$ and $\alpha_3 = \theta_3 - \theta_2$ The angles are in milliradians. The source height and detector height were both 500 microns.

We line up the gratings in two stages, a preliminary alignment outside the vacuum envelope, and a final rotational search using the interferometer contrast as a diagnostic.

The initial alignment is performed with the grating flanges flipped over and the grating mounts protruding into the air. A He-Ne laser is diffracted from the grating support structure and all diffracted orders are aligned in a common plane. The plane is defined by two plumb bobs. There is a wire that runs between the tops of the two plumb bobs that defines the top of the plane. The basic idea is unchanged from David Keith's thesis [KEI91], but by using a single wire to define the plane, we feel that the gratings can be aligned to within +/- 1/2 milliradians. By rotating the entire flange around the beam axis, any tilt in the flange seats cancels out. This is important because the seats are tilted with respect to each other by many milliradians.

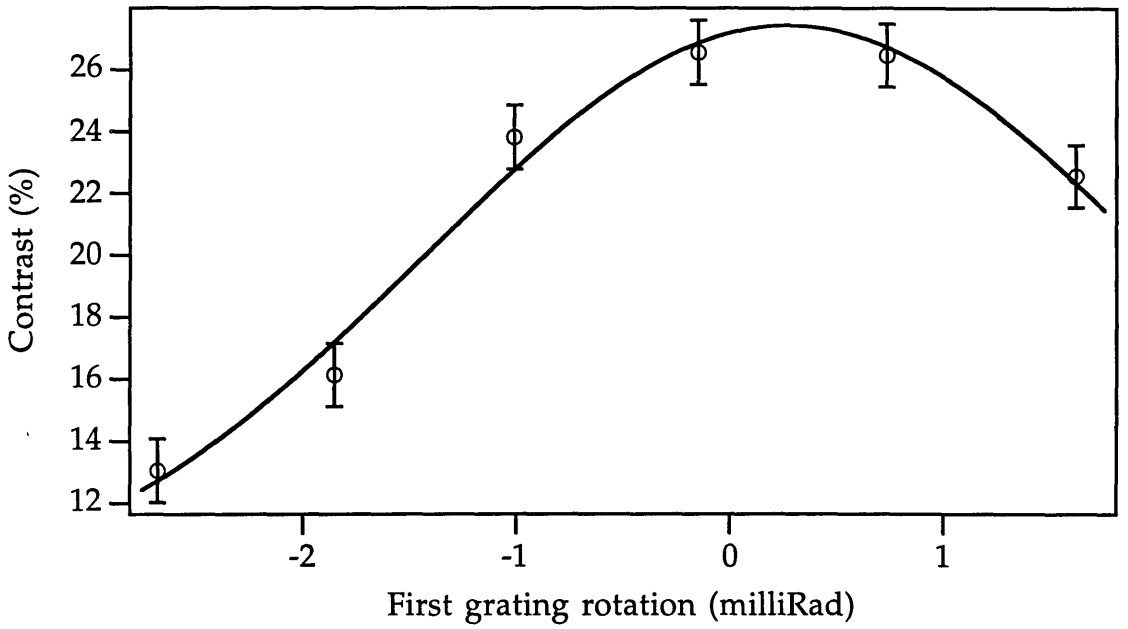

Figure 2.3: Contrast of the interference pattern as a function of first grating rotation. The fit is to a gaussian and is to guide the eye.

The final alignment involves rotating the first and third gratings to maximize the contrast in the interferometer. It is sometimes necessary to search blindly to find interference the first time. It can be seen from Figure 2.2 that a grid search would be optimal in finding the maximum of the contrast pattern. In practice, we tend to do one dimensional searches of the first and third gratings. If we had to make a large correction to any one grating, we will do another search of the other to get closer to the maximum contrast available. Figures 2.3 and 2.4 show the dependence of contrast in the interferometer on the rotational alignment of the first and third gratings for typical operating parameters. For the data in these figures, the beam was limited to 500 microns high.

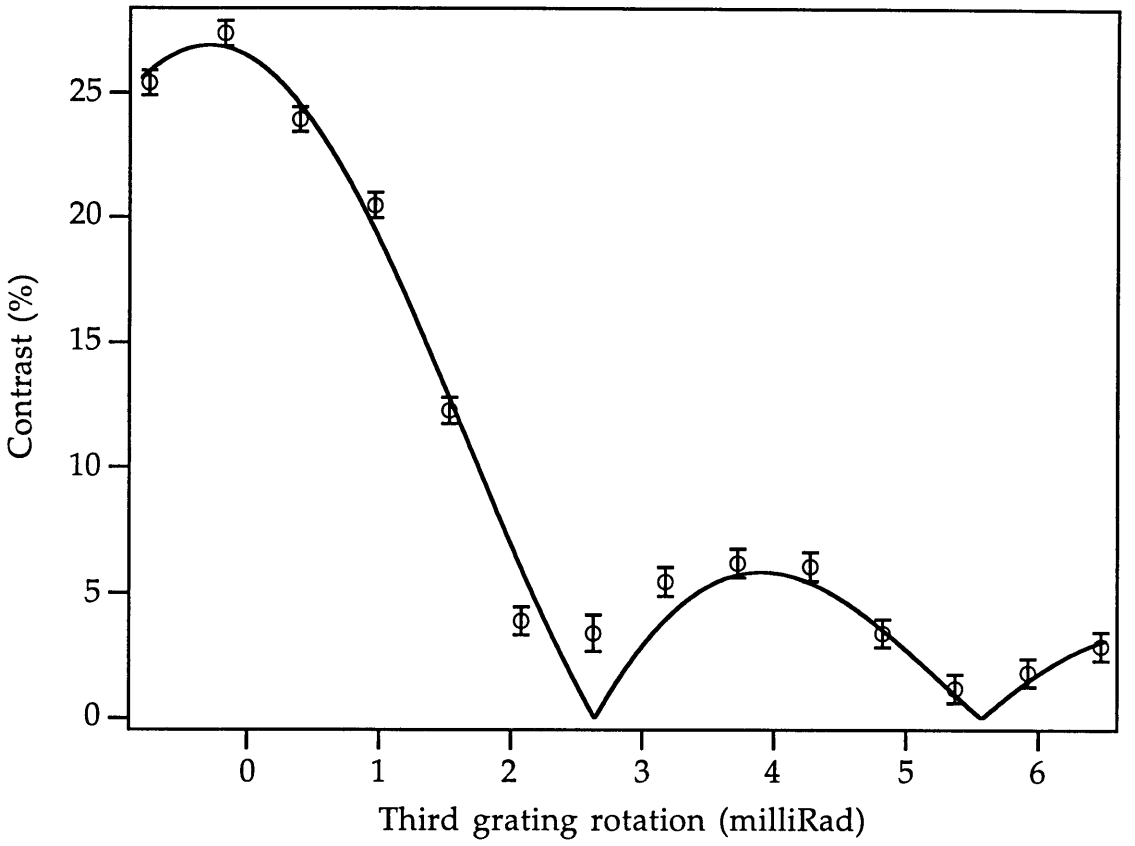

Figure 2.4: Contrast of the interference pattern as a function of third grating rotation. The fit is to a sinc function as predicted by the calculations from this section.

2.3 Data acquisition and analysis

Data collection on the IBM AT

Most of the data in this thesis was acquired with an IBM AT computer and a multifunction data acquisition card. This computer controls motor movement inside the vacuum envelope using a home built motor control box that can address up to 16 DC servo motors with quadrature position encoders. These motors are used to perform a variety of translations and rotations of gratings, slits, height limiters, and the interaction region.

The computer records the 5 volt pulses from the detected atoms on an accumulator. These counts can be recorded for a given length of time and correlated with the position of any motor to produce a scan of counts versus position. This feature is used in gross alignment of the interferometer, and to produce detector scans of the diffraction pattern from the first grating.

The computer also monitors the signal from the photodiode of the laser interferometer in the position servo system. Time histories of the number of counts and the photodiode signal are the standard way that interference data are taken.

All of the instrument control is accomplished with the aid of a data acquisition program ("tupeleck" for historical reasons) written by David Keith and myself. This has recently been replaced, as learning how to maintain it was quite a chore, and the last author is now leaving.

Data reduction and analysis

Data reduction is performed on a Macintosh Quadra 700 using a set of data analysis macros written for the data analysis and plotting package Igor. This is a great computer program that I would heartily recommend to anyone. The structure of the macros is described shortly.

The basic algorithm of binning the counts vs. position data is covered in David Keith's thesis [KEI91] but will be described briefly here. The basic idea is to correlate relative grating positions, as measured with the laser interferometer, with count rate to provide an average count rate versus relative grating position. This pattern is fit to a sine function, and the mean count rate, fringe amplitude, and phase are extracted.

One change in the analysis procedure a different way of removing noise spikes from the count data. With our new detector, problems from noise bursts from the detector have been greatly reduced. We now set a chopping threshold and invalidate any data with a count rate above that level. This has proven quite adequate, resulting in binned data that fits a sine function with typical reduced chi-squared values of 1.0(2).

Another modification has been increased automation of the data reduction. This has become necessary because of the large amount of raw data represented by the experiments described in this thesis. A set of interference scans is typically put in its own directory. The calibration data that is necessary for converting the position monitor's signal to relative displacement units is also included. The parameters from the calibration are extracted, and then the program will load, convert, correlate into bins, and fit each interference pattern. The results are loaded into a table of data for further manipulation. We typically do not look at the raw data after this point unless the reduced

chi-squared for that data set is ridiculous. This begs the question of why we transfer all that raw data, and future data acquisition schemes will perform most of the initial data reduction on line.

Further reduction such as fitting the phase or amplitude of the interference patterns against some parameter is performed in Igor. The analysis that is specific to a given experiment will be discussed in its own section.

The next generation: Macintosh data acquisition

The next generation data acquisition is being performed with a Macintosh Quadra 950. The computer uses the data acquisition system LabVIEW by National Instruments. The data for the Talbot effect, molecular diffraction, and some of the scattering data were acquired with this system. This system allows the user to quickly acquire and analyze interference scans. The short feedback time on the contrast and phase of the interference pattern allows quick rotational alignment searches, interaction region positioning, and on-line diagnostics of how you experiment is working.

2.4 Velocity measurements

We measure the mean velocity of the beam and the width of the velocity distribution by examining the diffraction pattern of atoms from the first grating. The angular separation of the diffracted orders is

$$\theta_{diff} = \frac{\lambda_{Na}}{p} = \frac{h}{mpv}.$$

The diffracted orders will also broaden because of the finite width of the velocity distribution coupled with the fact that the diffraction angle depends on the inverse of the velocity. By fitting the diffraction pattern, we can extract the mean velocity of the distribution and its width. The geometry is shown in Figure 2.5.

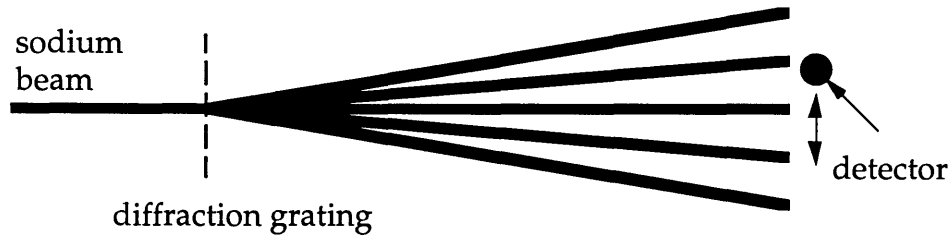

Figure 2.5: Diffraction of the sodium beam by an amplitude diffraction grating.

Early attempts at fitting the diffraction were not very successful. We were lacking a good model function for the diffraction pattern. The problem was in the way that the open fraction of the diffraction grating was dealt with. The open fraction of the grating determines the relative intensities in the various diffracted orders, or the form factors of the grating. When the fit called for a heavily suppressed order, the data always showed a more intense diffraction peak. This was because there was no provision for varying open fractions over the face of the grating to model roughness in the bars.

A more sophisticated fitting function is used now that includes an incoherent distribution of open fractions over the grating. If we consider a perfect grating with an open fraction β (slot width to period), the relative amount of power in the n^{th} diffraction peak (the form factor) is

$$\frac{\sin^2(n\pi\beta)}{(n\pi\beta)^2},$$

which is just the diffraction pattern from the slot between two grating bars evaluated at the angle of the n^{th} grating diffraction order. We now need to average over a distribution of open fractions. This averaged form factor will be

$$\int \frac{1}{\sqrt{2\pi\sigma_\beta}} e^{-(\beta-\beta_0)^2/2\sigma_\beta} \frac{\sin^2(n\pi\beta)}{(n\pi\beta)^2} d\beta .$$

In the above equation, σ_β is the width of the distribution of betas, and $\beta 0$ is the mean open fraction of the grating. This result can be simplified by first changing integration variables to another that represents the deviation of β from $\beta 0$, which I will call $a \equiv (\beta_0 - \beta)/\beta_0$. This leaves

$$\int P(a) \frac{\sin^2(a_0(1-a))}{(a_0(1-a))^2} da,$$

where $P(a)$ is a normalized gaussian with width σ_β, and $a_0 = n\pi\beta_0$. I next expand everything except the distribution function in a power series as a function of a. Because the distribution function is even, only even powers of the expansion will give non-zero results when integrated. I will include only the zero and second orders in a, so the result will then be correct up to third order. The expansion is

$$\frac{\sin^2(a_0(1-a))}{(a_0(1-a))^2} = \frac{\sin^2(a_0)}{{a_0}^2} + O[a]$$
$$+\left[\cos^2(a_0) - \frac{4\cos(a_0)\sin(a_0)}{a_0} + \frac{3\sin^2(a_0)}{{a_0}^2} - \sin^2(a_0)\right]a^2 + O\left[a^3\right] + \cdots$$

To aid in the readability of this section, the n dependence of a_0 has been suppressed. The only remaining integral to perform is that of the normalized distribution $P(a)$ multiplied by a^2. This is a standard gaussian integral, yielding ${\sigma_\beta}^2$. The final form factor for the n^{th} diffraction order of a grating having an open fraction $\beta 0$ with a distribution of betas having a width σ_β is:

$$\frac{\sin^2(n\pi\beta_0)}{(n\pi\beta_0)^2} + \left[\cos^2(n\pi\beta_0) - \frac{4\cos(n\pi\beta_0)\sin(n\pi\beta_0)}{n\pi\beta_0} + \frac{3\sin^2(n\pi\beta_0)}{(n\pi\beta_0)^2} - \sin^2(n\pi\beta_0)\right]{\sigma_\beta}^2$$

It can be seen by inspection that the additional term will tend to add power to an order that would ordinarily be heavily suppressed. If an order is heavily suppressed, $\sin(n\pi\beta_0)$ must be small, and therefore $\cos^2(n\pi\beta_0)$ must be the dominate term in the square bracket, insuring that the form factor correction is positive.

The width of the diffracted peaks increases with increasing order number because of the velocity width. We use a gaussian as the model function for our beam. The correct function would be a trapezoid convoluted with a rectangle. The gaussian function is a close description to the experimental beam profile, and makes calculations much easier, yielding analytic solutions.

The width of the zeroth diffraction order is σ_x. If the separation of the diffracted orders at the detector plane is s, then the width of the n^{th} diffracted order is given by

$$\sqrt{\sigma_x^2 + (ns\sigma_v)^2}\,.$$

A typical diffraction pattern with a fit is shown in Figure 2.6.

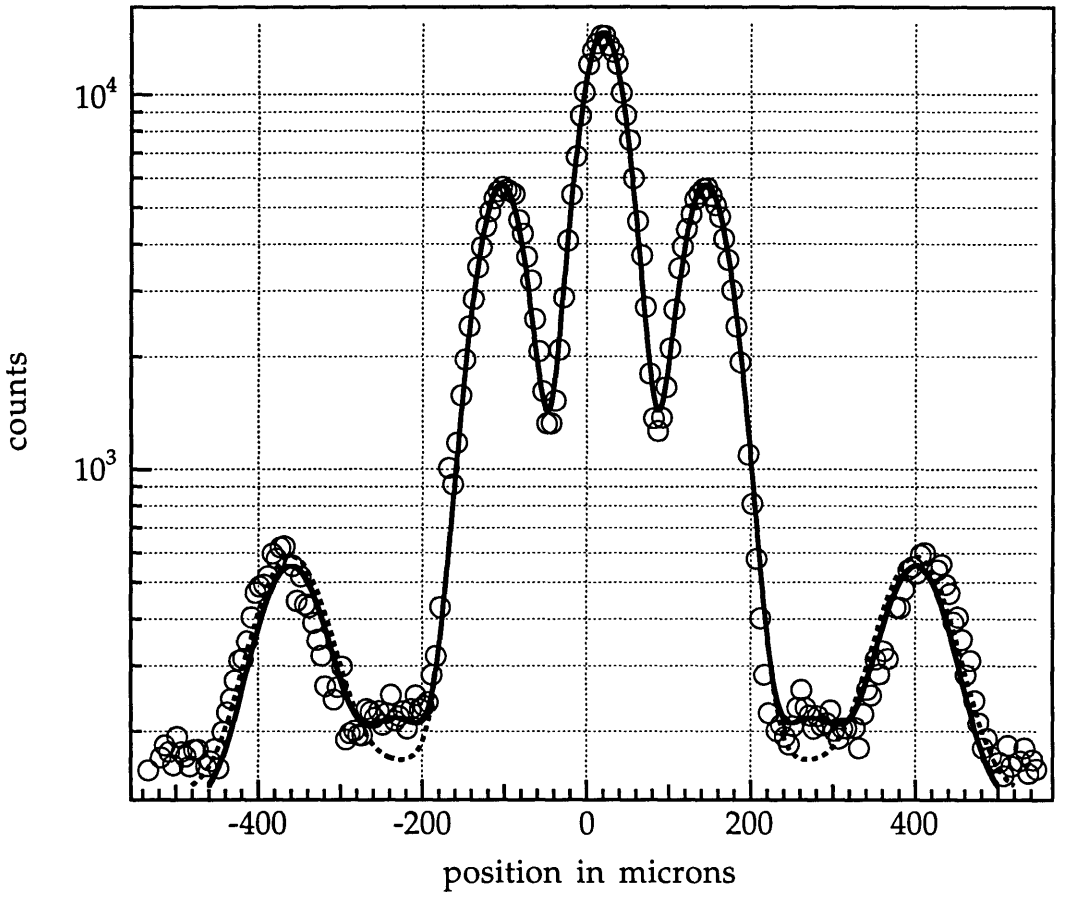

Figure 2.6: Diffraction of sodium atoms from a 200 nm period diffraction grating with $\beta = 0.50$. The solid line is a fit to the function described in the text, giving $\sigma_\beta = 0.73$. The dashed line is a fit with σ_β set to zero, which produces a poor fit at the heavily suppressed second order. Note the log scale, showing good visibility of the high diffracted orders.

Velocity widths

By the source by varying the carrier gas pressure we can produce relative velocity widths in the source that vary from 0.03 to 0.25. By fitting diffraction patterns from atomic beams produced with different carrier gas pressures, we can investigate the behavior of the velocity width as a function of carrier gas pressure. As expected, the velocity width increases with decreasing carrier gas pressure, with the limit of zero pressure and low sodium pressure being an effusive source. Figure 2.7 shows the relative velocity width as a function of source pressure.

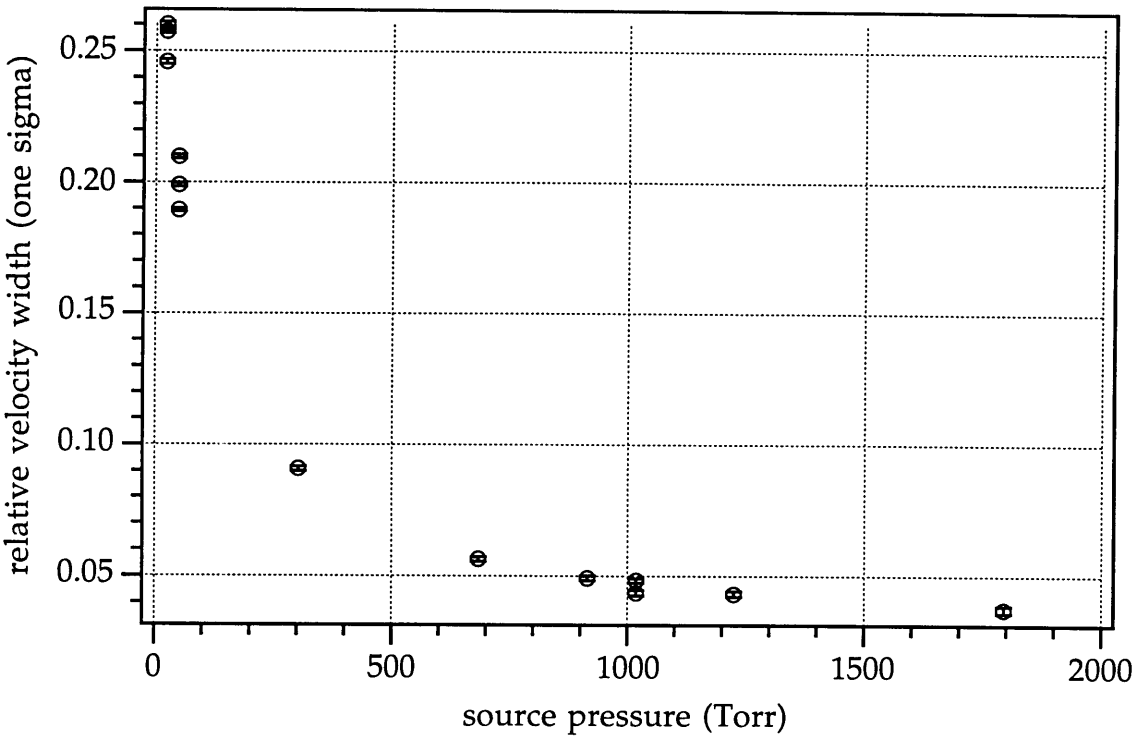

Figure 2.7: Relative velocity width of the atomic beam as a function of the argon carrier gas pressure. All of the data was taken with a nozzle diameter of 70 microns.

3 Theory

This chapter will cover the basic theory of the interferometer. This will include the addition of a potential in one beam, a prescription for carrying out an average over some perturbation that causes a phase shift, and an analysis of the contrast and interference amplitude in the interferometer as a function of the open fraction of the diffraction gratings. The coherence length of the beam will be dealt with as a special case of averaging over some perturbation, in this case, the velocity distribution. The chapter will end with a short discussion of the various quantum mechanical lengths present in the interferometer.

3.1 A potential in one arm of the interferometer

With the interaction region isolating the two beams of the interferometer, we can interact with each beam independently. The simplest case, which is very close to reality for many of the experiments, is to insert an external potential

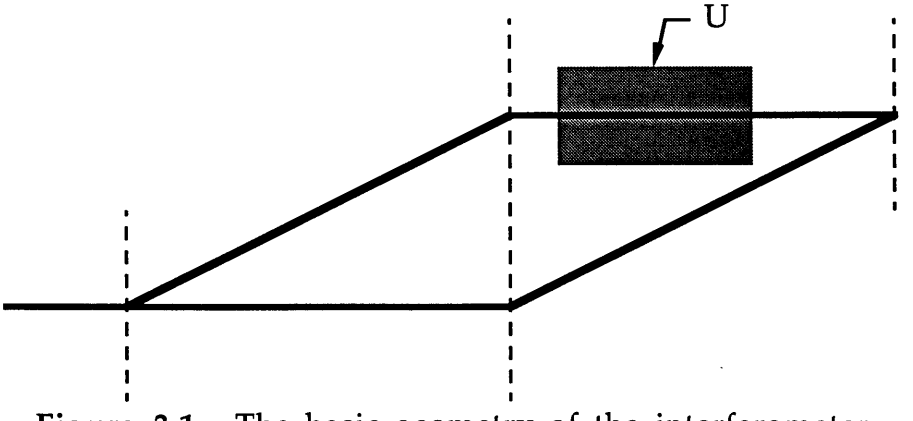

Figure 3.1: The basic geometry of the interferometer with a potential U inserted into one of the arms.

into one of the arms. The basic setup is shown in Figure 3.1, with the potential acting for a given length in one arm.

To calculate the effect of the potential on the interferometer, we must calculate the change in the "optical length" of the path when the potential is introduced. The phase is then shifted by 2π for each wavelength of path length change. The phase shift is

$$\begin{aligned}\Delta\varphi &= \int (k - k_0) ds \\ &= \int \Delta k ds\end{aligned}$$

in the JWKB approximation, where k_0 is the wave vector without the potential present, and k is the wave vector with the (possibly spatially dependent) potential present.

This integral can be greatly simplified by applying an eikonal approximation. This approximation is valid in the limit that the potential is much smaller than the energy of the particle, as is true for all of the experiments in this thesis. The mean particle energy is about .1 eV, and the typical applied potentials are about eight orders of magnitude smaller. The approximation follows

$$\begin{aligned}\Delta\varphi &= \int \Delta k ds \\ &= \int \left(\sqrt{\frac{2m}{\hbar^2}(E - U(x))} - \sqrt{\frac{2m}{\hbar^2} E} \right) ds \\ &= \sqrt{\frac{2m}{\hbar^2} E} \int \left(\sqrt{1 - \frac{U(x)}{E}} - 1 \right) ds \\ &\cong k_0 \int -\frac{U(x)}{2E} dx \\ &= \frac{1}{\hbar v_0} \int U(x) dx\end{aligned}$$

This result tells us that the phase shift is just proportional to the average value of the potential. It is also proportional to the length divided by the velocity, or the transit time. This will mean that except for the special case of potentials that increase linearly with the particle's velocity, such as the Aharonov-Casher phase shift discussed in chapter 9, there will be dispersion in the phase shift.

You can arrive at this result by just adding a phase factor of $e^{-iUt/\hbar}$ to the wave functions. This is an incorrect approach because the phase accumulates like $e^{-iEt/\hbar}$ in time dependent quantum mechanics, and E is conserved when the atom has different potential energies. The phase shift comes solely from the spatial part of the wave function.

3.2 Averaging over some perturbation

It is often necessary to average over some effect or distribution of interference patterns that will contribute to the signal from the interferometer. I will present here the basic method for predicting the phase shift from the average over a distribution of phase shifts. This will be used for adding in the effects of a velocity distribution and contrast loss due to phase drifts.

I will assume that the phase shift depends on some parameter a, and there is a probability distribution $P(a)$ that describes the distribution of the values of a over the measurement time. The interference pattern for a given value of a will look like

$$C_0 \cos(kx - \varphi(a)).$$

This must be averaged over the distribution $P(a)$ to give the measured pattern. The pattern is altered as follows.

$$\begin{aligned}\int P(a) C_0 \cos(kx - \varphi(a))\,da &= C_0 \int P(a)\big(\cos(kx)\cos(\varphi(a)) + \sin(kx)\sin(\varphi(a))\big)da \\ &= C_0\Big[\cos(kx)\int P(a)\cos(\varphi(a))\,da + \sin(kx)\int P(a)\sin(\varphi(a))\,da\Big] \\ &\equiv C(P(a):\varphi(a))\cos\big[kx - \varphi_{measured}(P(a):\varphi(a))\big]\end{aligned}$$

The realized contrast and phase shift depend on the form of the phase shift as a function of a, and the form of the distribution of $P(a)$. These are given by the following.

$$\tan\big[\varphi_{measured}(P(a):\varphi(a))\big] = \frac{\int P(a)\sin(\varphi(a))\,da}{\int P(a)\cos(\varphi(a))\,da}$$

$$C(P(a):\varphi(a)) = \sqrt{\Big(\int P(a)\sin(\varphi(a))\,da\Big)^2 + \Big(\int P(a)\cos(\varphi(a))\,da\Big)^2}$$

3.3 Optimum open fraction of the gratings

In this section I will present a calculation of how the contrast and the amplitude of the interference fringes depend on the open fraction of the three

gratings in the interferometer. The goals will be to find the optimum open fractions for maximum fringe intensity, contrast, and best phase determination. The i^{th} grating's open fraction (the ratio of slot size to bar size) will be β_i.

To calculate the intensity and contrast of the fringe pattern at the plane of the third grating, we must add up the amplitudes of the various paths to the place on the third grating where the fringes occur. For this calculation, I will only consider the paths shown in Figure 3.2. These are the only paths that arrive at the detector in our interferometer because the other paths are clipped off due to the width of the grating windows. The amplitudes for each path are identified in the figure.

The path lengths for A1 and A2 are the same, reflecting the white fringe nature of the interferometer (section 1.1). This means that there will be interference terms involving A1A2. The path length for A3 is approximately 10 nanometers longer than the paths for A1 or A2, which is much larger than the .6 Angstrom coherence length (section 3.4). This means that there will be no interference terms involving A3

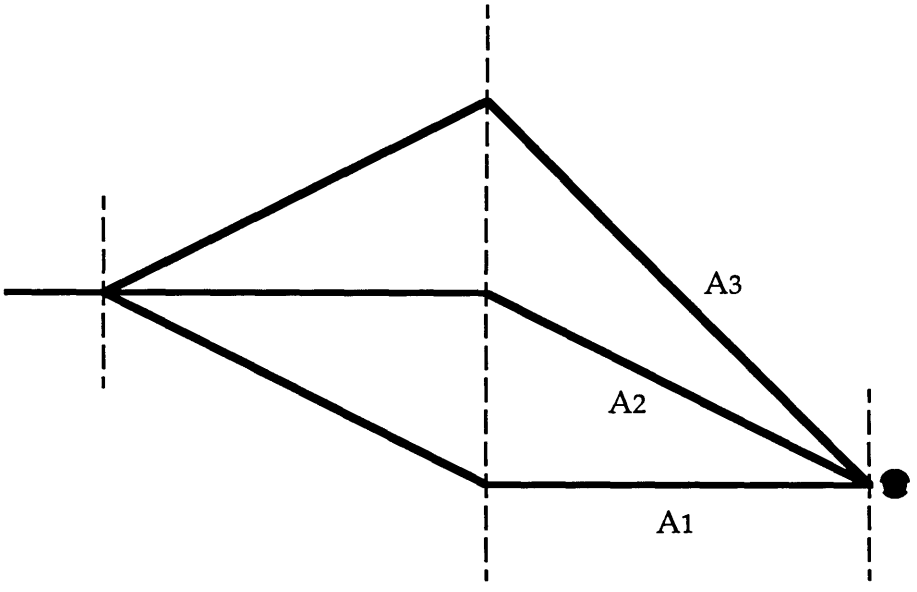

Figure 3.2: The paths that arrive at the detector considering the width of the grating windows. The amplitudes of the paths are A1, A2, and A3.

The amplitude in a diffraction order

The amplitude for a beam to make a diffractive "bend" into the n^{th} order through a grating is $\sin(n\pi\beta_i)/n\pi$. I will now justify this. The total transmitted flux through a grating that is illuminated with one unit of flux is the open fraction. The relative form factor for the grating is the single slit diffraction pattern for the slot between two grating bars with a slit of width βp, where p is the grating period. By summing up the intensities of all of the diffracted orders, multiplied by a normalization constant N, we can be sure that the sum should be β,

$$\beta = N\left[1+2\sum_{n=1}^{\infty}\frac{\sin^2(n\pi\beta)}{(n\pi\beta)^2}\right].$$

The sum in the above equation can be done in closed form,

$$\sum_{n=1}^{\infty}\frac{\sin^2(n\pi\beta)}{(n\pi\beta)^2}=\frac{1}{2\beta}-\frac{1}{2}.$$

By using the above results, we can solve for the constant N.

$$\beta = N\left[1+2\left(\frac{1}{2\beta}-\frac{1}{2}\right)\right]$$

$$N=\beta^2$$

This gives us the desired result for the amplitude to go into a given order with a given open fraction of the grating. The intensity of the n^{th} order is then

$$N\frac{\sin^2(n\pi\beta)}{(n\pi\beta)^2}=\frac{\sin^2(n\pi\beta)}{(n\pi)^2}.$$

This allows us to evaluate the three amplitudes for the beams that arrive at the detector as

$$A_1=\frac{\sin(\pi\beta_1)}{\pi}\frac{\sin(\pi\beta_2)}{\pi}$$

$$A_2=\beta_1\frac{\sin(\pi\beta_2)}{\pi}$$

$$A_3=\frac{\sin(\pi\beta_1)}{\pi}\frac{\sin(2\pi\beta_2)}{2\pi}.$$

Near field detection by the third grating

I will first deal with the amount of contrast and interference amplitude that survives the near field detection process illustrated in Figure 1.2. The fraction of the total flux that is transmitted through the third grating, averaged over grating positions, is β_3, the open fraction of the third grating. The amplitude of the transmitted fringes as a function of grating position and open fraction is found by multiplying a cosine function with a windowing function that is a grating with open fraction β_3. This gives a relative reduction in the transmitted fringe intensity of

$$\sin(\pi\beta_3)/\pi,$$

and a reduction in the contrast (relative to the standing wave atom pattern) of

$$\sin(\pi\beta_3)/\pi\beta_3.$$

The transmitted fringe intensity is maximized for $\beta_3 = 0.5$. While the contrast is maximized for $\beta_3 = 0$, no atoms get through the third grating.

Interfering amplitude

The amplitude of the interference pattern that is formed at the plane of the third grating is $2A_1A_2$. A_1 is the amplitude for a first order diffraction from the first grating multiplied by the amplitude for a first order diffraction from the second grating. A_2 is the amplitude for a zero order diffraction from the first grating multiplied by a first order diffraction from the second grating. A plot of this function is given in Figure 3.3. The maximum of this function is realized with β_1=0.65 and β_2 = 0.5. The maximum interfering amplitude as a function of the third grating's open fraction is realized for β_3 = 0.5.

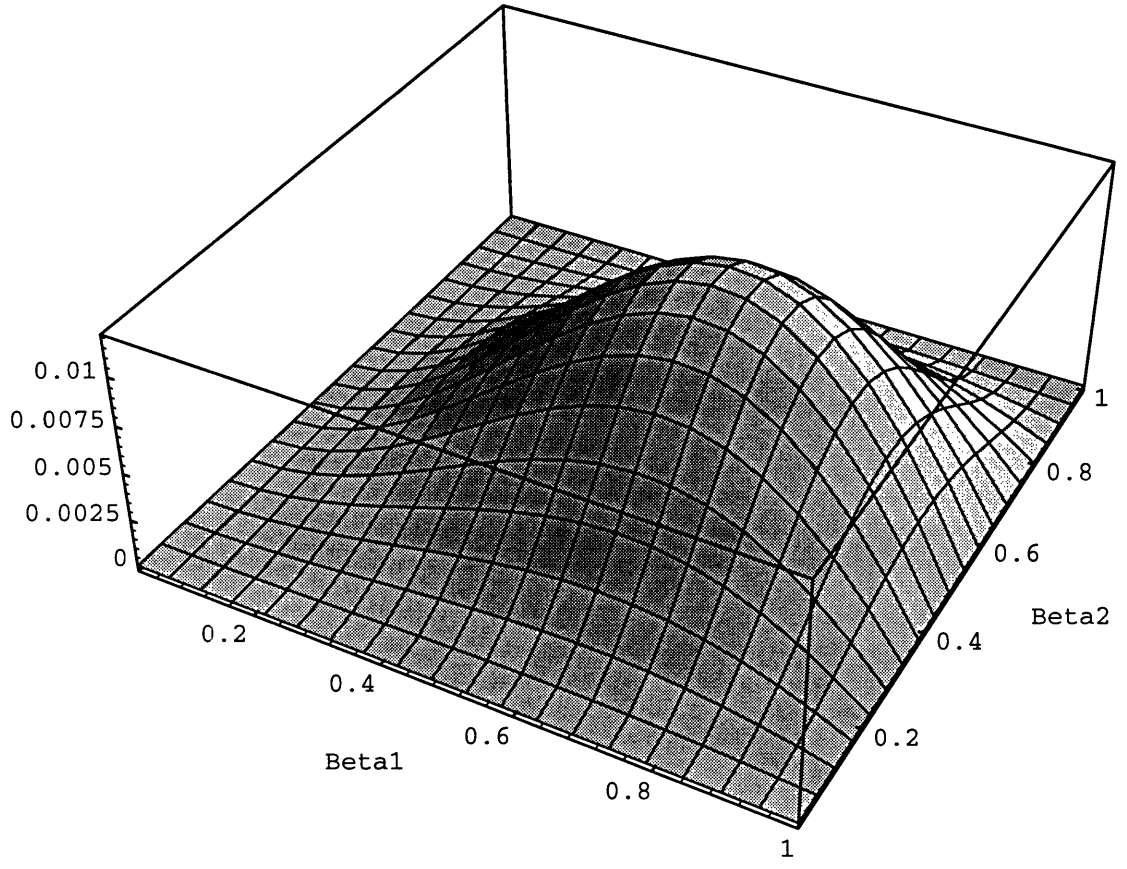

Figure 3.3: Interfering amplitude as a function of the open fraction of the first and second gratings. The magnitude is expressed as the fraction of the incident intensity of the atomic beam onto the interferometer.

Contrast

To find the contrast of the interference pattern we need the constant intensity at the third grating plane. This constant intensity is $A_1^2 + A_2^2 + A_3^2$. A_3 is the amplitude for a first order diffraction from the first grating multiplied by the amplitude for a second order diffraction from the second grating. The interfering amplitude divided by the constant intensity is the contrast. The contrast as a function of the open fractions of the first two gratings is shown in Figure 3.4. The maximum contrast is realized with β_1=0 and β_2 = 0.5. The maximum contrast as a function of the third grating's open fraction is realized for β_3 = 0. It is clear that, once again, while this may give the maximum contrast, no atoms get through the interferometer.

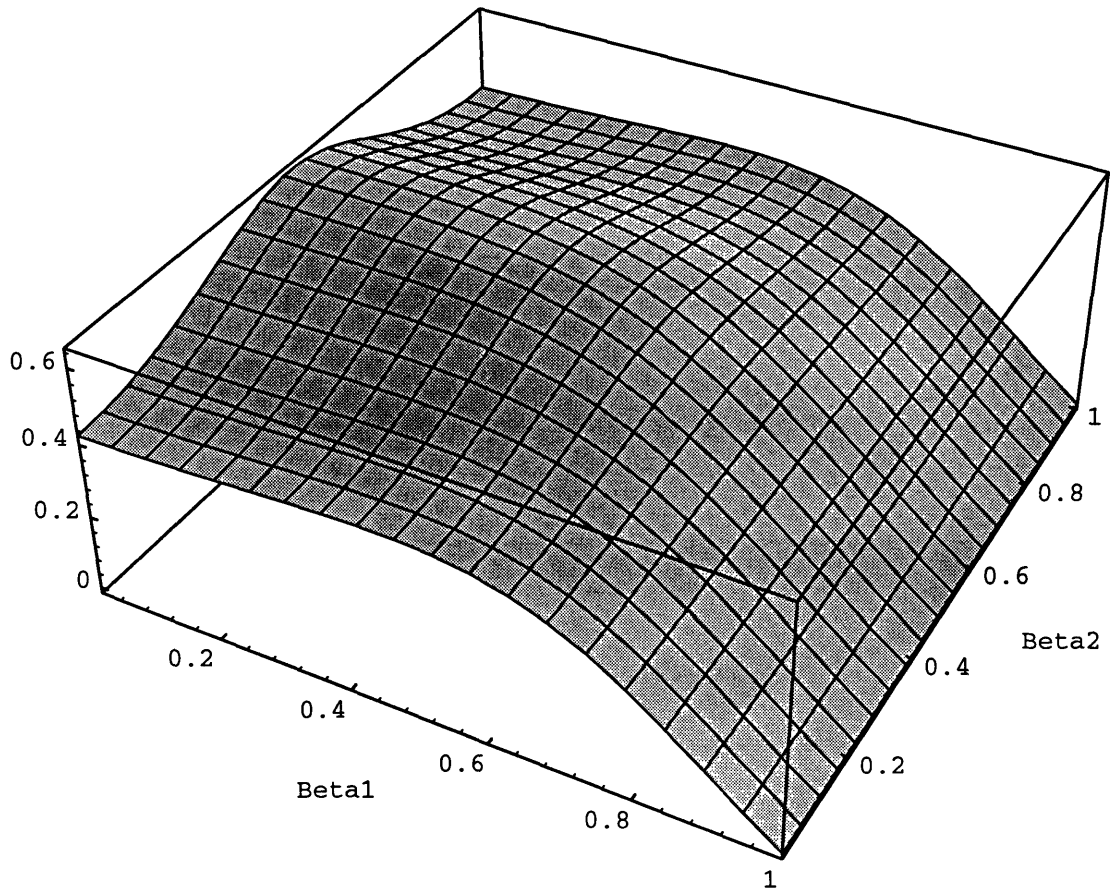

Figure 3.4: Contrast as a function of the open fraction of the first and second gratings.

Best phase determination

In almost all cases, what you want to do with an interferometer is to make the most accurate determination of the phase in a given time. The figure of merit for this is the square root of the transmitted intensity multiplied by the contrast. This figure of merit as a function of first and second grating open fraction is shown in Figure 3.5. The best phase determination is realized with β_1=0.56 and β_2 = 0.5. The best phase determination as a function of the third grating's open fraction is realized for β_3 = 0.37. This combination of open fractions gives a fringe amplitude at the detector that is 1.0% of the intensity incident on the first grating, with 67% contrast.

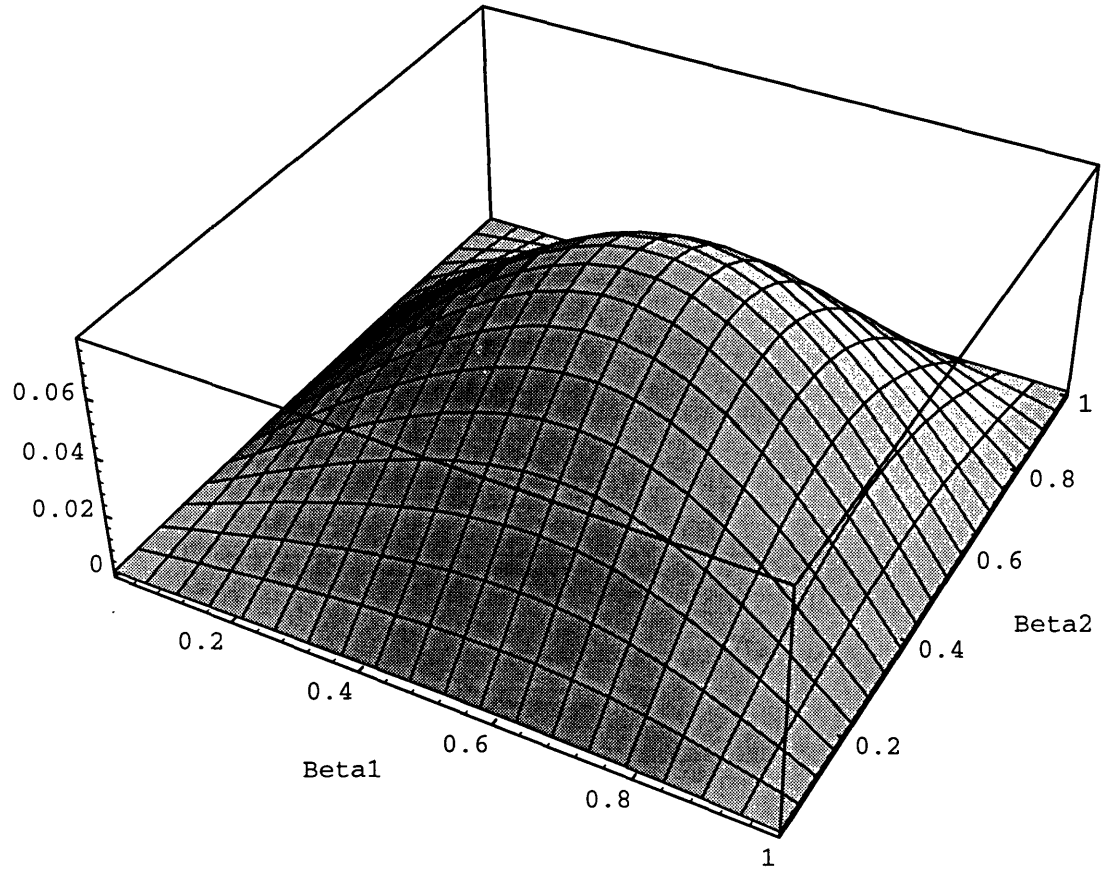

Figure 3.5: Best phase determination as a function of the open fraction of the first and second gratings. Units of the figure of merit are arbitrary.

3.4 Coherence length

The time evolution of a non-relativistic particle is quite different from that of a relativistic one, such as a photon. The key difference is that for non-relativistic particles, the vacuum is dispersive. In other words there is a definite dependence of propagation velocity on the wavelength of the particle. This is not very surprising, as it is just another way of saying that all other things being equal, non-relativistic particles with more energy move faster. One consequence of this is that a wave packet will spread due to its different momentum components.

The length of a wave packet does not in general tell us anything about the coherence length of the particle (or ensemble of particles). The coherence length is amount of additional path length that can be inserted into one arm of an interferometer and still have good contrast. As the additional path

length is increased, the contrast will decrease. For a gaussian wave packet, the length of the wave packet is equal to the coherence length only at the time when it is at its minimum size (the "focus" of the gaussian evolution) [KWG83, KOH83].

To calculate the loss of contrast as a function of phase shift with a given velocity distribution we use the results of section 3.2. In this case, the parameter that the phase shift depends on is the wave vector of the atom. The wide velocity distribution implies a wide wave vector distribution. For a gaussian distribution of wave vectors with a width σ_k, it can be easily verified that the contrast as a function of phase shift is:

$$C(\varphi:\sigma_k) \propto e^{-(\varphi\sigma_k)^2/2k_0^2}$$

where φ is the phase shift for the mean wave vector k_0 This means that the width of the contrast function with respect to interferometer phase is k_0/σ_k.

The translation to a coherence length is made by realizing that 2π of phase shift is one de Broglie wavelength of additional length.

$$\frac{k_0}{\sigma_k} = \frac{2\pi l_c}{\lambda}$$

$$l_c = \frac{k_0}{\sigma_k}\frac{h}{2\pi m v}$$

$$l_c = \frac{1}{\sigma_k}$$

This result looks quite familiar when written as $\hbar/\sigma_p$, which looks like an uncertainty principle limited length. This result can also be rearranged into another form, giving

$$l_c = \frac{\lambda_{dB}}{2\pi}\frac{v}{\sigma_v}.$$

This is roughly the one sigma speed ratio multiplied by the de Broglie wavelength.

We have applied many radians of phase shift to the interferometer and studied the coherence length of the beam. The phase shift was realized by applying an electric field to one beam. The details of the experiment are described in chapter 4, but for the purpose of this section, the applied electric field should be thought of as a phase knob on the interferometer.

When we plot the contrast of the interference pattern against applied phase shift, we obtain a pattern that reflects the finite coherence length of the beam. A plot of this type is shown in Figure 3.6.

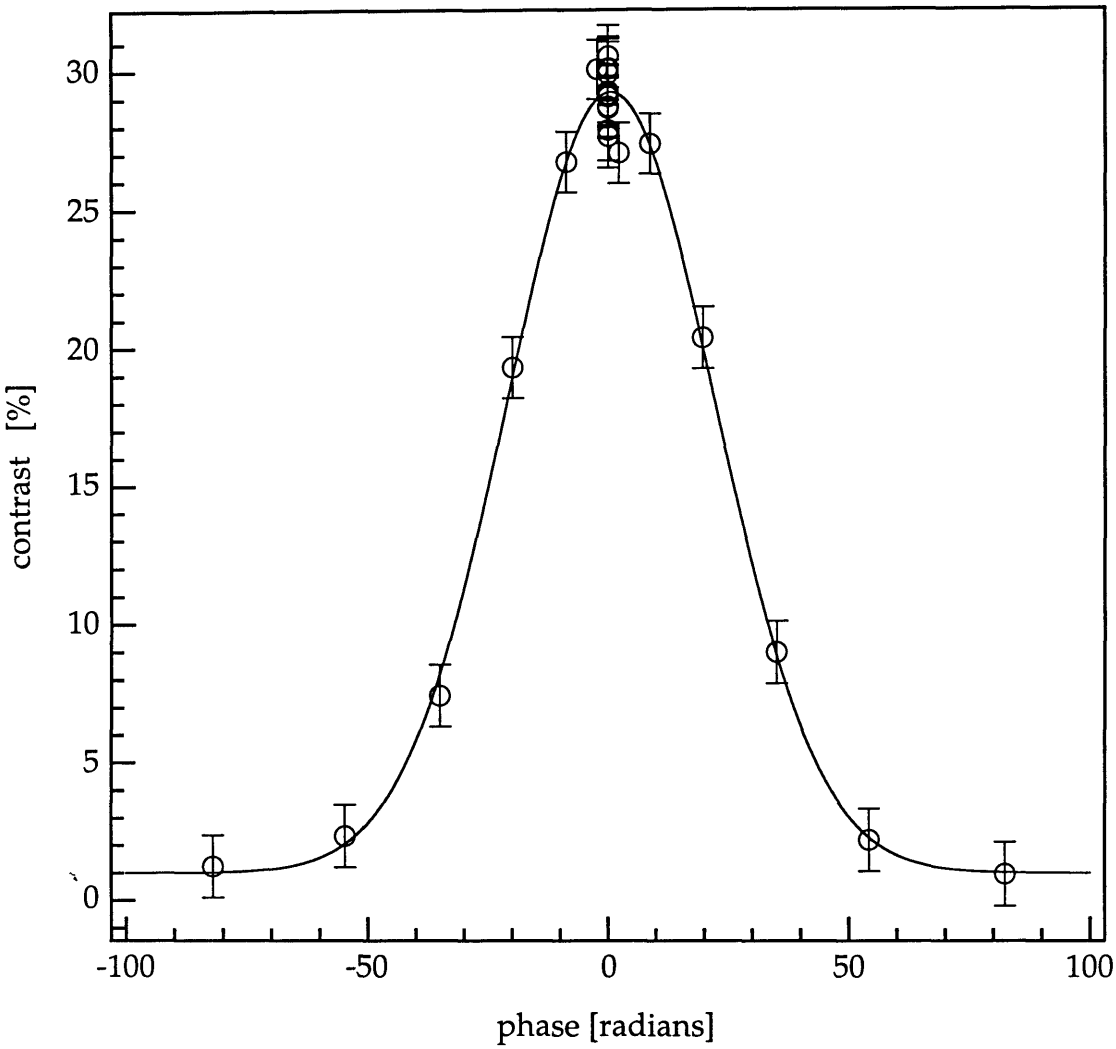

Figure 3.6: Interferometer contrast as a function of applied phase shift. The fit is to a gaussian, yielding a coherence length of .57 Angstroms.

By examining the coherence length of the beam in the interferometer, we can extract the width of the velocity distribution. This can be compared to the width that we find by fitting the diffraction pattern from the first grating. We have found good agreement between the velocity widths extracted from these two methods if the interaction region does not introduce additional phase inhomogenaities. The errors introduced by using a gaussian velocity

distribution instead of a v3 weighted gaussian are small for all of the experiments in this thesis, and are discussed in section 4.2.

3.5 The various quantum mechanical lengths in the interferometer

It is interesting to look at the various quantum mechanical lengths in the interferometer. There are four lengths that can be associated with the atom. The first and smallest length is the de Broglie wavelength. This is .16 angstroms for the beam using argon as the carrier gas. The next length is the coherence length, which is roughly .6 angstroms. The next largest length is physical size of the sodium atom in the ground state. For this length we can use the rms radius of the 3S state in sodium, which is about 3 angstroms, larger than either of the previous lengths associated with the center of mass motion of the atom.

The final length in the system is the "wave packet length". This has been encased in quotation marks because there are no wave packets in our beam, because we do not prepare them. If we did, by chopping the beam to a minimum uncertainty length wave packet corresponding to the velocity width just before the first grating in the interferometer, the wave packet would have spread to about 4 cm by the third grating. This is not very surprising. It is just a consequence of the interferometer being about 1 meter long and the speed ratio in the beam being about 4.

4 Polarizability of sodium

The first experiment that we conducted with the interferometer was to apply an electric field to one side of the interaction region and watch the fringes shift. This phase shift is caused by the quadratic Stark shift of the ground state, and allows us to determine the polarizability of the ground state of sodium.

Initially, this was intended to be a first demonstration experiment with the separated beam interferometer. We intended to do a rough measurement of the polarizability at the 2% to 5% level, publish, and get on to other experiments. When we analyzed the first set of data, we found that we had a statistical uncertainty of 0.4%. Then we got greedy. We set out to do a 0.1% measurement and quickly ran afoul of the systematic errors that will be discussed in this chapter. In the end, we ended up with a value that is good to 0.3% and spent about six months on the experiment.

The work in this chapter is written up in a paper that has been submitted to Physical Review Letters, included as section 4.2. The remainder of this chapter will only cover ground that had to be condensed or not included in the letter.

4.1 History of alkali measurements

The study of the Stark effect enjoyed a resurgence due to the tunable laser. All of these studies, however, looked only at the difference between the polarizabilities of two states. In other words, all experimental studies of the Stark shift of excited states have a common ground state shift subtracted. The study of ground state shifts of alkali atoms has previously relied on the transverse force on an atomic beam [HAZ74,MSM74]. Our work is the first in

which the effect of a constant electric field has produced a phase shift in an atomic state, and therefore given us a way to find the polarizability. A good overview of theoretical and experimental studies of atomic and molecular polarizabilities are given in two review articles by Miller and Bederson [MIB78,MIB88].

The electric polarizability of an atomic ground state is the lowest order description of the response to an electric field. It is therefore not surprising that this quantity paramatrizes a large number of phenomena and interactions in physics. One area that the polarizability appears is the long range interaction of atoms with electrons or ions, and other atoms. The polarizability parametrizes the interatomic attraction through the van der Walls constant in the Slater-Kirkwood approximation, and the dipole-quadrapole attractive term in a dominate level approximation. Other manifestations of the polarizability (really the interaction with electric fields) include: the Rayleigh scattering cross section, the ion mobility in a gas, and the Casmir-Polder effect.

4.2 Paper submitted to Phys. Rev. Lett.

Measurement of the Electric Polarizability of Sodium with an Atom Interferometer

Christopher R. Ekstrom, Jörg Schmiedmayer, Michael S. Chapman, Troy D. Hammond, and David E. Pritchard.

Department of Physics and Research Laboratory of Electronics
Massachusetts Institute of Technology, Cambridge, Massachusetts 02139, USA.

We have demonstrated an atom interferometer with interfering beams that are physically isolated by a metal foil. By applying an electric field to one beam of the interferometer, we have measured the phase shift resulting from the quadratic Stark effect. By studying these phase shifts, we have determined the ground state polarizability of sodium, with much improved precision, to be $24.08(5)_{\text{statistical}}(7)_{\text{systematic}} \times 10^{-24}$ cm^3.

PACS numbers: 35.10.Di, 07.60.Ly

Recently, there have been several atomic interference experiments that have culminated in the demonstration of atom interferometers[1-7] that are now beginning to be used as tools in the field of atomic physics.[8] We report in this letter an atom interferometer in which the two interfering beams are physically isolated by a metal foil, permitting the controlled application of different interactions to the two beams. We have used this interferometer to measure the polarizability of the ground state of sodium to 0.3% by applying a uniform electric field to one beam and examining the resulting phase shift.

The interferometer has a Mach-Zender geometry that uses three nanofabricated transmission gratings[9](Figure 1). Since the path length difference is zero for the central fringe for all velocities, or "colors", this geometry produces a robust white fringe.[10] The experimental apparatus has been considerably improved since our first demonstration experiment,[2] and has been described in detail elsewhere.[11] We now use 200 nm period gratings that separate the centers of the interfering beams by 55 μm at the position of the second grating, where the FWHM of the beam is 40 μm. An interaction region consisting of a stretched metal foil held symmetrically between two side electrodes is positioned between the beams. This septum is 10 μm thick, up to 10 cm long, and casts a shadow corresponding to a width of 20-30 μm on the detector. The mean velocity of the beam is 1050 m/s, corresponding to a deBroglie wavelength of 0.16 Å, with a typical velocity width of 4% rms.

With the septum between the beams of the interferometer, we have observed fringes with 35% contrast and an interference amplitude of more than 800 counts/s (Figure 2). We can determine the phase of the interference pattern with a precision of 10 mrad in one minute.

We now examine the effect of applying a potential $U(x)$ to one beam of the interferometer. The phase evolution of the wave function can be written within the JWKB approximation as $\psi(x) \propto e^{i\int k(x)dx}$, with the integration performed along the classical path. Here,

$$k(x) = \frac{1}{\hbar}\sqrt{2m(E-U(x))} \approx k_0 + \frac{1}{\hbar v}U(x)$$

where k_0 is the wave vector without the potential, $U(x)$ is the applied potential, and $v = \hbar k_0/m$. The approximation for $k(x)$ assumes $U(x)$ is much smaller than the energy ($U(x) \approx 10^{-8}E$ in our experiment).

If we apply a potential to only one beam, the resulting phase difference between the beams is:

$$\Delta\varphi(k) = \int k(x)ds - \int k_0 ds \approx \frac{1}{\hbar v}\int U(x)dx. \qquad (1)$$

This phase difference is the phase shift in the measured interference pattern.

In this experiment we apply a Stark potential $U = -\alpha\mathcal{E}^2/2$, were $\mathcal{E}$ is the applied electric field and α is the scalar electric polarizability. The polarizability parameterizes many important processes in atomic and molecular physics, including the index of refraction, the van der Waals constant between two polarizable systems, and the Rayleigh scattering cross section.[12]

To measure the polarizability, we subject one beam of the interferometer to a uniform electric field and record an interference pattern. The polarizability is determined from the phase shift of the interference pattern using Eqn. 1 with $\mathcal{E} = V/D$, yielding

$$\alpha = \left(\frac{\Delta\varphi_{Stark}}{V^2}\right)\left(\frac{D^2}{L_{eff}}\right)(2\hbar v), \qquad (2)$$

where L_{eff} is the effective interaction region length, V is the voltage applied to one side of the interaction region, D is the width of the spacer across which the voltage is applied, and v is the mean velocity of the atomic beam. We now examine each of the three terms in Eqn. 2, discussing their measurement and associated statistical and systematic errors.

To measure the first term of Eqn. 2, $\left(\Delta\varphi_{Stark}/V^2\right)$, we fit the phase shifts from several different voltages to a quadratic function of voltage (Figure 3). The phase for a given voltage is measured with respect to the phase with no voltage applied. This zero voltage reference phase changes with time. Typical long term drift rates are 1 rad/hour, but on a short time scale (30 sec) we find rms fluctuations as large as 150 mrad. To correct for these drifts and fluctuations, we take frequent measurements of the reference phase. In the fit, the quadratic term has a statistical uncertainty, typically 0.2%, dominated

by the phase measurement, but also includes residual scatter from the reference phase fluctuations. There are no significant systematic errors associated with this measurement.

The second term in Eqn. 2 depends only upon the geometry of the interaction region. We numerically calculated the electric fields of the interaction region and then evaluated the integral of $\mathcal{E}^2$ along the beam path. We define an effective length L_{eff} as

$$\left(\frac{V}{D}\right)^2 L_{eff} \equiv \int \mathcal{E}^2 \, dx.$$

These calculations yield an effective length that, due to fringing fields, is 3.0% shorter than the nominal physical length. The fringing fields at the end of the foil were minimized by guard electrodes, held at the same potential as the foil, located at the ends of the side plates (see Fig. 1). We have included an uncertainty in L_{eff} which contributes a 0.1% relative error in the determination of the polarizability. The spacer thickness D has been measured to 0.05% with a dial indicator. This error, combined with the effect of other dimensional uncertainties on the field calculations, produces a systematic error of less than 0.2%.

We found no statistically significant difference in the polarizability from measurements made with positive vs. negative voltages, indicating the absence of significant contact potentials. There was also no statistically significant difference between the left and right side of the interaction region, confirming interaction region symmetry to at least 0.2%.

The third term in Eqn. 2 is the velocity of the sodium beam. The mean velocity and the width of the velocity distribution are extracted from the diffraction pattern produced by the first grating with the second and third grating removed. The velocity is determined from the diffraction angle by,

$$\theta_{diff} = \frac{\lambda_{Na}}{d} = \frac{h}{m\mathrm{v}}\frac{1}{d}, \qquad (3)$$

where d is the grating period and $\lambda_{Na} = 2\pi/k_0$ is the deBroglie wavelength. A typical diffraction pattern, with a fit that determines the velocity to 0.15%, is shown in Figure 4.

In the limit of a monochromatic atomic beam, we have measured all the quantities in Eqn. 2 necessary to determine the polarizability. The finite velocity distribution of our beam complicates this simple analysis. The rms width of the velocity distribution varies between 3% and 5% and depends primarily on the carrier gas pressure and nozzle diameter of the seeded supersonic source. We can measure this width to 10% from the broadening of the high order peaks in the diffraction pattern or from the coherence length of our beam.[11]

We first consider the results of averaging over an arbitrary velocity distribution $P(v)$, which will effect the measured phase of the interference pattern. The measured phase will not be $\varphi(\bar{v})$, where $\bar{v}$ is the mean velocity, but will be given by

$$\tan(\varphi_{measured}) = \frac{\int P(v)\sin\varphi(v)dv}{\int P(v)\cos\varphi(v)dv}. \qquad (4)$$

The phase shift depends primarily on the mean velocity and, to a lesser extent, on the velocity width. It is only weakly dependent on the exact form of the distribution. We use a gaussian model function (instead of a more realistic v^3 weighted gaussian) for calculational convenience as there is no difference between the results at the 0.01% level. A similar velocity average is applied to the fit of the diffraction pattern, producing a 0.15% correction to the mean velocity found from Eqn. 3.

Because we use diffractive beam splitters in our interferometer, atoms from different velocity classes travel on different paths. Therefore, systematic errors can occur because the velocity distribution contributing to the interference pattern differs from the velocity distribution of the supersonic source, which is fit determined from the diffraction pattern.

In our experiment, there are two sources of this type of systematic velocity distribution change. One is the velocity selective blocking of atoms by the septum. Faster atoms have a smaller diffraction angle and, therefore, a larger chance of being blocked by the septum. The second is velocity selective detection of atoms. The same correlation between velocity and diffraction angle results in a correlation between the detector position and the velocity distribution of the atoms that are detected. These systematic effects are

modeled with a ray tracing algorithm. The calculation is performed for a variety of septum and detector positions, allowing us to find corrections to the measured phase shift and the contrast reduction for each experimental configuration.

We measured the polarizability at many positions of the interaction region within the interferometer. These measurements agreed with the predictions from the model, showing no variation in the polarizability at the 0.1% level for excursions of the septum that reduce the contrast to 50% of its peak value. This systematic is insignificant at our level of precision and required no correction.

We also measured the polarizability at several detector positions. These data showed a correlation between measured polarizability and detector position of 0.025% per micron, agreeing within errors to the model calculations. The resulting corrections of about 0.4%, which include the velocity average of Eqn. 4, introduced a systematic uncertainty of 0.15% in our determination of the polarizability.

To arrive at our final value, we performed polarizability measurements with three different interaction regions. The first and second had no guard electrodes and different length foils. The third interaction region had guard electrodes and provided the measurements that dominated the final result. These different electric field geometries gave consistent results. We find the electric polarizability of the sodium ground state to be $24.08(5)(7) \times 10^{-24}$ cm^3, where the first error is statistical and the second is systematic. The systematic error is dominated by uncertainties in the geometry of the interaction region, but also includes other geometric factors common to all measurements such as uncertainty in the grating period and the distance from the first grating to the detector which are used to find the velocity. Our statistical error is dominated by uncertainty in the determination of our velocity distribution, the short term stability of the phase reference in our experiment, and to a lesser extent by counting statistics.

Unlike the present work, previous measurements of alkali polarizabilities relied on the transverse force acting upon atoms in an electric field gradient. These efforts were limited by the knowledge of the exact value of the gradient and the field at the position of the atomic beam, giving $24.4(1.7)$[13] and $23.6(5) \times$

10^{-24} cm^3.[14] In another deflection experiment, the fringes from a Young's double slit have been shifted with an electric field gradient.[6] Our experiment has the advantage of applying a nominally uniform field and detecting a quantity that depends only on the field magnitude to measure the polarizability.

In conclusion, we have performed an interferometric measurement of the polarizability of the ground state of sodium. We have an uncertainty that is six times smaller than previous results. By performing a pulsed beam experiment with a better characterized interaction region, it should be possible to improve the accuracy of this measurement to below 0.1%.

Atom interferometers with physically separated beams open up the possibility of several other experiments, such as a measurement of the index of refraction of a gas for matter waves, a topological measurement of the Aharonov-Casher phase shift, and the measurement of Berry's phase for the wave function of a massive boson,[11] all of which require the ability to apply uniform, well controlled interactions to one portion of a split atom wave.

This work was supported by the Army Research Office contracts DAAL03-89-K-0082 and ASSERT 29970-PH-AAS, the Office of Naval Research contract N00014-89-J-1207, and the Joint Services Electronics Program contract DAAL03-89-C-0001. TDH acknowledges the support of a National Science Foundation graduate fellowship. JS acknowledges the support of an Erwin Schrödinger Fellowship of the Fond zur Förderung der Wissenschaftilchen Forschung in Austria.

References

1. Carnal, O. and Mlynek, J. *Phys. Rev. Lett.* **66**, 2689 (1991).

2. Keith, D.W., Ekstrom, C.R., Turchette, Q.A. and Pritchard, D.E. *Phys. Rev. Lett.* **66**, 2693 (1991).

3. Kasevich, M. and Chu, S. *Phys. Rev. Lett.* **67**, 181 (1991).

4. Riehle, F., Kisters, T., Witte, A., Helmcke, J. and Borde, J. *Phys. Rev. Lett.* **67**, 177 (1991).

5. Robert, J., Miniatura, C., Boiteux, S.L., Reinhardt, J., Bocvarski, V. and Baudon, J. *Europhys. Lett.* **16**, 29 (1991).

6. Shimizu, F., Shimizu, K. and Takuma, H. *Jpn. J. Appl. Phys.* **31**, L436 (1992).

7. A recent review of atom optics and atom interferometry is contained in the special issue: *Appl. Phys. B* **54**, *1992.* (1992).

8. Pritchard, D.E. *Atom Interferometers* in Atomic Physics 13, T.W. Hansch and H. Walther eds. (Munich, 1992).

9. Ekstrom, C.R., Keith, D.W. and Pritchard, D.E. *App. Phys. B* **54**, 369 (1992).

10. Chang, B.J., Alferness, R. and Leith, E.N. *Appl. Optics* **14**, 1592 (1975).

11. Schmiedmayer, J., Ekstrom, C.R., Chapman, M.S., Hammond, T.D. and Pritchard, D.E. *Atom Interferometry* in "Fundamentals of Quantum Optics 3" (Kühtai, 1993).

12. Miller, T.M. and Bederson, B. in *Advances in Atomic and Molecular Physics 13* 1-55 (1978).

13. Hall, W.D. and Zorn, J.C. *Phys. Rev. A* **10**, 1141 (1974).

14. Molof, R.W., Schwartz, H.L., Miller, T.M. and Bederson, B. *Phys. Rev. A* **10**, 1131 (1974).

Figures

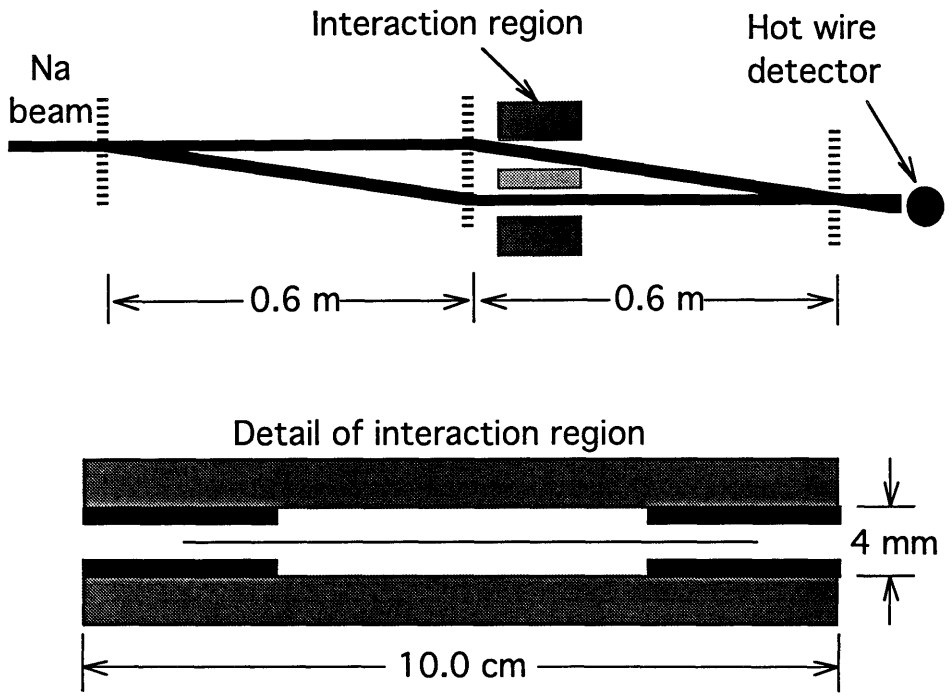

Figure 1: Schematic of our interferometer and interaction region. Vertical dashed lines are 200 nm period diffraction gratings. The detail of the interaction region shows the 10 micron copper foil suspended between the side plates. The guard electrodes are indicated in black at both ends.

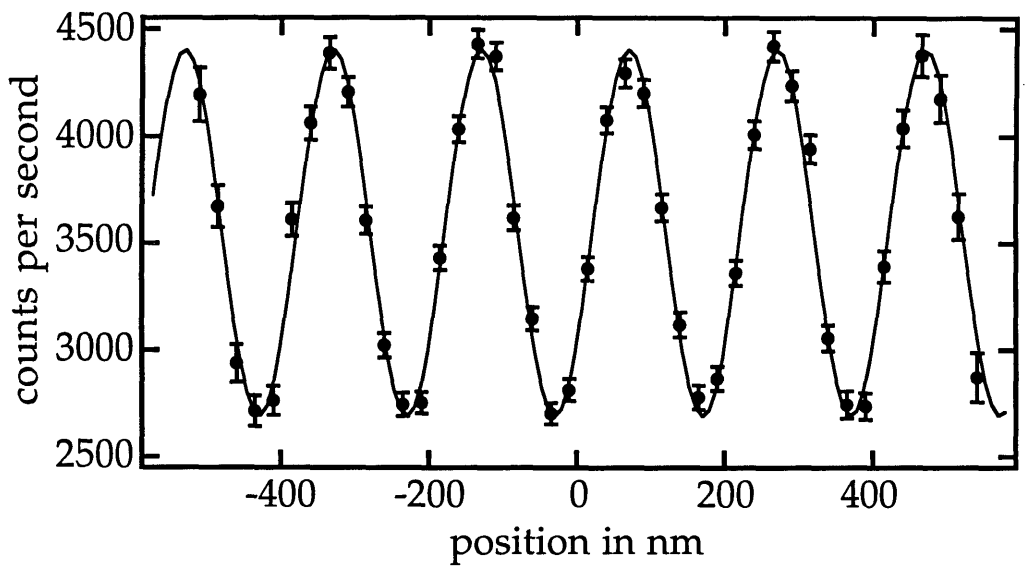

Figure 2: Interference pattern from 40 seconds of data (1 second per point). A constant background of 200 cps has been subtracted.

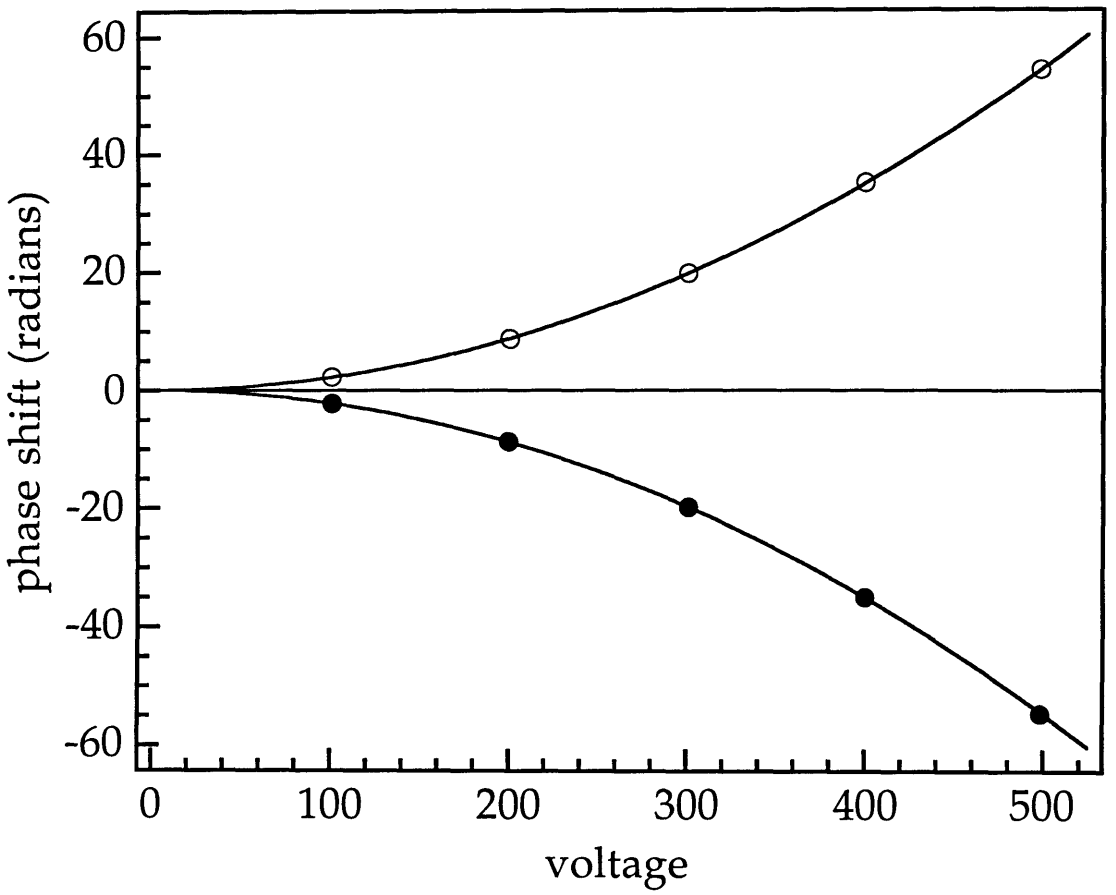

Figure 3: Phase shift of the interference pattern as a function of voltage applied to the left (open circles) or right (filled circles) side of the interaction region. Typical statistical error bars are contained within the markers. The fit is to a quadratic.

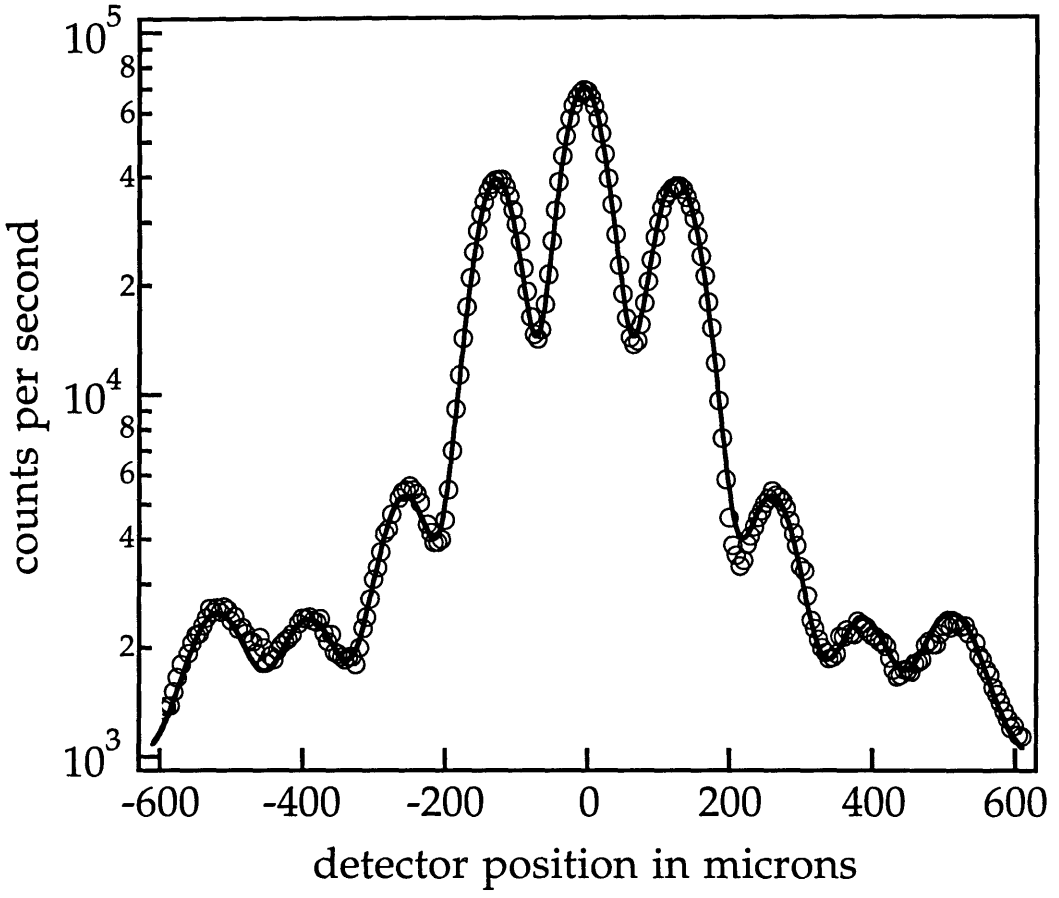

Figure 4: Diffraction pattern of sodium atoms from a 200 nm period grating. The solid line is calculated for a grating with average open fraction of 39.5%. The fit yields a mean velocity of 1040(2) m/s, λ_{dB} = 0.165 Å and a rms velocity width of 3.7(4)%.

4.3 Theory

I will now present two simple models for how you might calculate the polarizability of the ground state of sodium, with varying levels of sophistication. To give perspective to the results of each method, we have determined the polarizability to be $24.08(5)(7)\times10^{-24}$ cm^3.

Charged ball and spring

The ball and spring model of the polarizability is just about the simplest model you can think of. Take a particle with charge e and mass m on the end of a spring with an oscillation frequency ω. An external electric field with strength E is present. We now find the response of the system, and its energy shift.

The mass experiences a force in the direction of the field with magnitude eE. The displacement of the charge is found by balancing the forces

$$m\omega^2 x = eE$$

$$x = \frac{eE}{m\omega^2}$$

The dipole moment is the charge multiplied by its displacement , and is also the electric polarizability multiplied by the field.

$$ex = \frac{e^2 E}{m\omega^2} = \alpha E$$

$$\alpha = \frac{e^2}{m\omega^2}$$

This simple result is quite accurate for the sodium ground state because optically, it is connected most strongly to states at one optical frequency. You must use the frequency of the sodium D line for ω. This results in a polarizability of 24.9×10^{-24} cm^3.

Oscillator strengths

A more sophisticated analysis relies on perturbation theory using the sodium matrix elements. The first order in perturbation theory is

$$\Delta E^{(1)} = \langle g | e\vec{r} \cdot \vec{E} | g \rangle$$

and vanishes for any state with a definite parity.

Extending this to second order turns out to be the same as replacing the simple ball and stick model with a sum over a collection of oscillators, each weighted by its oscillator strength. The expectation value of the inverse square of the transition frequency is then written as

$$\left\langle \frac{1}{\omega^2} \right\rangle = \sum_i \frac{f_{0,i}}{\omega_{0i}^2}$$

where $f_{0,i}$ is the oscillator strength between the ground state and the excited state i, and ω_{0i} is the transition frequency between these two states. Because sodium is very much like a one electron atom, $\sum f_{0,i} \approx 1$. This alteration to the frequency is small, resulting in a polarizability of 24.5×10^{-24} cm^3.

Real calculations

More sophisticated calculations quickly get much more complex, without getting much more accurate. The review by Miller and Bederson [MIB78] has a good list of theoretical references.

4.4 Phase drifts

As was mentioned in the paper (section 4.2), the phase reference of the interferometer drifted with time. The behavior of the phase reference with respect to time is shown in Figure 4.1, showing a drift of approximately 1 Rad/hr. The current working theory on the cause of this drift is that fluctuations in the laser interferometer laser's intensity are translating into scale shifts in the detected relative position of the gratings. One other possible cause is the residual effects of temperature gradients in the machine. One way in which temperature gradients can effect the interferometer are by warping the beam tube that the entire experiment is housed within. This will result in the phase of the interference pattern shifting if transverse movement is imperfectly canceled by the laser interferometer servo system, or if vertical displacements couple into phase changes through imperfectly rotationally aligned gratings.

The short term fluctuations can be quite a bit larger. The rms of the phase differences from sample to sample on a minute time scale can be as large as 150 millradians. This could be caused by short term laser intensity fluctuations, which can be reduced by more frequent reversals or chopping in the experiment.

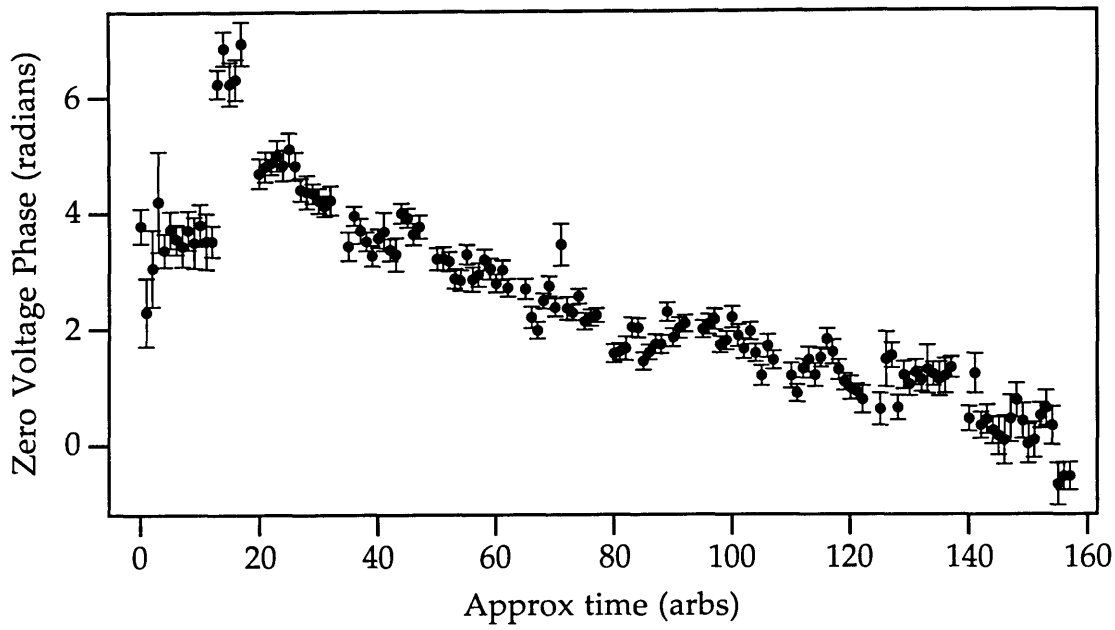

Figure 4.1: Drift of the reference phase in the interferometer with time.

4.5 Systematic errors and corrections

Interaction region field calculation

The electric field produced by the interaction region was modeled with a standard relaxation algorithm [PTV92]. The geometry of the interaction region is shown in Figure 4.2, viewed from above. An exploded view is shown in Figure 1.6. There were several important physical dimensions that we had to measure in the interaction region. The first is the thickness of the insulating spacers, which is discussed below. We also needed to know the distance between the guard electrodes. This was measured with a digital caliper to 25 microns. We needed to know the spacing from the guard electrode to the side plate as well, but to much lower accuracy. This was also measured to 25 microns with a digital caliper.

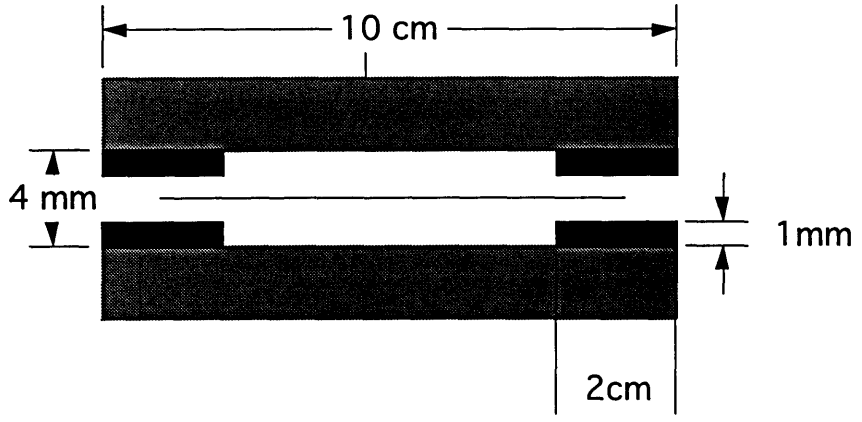

Figure 4.2: Detail of the interaction region viewed from above. The guard electrodes are shown in black and are held at the same potential as the metal foil. The side plates are shown in gray.

The relaxation code was run on our local Cray super computer with a 1 micron grid size. We then calculated the integral of the square of the electric field along different paths through the interaction region. For the final interaction region used in the experiment, the effective length was shorter from the nominal physical length by 0.3%.

Detector/septum clipping

Ray tracing code

Because we use diffractive beam splitters in our interferometer, atoms from different velocity classes travel on different paths. Therefore, systematic errors can occur because the velocity distribution contributing to the interference pattern differs from the velocity distribution of the supersonic source, which is fit determined from the diffraction pattern.

In our experiment, there are two sources of this type of systematic velocity distribution change. One is the velocity selective blocking of atoms by the septum. Faster atoms have a smaller diffraction angle and, therefore, a larger chance of being blocked by the septum. The second is velocity selective detection of atoms. The same correlation between velocity and diffraction angle results in a correlation between the detector position and the velocity distribution of the atoms that are detected.

To deal with these systematic effects, we used a numerical ray tracing algorithm. We also looked at the correlations of the measured polarizability with detector and septum position. The ray tracing code used an incoherent sum over paths through the interferometer. This produced an average phase

shift for a given location of the detector and interaction region. The algorithm is different from the one that was used to model the entire interferometer [TPK92,TUR92], which used a coherent sum of amplitudes over all paths.

The algorithm involved starting from each of several source points in the first collimation slit. The paths that lead to interference were identified by the transverse momentum change at each diffraction grating. Each set of interfering paths that arrived at a given location in the detector plane was evaluated for the difference in phase between the paths, and therefore the phase shift. The interaction region was included as a phase shift in certain paths with the size of the object determined by the interaction region field calculation. The physical size of the metal septum was included as an opaque object that occluded some of the possible paths through the interferometer. The results were averaged over an extended source, and an initial velocity distribution.

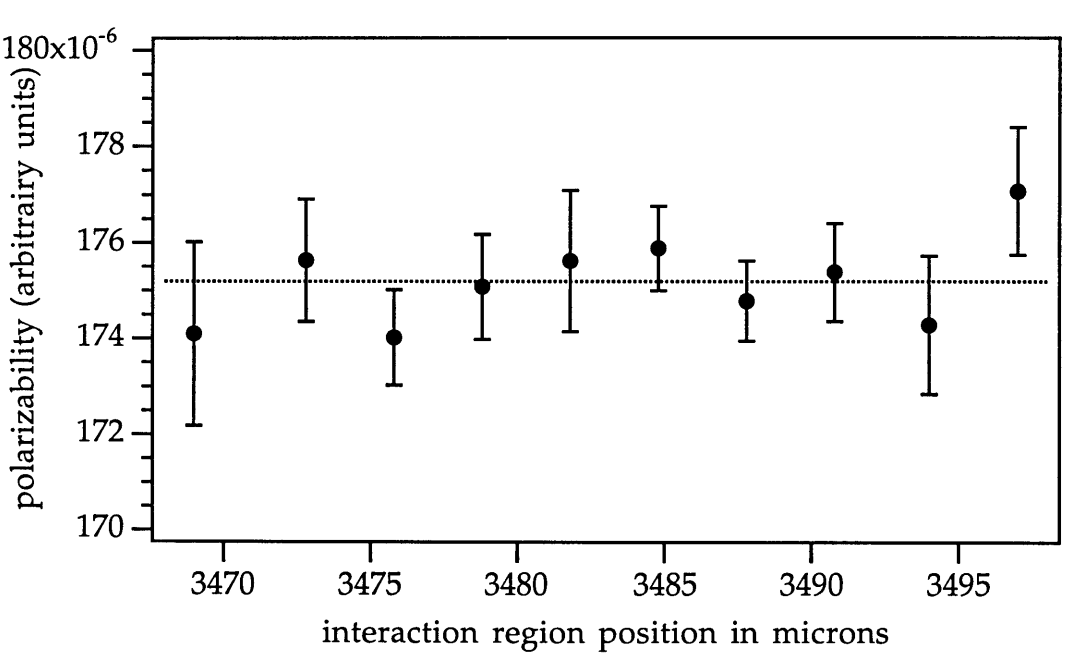

Figure 4.3: Change in the measured polarizability with interaction region position. The dashed line is the average of the measurements. These measurements show no linear correlation with interaction region position.

By altering the transverse position of the interaction region and therefore the septum, we could predict the correlation between interaction region position

and realized phase shift. These correlations were all small, as discussed in the paper. Figure 4.3 shows the results of these measurements taken with several interaction region positions, which were converted to polarizability units as outlined in section 4.2.

Polarizability vs. detector position

By running the simulation for several different detector positions, we could predict the amount of correlation between measured phase shift and detector position. The results of polarizability measurements taken at several different detector positions is shown in Figure 4.4 and agrees within errors with the simulations. These results were converted to polarizability units as outlined in section 4.2.

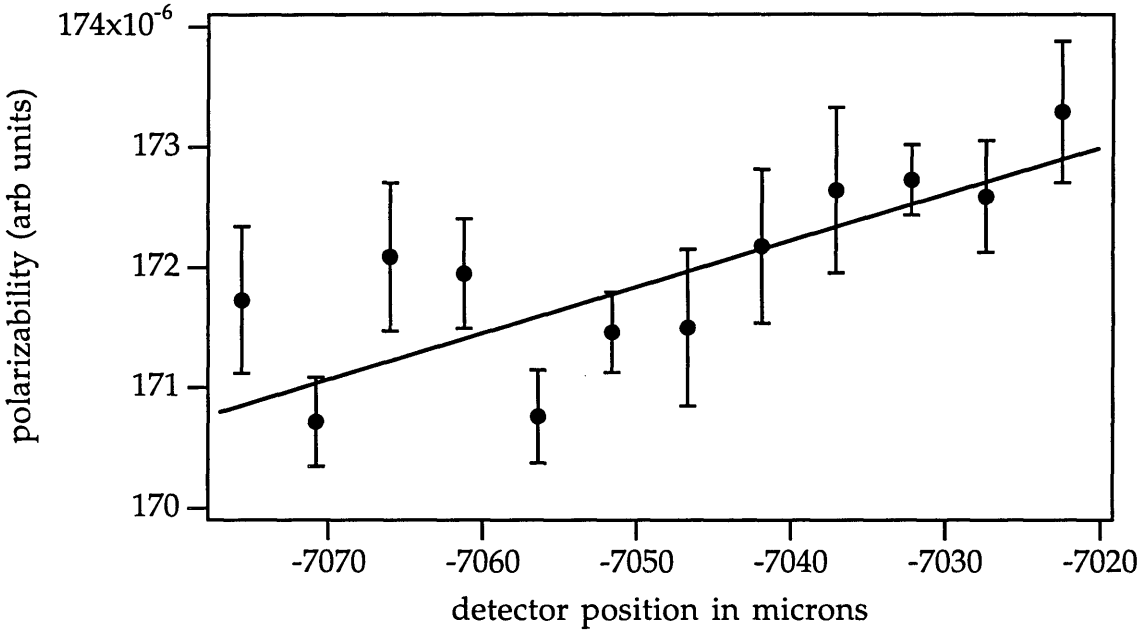

Figure 4.4: Change in the measured polarizability with detector position. The solid line is a linear fit to the data.

4.6 Physical measurements

There were several physical dimensions that needed to be measured to determine the polarizability. In this section I will describe in detail how they were measured.

The interaction region spacers

To find the electric field seen by the atoms, we need to know the voltage that was applied to the interaction region, and the distance that it was applied

across. The distance is determined by the alumina spacers that hold the side plates and the metal foil apart. We wanted to know the thickness of the spacers, which were supposed to be 2 mm thick, with a 1 micron tolerance. The spacers were made by the San Jose Delta company, and were specified to 1.3 microns (actually 0.05 thousandths of an inch).

Measuring a physical dimension to one micron is not a trivial task (although it is easier than the method we actually used). The basic measuring tool was a Mitutoyo digital dial indicator. This indicator has a precision of one micron, but an accuracy of only four microns. The indicator was mounted over a good granite block (Starrett Grade A inspection plate, "master pink"), that is flat to 2.5 microns over 12 inches. We used only about 3 inches of this block.

The system still needs to be calibrated to reach the desired accuracy of one micron. This was accomplished by measuring several gauge blocks (2, 2.25, and 2.5 mm) that are all calibrated to 50 nm. We were all surprised at how good the gauge blocks were (we used the worst grade available). The flatness is as good as a lambda/10 mirror. They also have the added attraction of being NIST traceable.

We measured several spacers, including pieces of broken spacers which should give the same value. The broken pieces gave the same values, and the gauge blocks all measured the same each time they were removed and replaced from the measuring apparatus. The rms of the measurements were all less than 1 micron, but all of the spacers were not at all within specifications. While all of the spacers that were measured were flat to within 1 micron, very few were the correct thickness. We had to end up measuring each spacer and its position in the interaction region to find the spacing at the location of the atomic beam. The spacers varied by as much as five microns, not a very impressive fabrication job.

The grating period

To convert from the separation of the diffraction orders in a diffraction pattern to a velocity we need to know the period of the diffraction gratings. The grating period was determined from SEM pictures. While measuring almost anything on an absolute scale from a SEM picture is a dubious practice at best (due to the projection onto the imaging system from the sample), I will now describe the measurement process.

To describe the method, I will need to introduce a few details of the electron beam lithography system. Much of this is covered in an article from Applied Physics B that is included as section 1.3. The e-beam writer (a JEOL JBX5DII) writes fields that were set to 50 micron squares. The writer moves a translation stage to "stitch" fields together to write large patterns. These stage moves are monitored by a Hewlett Packard laser interferometer ranging system in two dimensions that is accurate to 2 nm (once again, NIST traceable). This means that the 50 micron stage move is accurate to 0.004%.

The size of the error at a field boundary is measured in grating periods. This error is typically 0.1 periods, the practical limit of this measurement method. The 10% measurement is leveraged up by a factor that is the field size measured in grating periods (250 for 200 nm period gratings). This yields an uncertainty in the grating period of one part in 2500.

The measurement is made by assuming that no whole periods of a diffraction grating are "missed" by stitching errors. I have made this assumption on the basis of a series of tests of the field stitch tests made with verniers written across field boundaries that never showed more than one half period stitching errors for fields that were written one after another.

Distance from the first grating to the detector

Another quantity that is necessary for the determination of the velocity is the distance from the first grating to the detector. This allows the peak separation in the diffraction pattern to be converted into a diffraction angle. This is measured by measuring the distance between flanges that hold the detector and the first grating from the outside of the machine to 1 mm. The location of the detector wire and the first grating relative to their respective flanges are determined much more accurately by measurement with dial micrometers to several thousandths of an inch (approximately 100 microns).

4.7 The final number

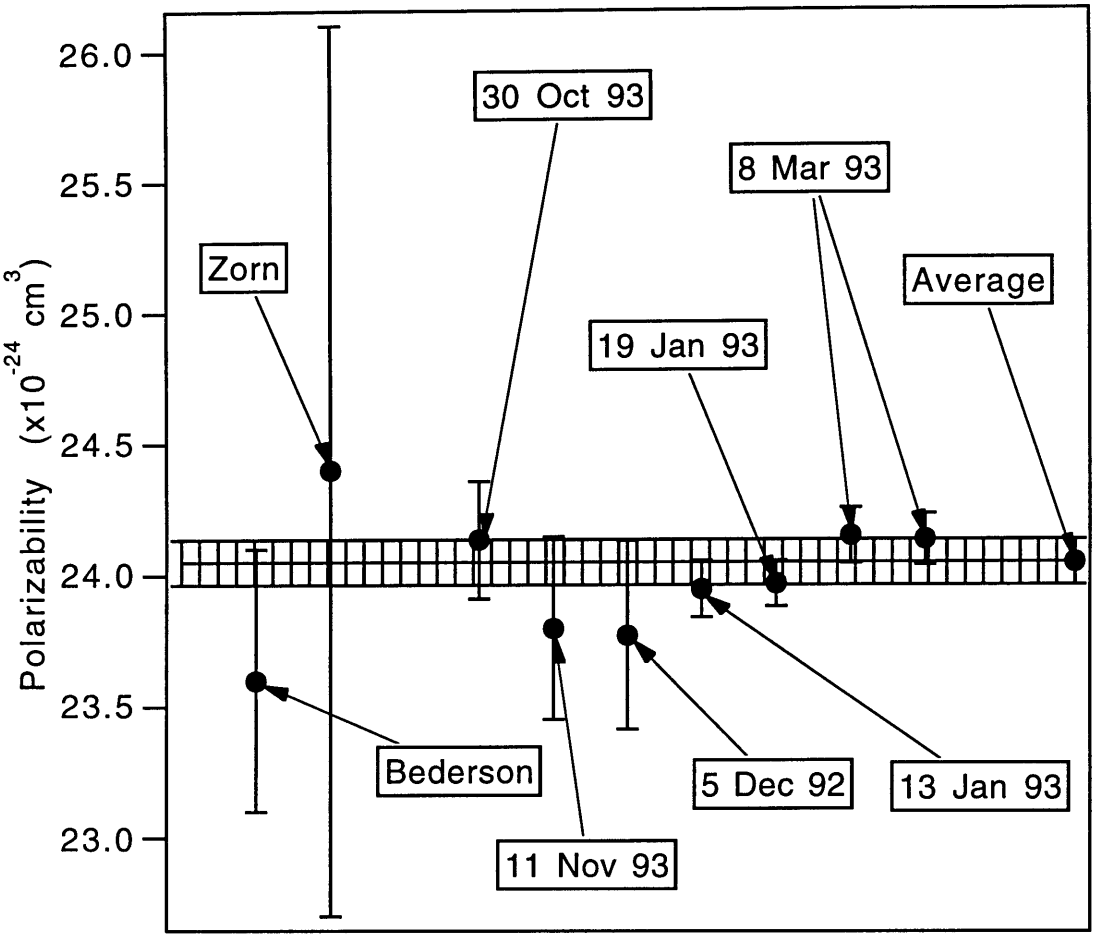

Figure 4.5: The measurements that lead to our value of the polarizability (average). The experimental results of Zorn [HAZ74] and Bederson [MSM74] are also included. In this figure, the statistical and systematic error bars for each point have been added in quadrature.

The final number was determined by several different measurements. Figure 4.5 shows the different measurements, and our final result. The October 30 value is dominated by statistical errors in the velocity determination. The November 11 and December 5 values are dominated by uncertainty in the length of the septum. The final four values determine the average, and were all performed with an interaction region that had the guard electrodes shown in Figure 4.2.

The table in Figure 4.6 shows the various error sources discussed in this chapter and their effect on the final errors. All errors are relative and the

number reflects the total effect on the final number's errors, so some are the typical error for a given measurement, and some are de-weighted by averaging over several measurements.

Error source	systematic error	statistical error
Spacer width	0.07%	
Grating period	0.05%	
Velocity		0.12%
1g - det distance	0.06%	
Interaction region length	0.08%	
Field calculation correction	0.10%	
Fit to $\Delta\varphi$ per E^2		0.15%
Corrections from ray tracing	0.15%	
Total	0.25%	0.21%

Figure 4.6: Relative contributions of the various error sources.

5 Magnetic rephasing

Another experiment that was made possible by the basic interaction region is called magnetic rephasing. In this experiment, the basic variable measured from the interference pattern in the contrast, which is highest when a number of different types of atoms experience different phase shifts that nevertheless line up their interference patterns. This experiment is closely related to the spin 1/2 rotation experiment in a neutron interferometer [RZB75]. Our experiment performs spin rotations of all of the spin projections of a spin two and a spin one state.

5.1 The experimental setup

The experimental setup uses the same conductive septum and interaction region as used in the polarizability measurement. There are two electrical connections to the septum, one at the top and one at the bottom, located in the center of the foil. This allows a current to flow down the septum, through the plane of the interferometer.

The experimental configuration of the interaction region and the resulting magnetic fields are shown in Figure 5.1. A nominally uniform external magnetic field is imposed over the entire interaction region area. The field is produced by three sets of "Helmholtz-ish" field coils wound around the cross at the second grating flange that houses the interaction region. This magnetic field is directed along the beam axis (z axis), and is typically 3-4 Gauss. This will be the largest magnetic field in the experiment and will be the major constituent of the local magnetic field, which will provide the quantization axis for the experiment.

The unpolarized sodium beam has two hyperfine ground states having total angular momentum F of 2 and 1. These two states have g-factors that are the same in magnitude, but have opposite sign. This means that there will be one state (F=2, m_F=2) with one Bohr magneton of magnetic moment projection along the z-axis, two with half a Bohr magneton (F=2 and 1, m_F=1,-1), two with no projection (F=2 and 1, m_F=0), two with minus one half (F=2 and 1, m_F=-1,1), and one with minus one Born Magneton (F=2 , m_F=-2). At this point there is no shift in the phase of the interference pattern because there is no difference in the phase accumulated on the two sides of the foil, assuming that there is no magnetic field gradient across the interferometer.

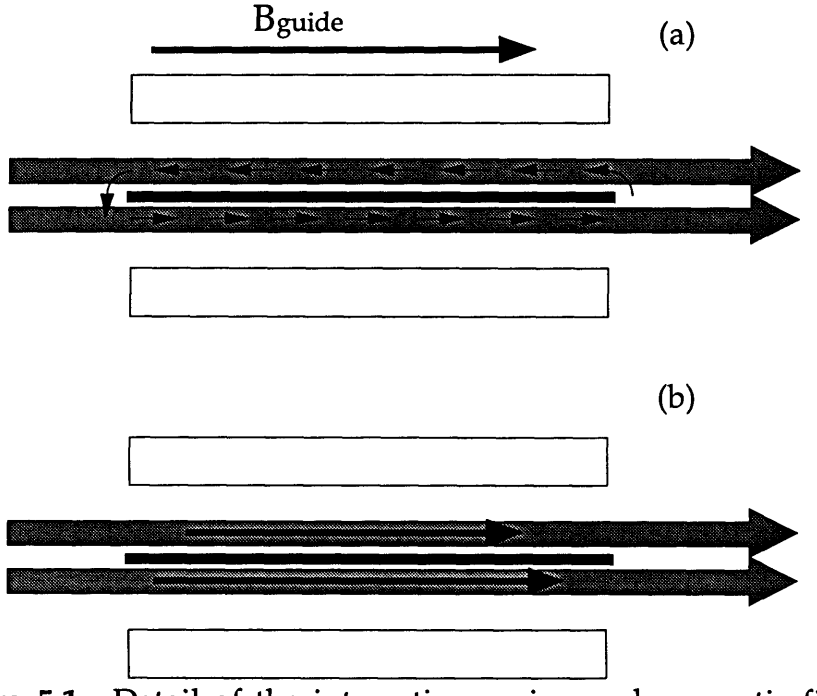

Figure 5.1: Detail of the interaction region and magnetic fields for the rephasing experiment. The dark arrows are magnetic fields, and the light arrows represent the atomic beams. In (a), the large guide field is shown above the interaction region. There is a current flowing up out of the page that creates the field circulating around the foil. In (b) the resulting fields are shown for each beam, their different lengths cause different Zeeman phase accumulation for the two beams.

A current is then passed down the foil, through the plane of the interferometer. This forms a current sheet that creates a magnetic field. This field points along the guide field on one side of the foil and against the guide

field on the other. This has the effect of shortening the guide field for one path, and lengthening it for the other path.

This difference in the strength of the guide fields, and therefore a difference in the accumulation of phase, will result in a differential Zeeman phase shift of the interference pattern for each magnetic moment projection. The total interference pattern is the incoherent sum of the patterns produced by the individual magnetic moment projections, each with a different phase and contrast. The paths of the two beams form, to a very good approximation, a Amperian loop about the current distribution. If we assume that there is an angle theta between the local magnetic field and the propagation direction of the atoms, and the current flows straight down the foil, we can use Ampere's law to find the differential phase shift for a given magnetic moment projection. This phase shift is

$$\Delta\varphi_m = \frac{4\pi}{\hbar c}\frac{\mu_m I}{v}\cos(\theta),$$

where I is the current flowing down the septum. This assumes that there is a constant angle between the local magnetic field and the beam direction. A more realistic treatment must average this misalignment over the path arriving at an expression with a "fudge factor" $\langle\cos(\theta)\rangle$

$$\Delta\varphi_m = \frac{4\pi}{\hbar c}\frac{\mu_m I}{v}\langle\cos(\theta)\rangle$$

In the limit of a monochromatic atomic beam the form of the contrast of the interference pattern as a function of septum current is fairly simple. In this limit, the contrast is

$$\begin{aligned} C &= \frac{C_0}{8}\left[\cos(\varphi) + 2\cos\left(\frac{\varphi}{2}\right) + 2 + 2\cos\left(-\frac{\varphi}{2}\right) + \cos(-\varphi)\right] \\ &= \frac{C_0}{4}\left[\cos(\varphi) + 2\cos\left(\frac{\varphi}{2}\right) + 1\right] \end{aligned}$$

where φ is the phase shift (the Δ has been dropped) applied to the state with one Bohr magneton of magnetic moment projection (the "stretched state"), and C_0 is the initial contrast. The function simplifies to

$$C_0\cos^2\left(\frac{\varphi}{4}\right)\cos\left(\frac{\varphi}{2}\right).$$

This function is plotted in Figure 5.2. As expected, when small amounts of phase shift are applied (experimentally by turning up the current flowing down the foil), the contrast degrades. The first interesting feature occurs when the phase shift applied to the stretched state is 4π. The phase shift of the four states with $|m|=1$ is then 2π. At this point, all of the interference patterns have the same phase modulo 2π, and high contrast fringes should reappear because all of the interference patterns will line up with each other. The same conditions will be fulfilled for every additional 4π of phase shift applied to the stretched state.

Another interesting feature of this contrast function is that there are regions with low contrast that have a phase shift of π, with the other regions having no phase shift, and sudden transitions between them.

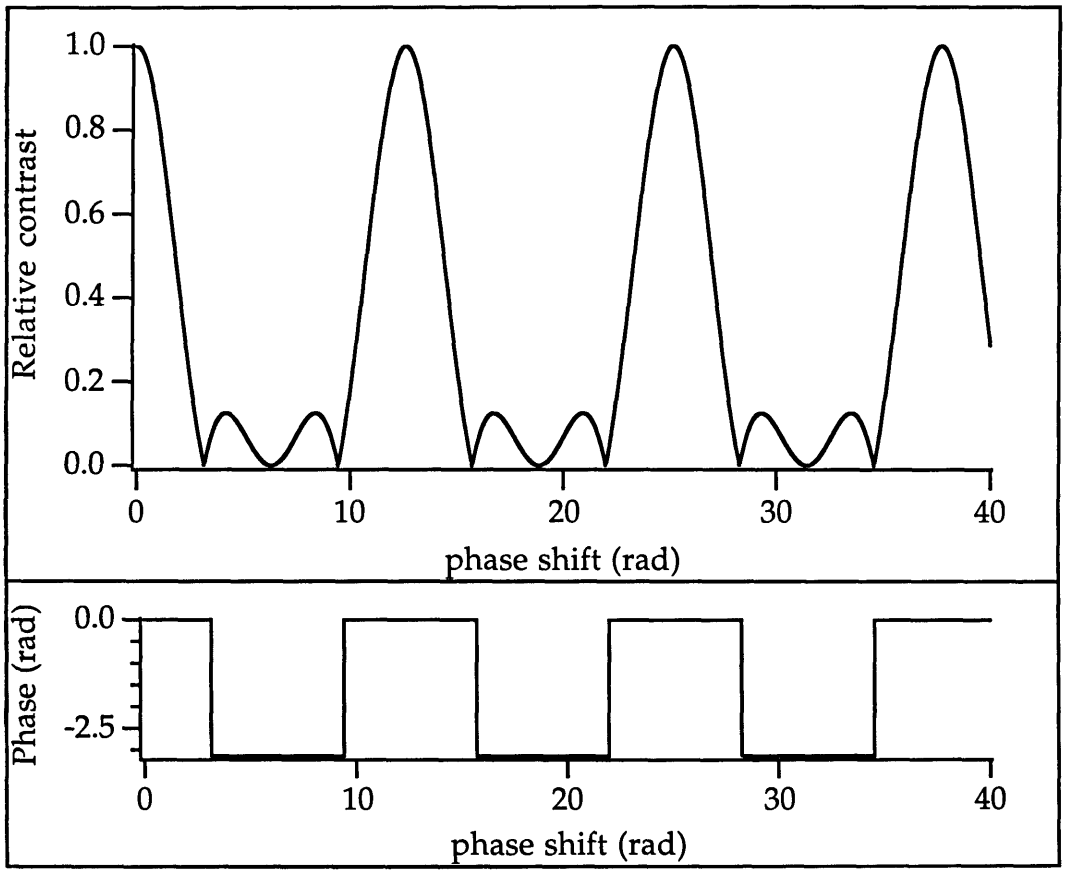

Figure 5.2: Contrast and phase of the interference pattern versus phase shift applied to the stretched state.

The situation is complicated by the velocity distribution and therefore finite coherence length of the atomic beam. The contrast of the interference pattern

for any state decreases like a gaussian function of the applied phase shift for that state (see section 3.4). The contrast is then

$$\frac{C_0}{4}\left[P(\varphi)\cos(\varphi)+2P\left(\frac{\varphi}{2}\right)\cos\left(\frac{\varphi}{2}\right)+1\right]$$

where P is the relative loss of contrast as a function of the applied phase. At large applied phase shifts, the contrast damps out to a level that is one quarter of the original contrast. This is the contribution of the two states that has no projection of their magnetic moment along the guide field, and therefore no phase shift as a result of the current in the foil.

Throughout this discussion, I have ignored the curvature in the Zeeman manifolds. This is because we operate at total magnetic fields of approximately 5 Gauss, while the decoupling of the Zeeman states occurs at several hundred Gauss.

5.2 Experimental results

This section contains data from two magnetic rephasing experiments. The first set of data is well accounted for by the simple theory outlined in the previous section. It appears in Figure 5.3 with a fit to the function described at the end of section 5.1. It is clear that the maximum contrast is not realized for zero current flowing through the septum. This is the result of a small magnetic field gradient across the machine, which produces a differential Zeeman phase shift for zero current.

By fitting the data in Figure 5.3 we can extract the velocity from the amount of current required for each contrast revival. This data yields a velocity of 1088(4) m/s if we do not include the $\langle\cos(\theta)\rangle$ fudge factor. Diffraction data taken during the same run yields a velocity of 1071(3) m/s, which we trust. This implies an average local field misalignment that corresponds to $\langle\cos(\theta)\rangle = 0.984$, demonstrating that without better control of the local field direction, finding the beam velocity from rephasing data is flawed at the 1% level.

By looking at the rate that the rephasing pattern washes out over, we can extract a velocity distribution width. This indicates a rms width of 5.6%, as compared to 3.6% from diffraction patterns. This discrepancy could be caused by magnetic field gradients being induced by increasing septum currents.

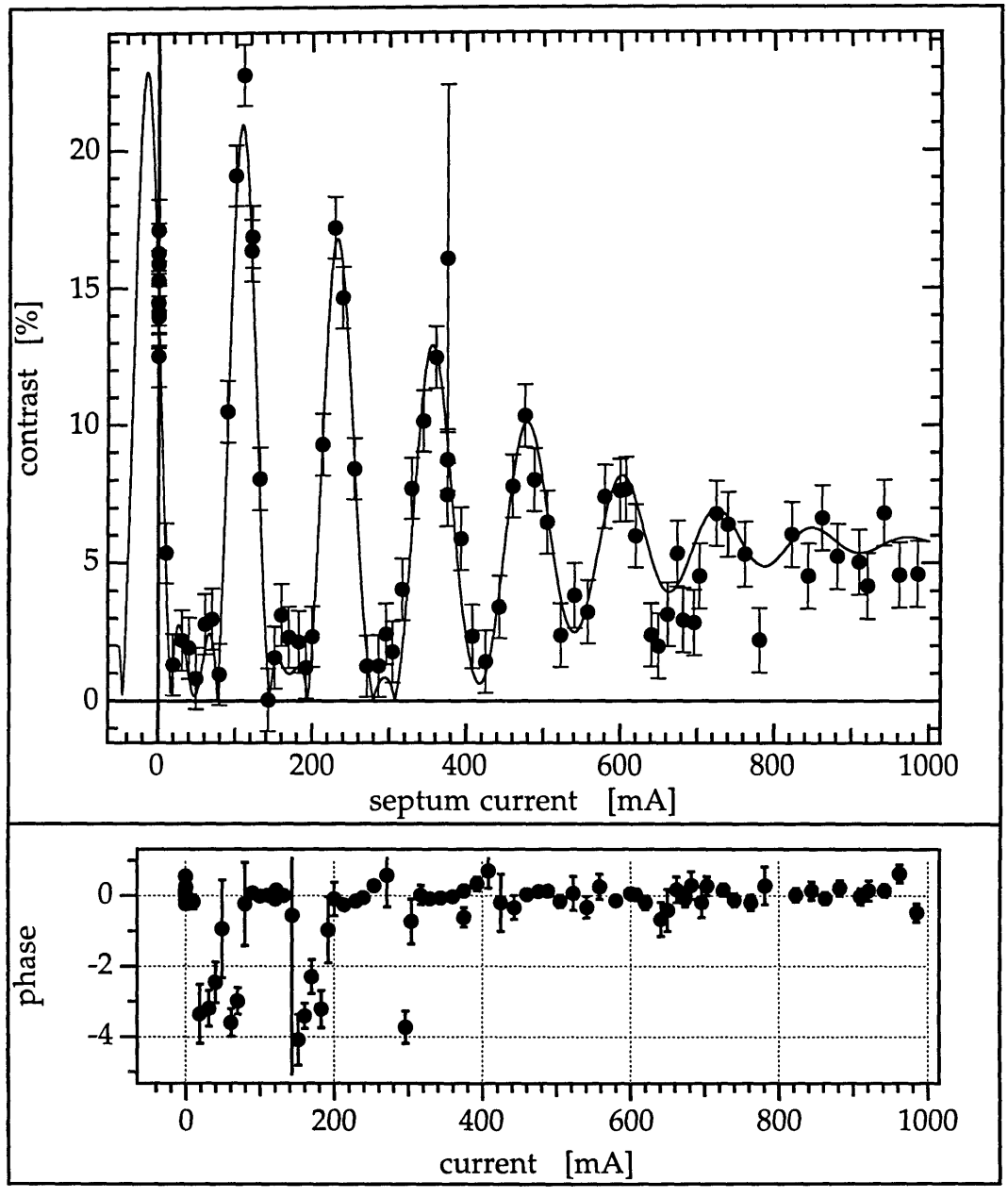

Figure 5.3: Magnetic rephasing data. The top graph is the contrast of the interference pattern as a function of the current flowing down the septum. The lower graph is the phase of the same interference patterns. Note the sudden changes in the phase by π.

The second set of data, shown in Figure 5.4, is not well accounted for by our theory. The peaks in the contrast function are not symmetric. The key to our

qualitative understanding of these data is how the current leads were hooked to the foil for this data. The current flowed down one end of the foil. We believe that the sudden change in field around the end of the foil caused non-adiabatic following of the spins. We could construct no simple model to describe this non-adiabatic behavior.

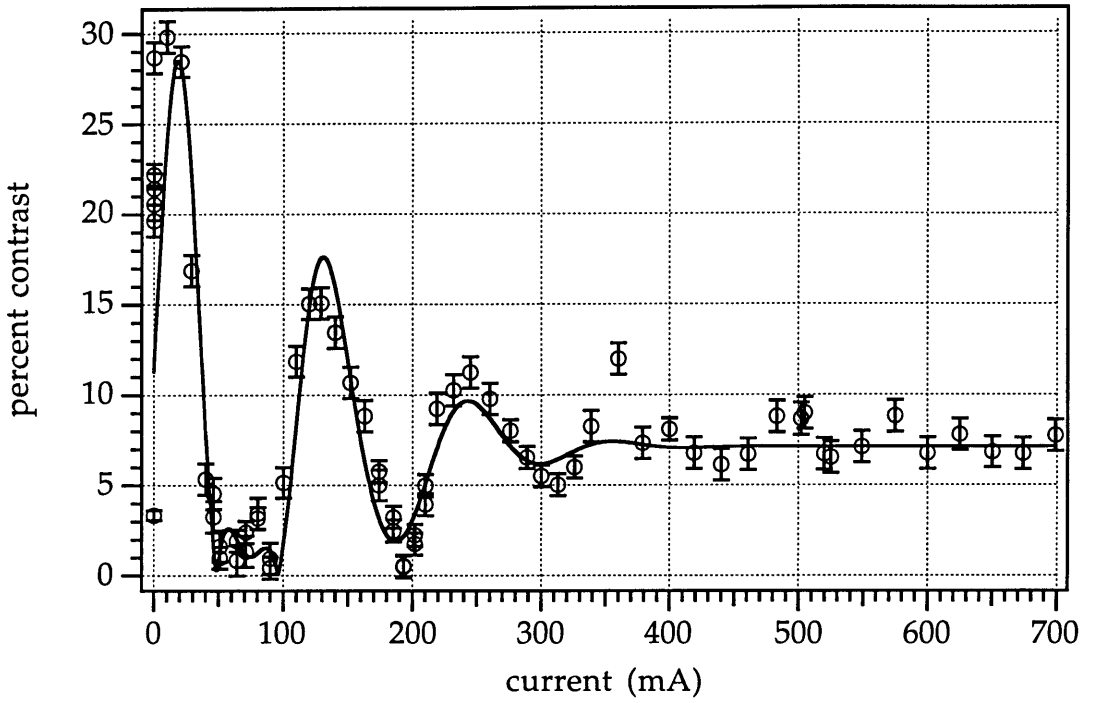

Figure 5.4: Contrast versus septum current for a configuration of magnetic fields that presumably produces non-adiabatic transitions between the Zeeman states. The solid line is a fit to the function derived in section 5.1, with poor agreement.

5.3 Balancing phase shifts with the Stark effect

As mentioned at the end of section 5.1, for large applied phase difference, only the states with no magnetic moment projection on the guide field contribute to the interference fringes. If we were to add a small additional interaction to one beam of the interferometer, we would see the effects in the interference pattern from only the $m_F=0$ atoms. This is an easy way to do interferometery on an aligned beam without the difficulty of optically pumping the beam. This would be a real advantage for an atom with no simple light source for an optical pumping transition. This is important because the gratings used in our interferometer are not specific to the structure of the atom.

We performed an experiment in which we independently addressed two of the different spin projections. This was accomplished by adding a Stark phase shift to the magnetic rephasing setup. The experiment was run with an electric field applied to one beam of the interferometer that corresponded to 70 radians of phase shift. This Stark phase shift was well outside the coherence length of the beam, and destroyed the contrast for all of the m_F states.

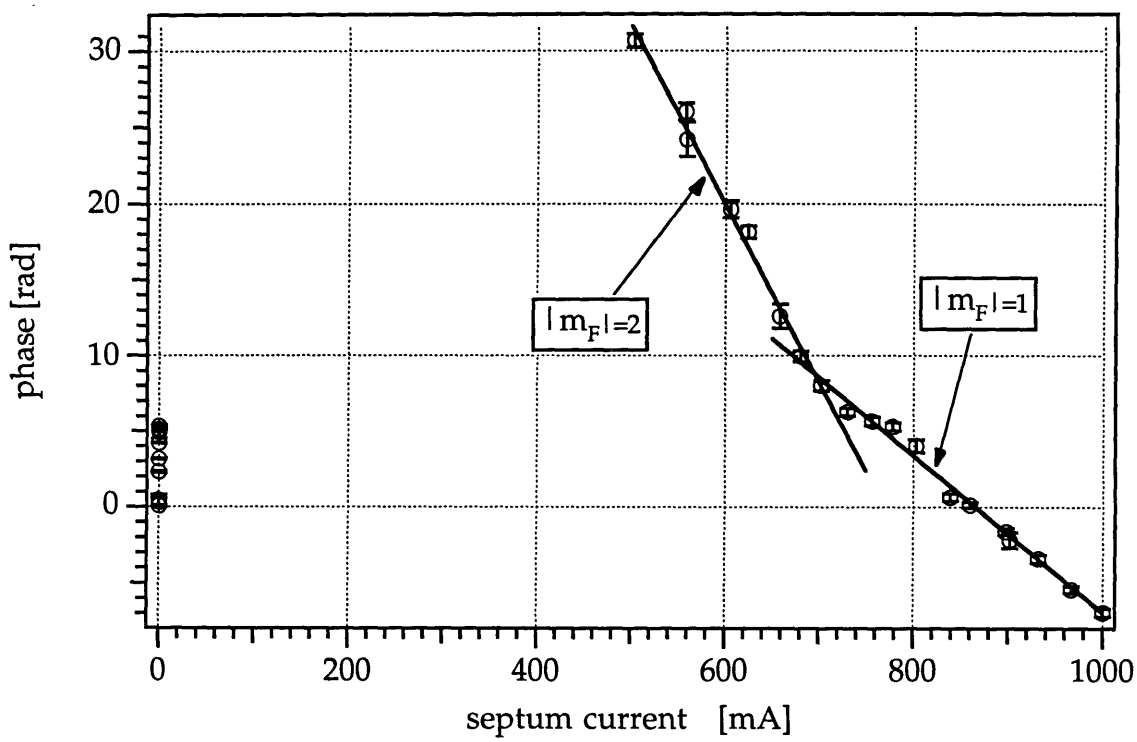

Figure 5.5: Phase shift versus septum current, and therefore differential Zeeman phase shift. There is an additional 70 radians of Stark phase shift applied between the beams of the interferometer. The two slopes of the phase correspond to different magnetic moment projections being within their coherence length.

The next step was to apply a differential Zeeman phase shift with the rephasing magnetic fields. For certain ranges of septum currents, and therefore differential Zeeman phase shifts, one magnetic moment projection would have a total (Zeeman plus Stark) phase shift that was within the coherence length of the beam. Figure 5.5 shows the phase shift of the resulting interference pattern as a function of septum current. The slope of the line reflects the magnitude of the magnetic moment projection.

While this is a nice way to address only one spin projection, optical pumping in our beam is possible and provides four times the intensity. This optical pumping is made easier because we have a room full of working spectroscopic dye lasers.

5.4 Applications

The question remains: what is this experiment good for? If the local field direction and the current distribution in the foil were well known, the only other parameter that determines when the rephasing "resonances" occur is the velocity. This would allow us an independent measure of the mean velocity and the velocity width of the beam. This would be even more important than a simple check of our velocity distribution because it would measure the velocity distribution that we really care about, the one that is present and contributing to interference when the interferometer is running. Issues of the change in velocity distribution due to interaction region position and detector position are dealt with in sections 4.2 and 4.5.

In its current form, this experiment does have several virtues. It is (at least to my tastes) simple and elegant. You have to believe several fundamental things about quantum mechanics to understand the results of this experiment. The first is that the phase shift of the particle depends on it's magnetic moment projection. The second is that the different spin projections form independent interferometers. This makes it an interesting pedagogical tool. The final, and not insignificant value, is that it provides a simple way to balance two phase shifts that have the same dispersion.

6 Index of refraction of a gas for matter waves

In light optics, it is common to characterize a material by its index of refraction and its transmission. The index of refraction occurs from the forward scattering of the light, as does the attenuation. The attenuation is related to the imaginary part of the forward scattering amplitude by the optical theorem. This means that these bulk properties are determined by the microscopic scattering events within the material.

These ideas can be extended to matter waves. The attenuation of a beam of particles is due to the scattering of the beam into other directions and is governed by the imaginary part of the forward scattering amplitude. The phase shift of the wave function is governed by the real part of the forward scattering amplitude. This chapter deals with a scattering experiment that we performed by inserting a gas target into one arm of the interferometer. This opens up to opportunity to probe different properties of atom-atom and atom-molecule collisions. Scattering experiments have been performed with the noble gasses (He, Ne, Ar, Kr, Xe) and several molecules (N_2, CO_2, H_2O, NH_3) as target gasses. The results for the ratio of the real to imaginary parts of the forward scattering amplitude are compared to several semiclassical scattering models.

6.1 Experimental setup

The gas target is created by making a small modification to the basic interaction region. The altered interaction region and beam paths are shown in Figure 6.1. One side plate has a hole drilled through it to allow the introduction of the target gas into one beam path. There are tabs to close down the ends of the volume on the side of the interaction region with the

gas to decrease the gas load into the main chamber of the vacuum system, creating a large differential pumping factor between the cell and the main chamber. The openings on either end of the gas cell are 200 microns wide.

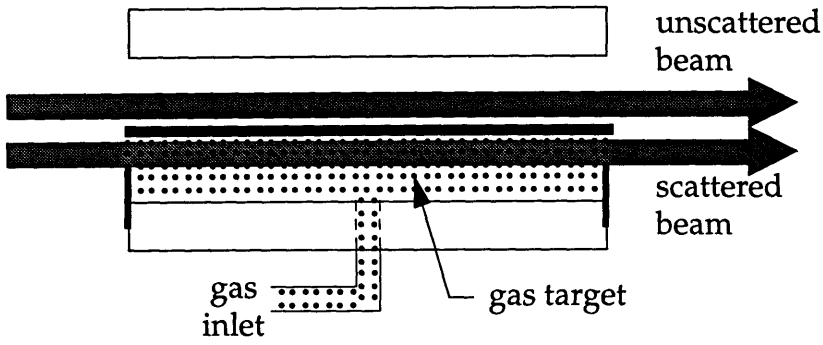

Figure 6.1: The gas target interaction region showing the scattered and unscattered beams.

The question now is: What is the effect on the beam that goes through the gas target? I will consider a beam that is transported through a gas sample of length L and density n. If the wave function has a well defined wave vector k, the wave function will be altered as follows.

$$\Psi(L) = \Psi(0) e^{ikL} e^{-\frac{2\pi}{k} nL \mathrm{Im}(f(k,\theta=0))} e^{i\frac{2\pi}{k} nL \mathrm{Re}(f(k,\theta=0))}$$

The first term, $\Psi(0)$, is the envelope of the incident wave function of the beam. The second term is the standard phase factor for propagation of a plane wave with wave vector k. The third term is a reduction of the amplitude of the wave function that represents scattering out of the beam. This attenuation of the amplitude is just the square root of the attenuation we expect from the total cross section from the optical theorem. The transmission T of intensity through the gas sample is

$$\begin{aligned} T &= e^{-\frac{4\pi}{k} nL \mathrm{Im}(f(k,\theta=0))} \\ &= e^{-\sigma_{total} nL}. \end{aligned}$$

We will be able to study this attenuation in two ways, by looking at the amplitude of the transmitted beam, which decreases like T, or by looking at the decrease in the interference amplitude, which decreases like $\sqrt{T}$ (since only one beam is attenuated by the gas).

The last term is the phase shift from forward scattering. It is obvious that if we were to analyze this experiment by simply counting particles after the

beam exits the gas target, we would never see effects from this term. In our experiment, however, we interfere the altered wave function with an unaltered copy of itself, preserving the phase information. The phase shift appears as the phase shift of the interference pattern.

I am justified in considering only the forward scattering because the differential scattering amplitude has no features as small as the total angular size of the experiment. The size of the scattering potentials that are use in this experiment are ~15 Angstroms. This gives a diffraction angle of 11 milliradians for our sodium beam with a wavelength of .165 Angstroms. The target is 80 cm from the detector, so the diffractive spot size is 9 mm at the detector plane. This is the minimum size for structure in the scattering amplitude, and the total angular width of the beam at the detector plane is less than 0.1 mm, so I am justified in considering only forward scattering.

6.2 Calculating f(k,0)

To compare the results of the experiment to theory, we need to be able to calculate the forward scattering amplitude. The quantity that we are most sensitive to in the experiment is the ratio of the real to imaginary parts of the forward scattering amplitude. We have used several models to see if we can gain any qualitative information about the different scattering results.

Hard sphere scattering

The problem of scattering from a hard sphere is soluble in closed form. The partial wave phase shifts are given in most quantum mechanics texts [SAK85]

$$\tan(\delta_l) = \frac{j_l(kR)}{n_l(kR)}.$$

The radius of the hard sphere is R and the wave vector of the incident particle is k. The scattering amplitude in the forward direction is found by completing the following sum over angular momentum quantum number,

$$f(k,\theta) = \frac{1}{2k}\sum_l (2l+1)\left[e^{2i\delta_l(k)} - 1\right]P_l(\cos(\theta)),$$

which reduces to the following in the forward direction.

$$f(k,\theta=0) = \frac{1}{k}\sum_l (2l+1)e^{i\delta_l(k)}\sin\delta_l(k)$$

This model gives a very small ratio of real to imaginary part, on the order of one over the number of partial waves contributing to the scattering process.

Semiclassical scattering models

For all of the scattering experiments, a large number of partial waves contribute to the scattering process. The maximum angular momentum that contributes to the scattering process is on the order of the momentum of the sodium atoms multiplied by the maximum impact parameter of interest in the scattering potential. This product is equated to the maximum angular momentum quantum number multiplied by $\hbar$, yielding a maximum angular momentum quantum number that is the range of the potential divided by the reduced wavelength of the sodium atom. This is 500-600 for the systems we have studied.

The large number of partial waves contributing to the scattering process suggests a semiclassical approach coupled with the eikonal approximation introduced in section 3.1. I will summarize the results of semiclassical scattering theory [SAK85] when we look only in the forward direction.

The phase shift for a trajectory that approaches the scattering center with an impact parameter b is

$$\Delta(b) = -\frac{m}{2k\hbar^2}\int_{-\infty}^{\infty} V\left(\sqrt{b^2+z^2}\right)dz,$$

where $V(r)$ is the radial scattering potential. This phase shift at a given impact parameter takes the place of the partial wave phase shift at a given angular momentum. We then transform the sum over angular momentum quantum number in the standard expression for the scattering amplitude

$$f(k,\theta) = \frac{1}{2k}\sum_l (2l+1)\left[e^{2i\delta_l(k)}-1\right]P_l(\cos(\theta))$$

into an integral over impact parameter. If we drop the angular dependence, as $P_l(1)=1$, we arrive at

$$f(k,\theta=0) = -ik\int_0^{\infty} bdb\left[e^{2i\Delta(b)}-1\right],$$

or, applying a simple trigonometric identity,

$$\mathrm{Re}\left[f(k,\theta=0)\right]=k\int_0^\infty bdb\sin(2\Delta(b))$$

$$\mathrm{Im}\left[f(k,\theta=0)\right]=2k\int_0^\infty bdb\sin^2(\Delta(b)).$$

The actual quantity that we will be investigating is the ratio of the real to imaginary parts of the forward scattering amplitude. Calculation of this ratio will be much simpler than calculating each part in some cases, and will be relatively independent of the magnitude (but not the shape) of the potential.

Pure long range attraction

The lowest order attractive potential between two neutral, polarizable atoms is

$$V(r)=-\frac{C_6}{r^6}.$$

For this potential, there are fairly general things that can be said about the ratio of the real to imaginary parts of the forward scattering amplitude. That ratio is in fact independent of C_6 if one uses an eikonal approximation for the phase shift, and a semiclassical approximation for calculating the scattering amplitude.

The phase shift for this potential is proportional to the integral of the potential along a line through the potential. If we operate at a fixed impact parameter b:

$$\begin{aligned}\Delta(b) &\propto \int_{-\infty}^{\infty} V\left(\sqrt{z^2+b^2}\right)dz\\ &\propto \int_{-\infty}^{\infty}\left(z^2+b^2\right)^{-3}dz\\ &\propto b^{-5}\\ &=\frac{C}{b^5}\end{aligned}$$

Here, C is not the attractive coefficient, but is a constant that depends upon the attractive coefficient and the center of mass wave vector like

$$C=\frac{3m\pi}{16k\hbar^2}C_6.$$

The real and imaginary parts of the forward scattering amplitude have the following dependence on b and the phase shift in the semiclassical approximation.

$$\mathrm{Re}(f) \propto \int_0^\infty b db \sin(2\Delta(b))$$

$$\mathrm{Im}(f) \propto \int_0^\infty 2 b db \sin^2(\Delta(b))$$

The key is to make a substitution for b and do the integral over the phases.

$$b = \left(\frac{C}{\Delta}\right)^{\frac{1}{5}}$$

$$db = -\frac{1}{5}\left(\frac{C}{\Delta^6}\right)^{\frac{1}{5}} d\Delta$$

With these substitutions, and changing the order of the integration limits we arrive at:

$$\mathrm{Re}(f) \propto \frac{C^{\frac{2}{5}}}{5}\int_0^\infty \Delta^{-\frac{7}{5}} \sin(2\Delta) d\Delta$$

$$\mathrm{Im}(f) \propto \frac{C^{\frac{2}{5}}}{5}\int_0^\infty \Delta^{-\frac{7}{5}} \sin^2(\Delta) d\Delta$$

We can see that any dependence on C in the scattering amplitudes and the phases cancel when we look at the ratio of real to imaginary parts. The two integrals can be done analytically and the result is:

$$\frac{\mathrm{Re}(f)}{\mathrm{Im}(f)} = -\frac{\Gamma\left(\frac{3}{10}\right)\Gamma\left(\frac{7}{10}\right)}{\Gamma\left(\frac{6}{5}\right)\Gamma\left(-\frac{1}{5}\right)}$$

$$= .7265$$

This procedure can be easily extended to any potential that varies like r^{-n} (n is a positive integer), and gives a result:

$$\frac{\mathrm{Re}(f)}{\mathrm{Im}(f)} = -(n-1)\frac{\Gamma\left(\frac{1}{2}-\frac{1}{n-1}\right)\Gamma\left(\frac{1}{2}+\frac{1}{n-1}\right)}{\Gamma\left(-\frac{1}{n-1}\right)\Gamma\left(\frac{1}{n-1}\right)}$$

Molecular potentials

Molecular potentials have been determined for some of the systems we have studied experimentally. These potentials can be used along with the semiclassical scattering methods to predict the ratio of the real and imaginary part and the magnitude of each. We have 6-12 potentials for sodium interacting with argon, krypton, xenon [DRS68], and neon [DFS72]. We also have a 6-8 potential for sodium interacting with neon [GAL81]. These potentials are shown in Figure 6.2.

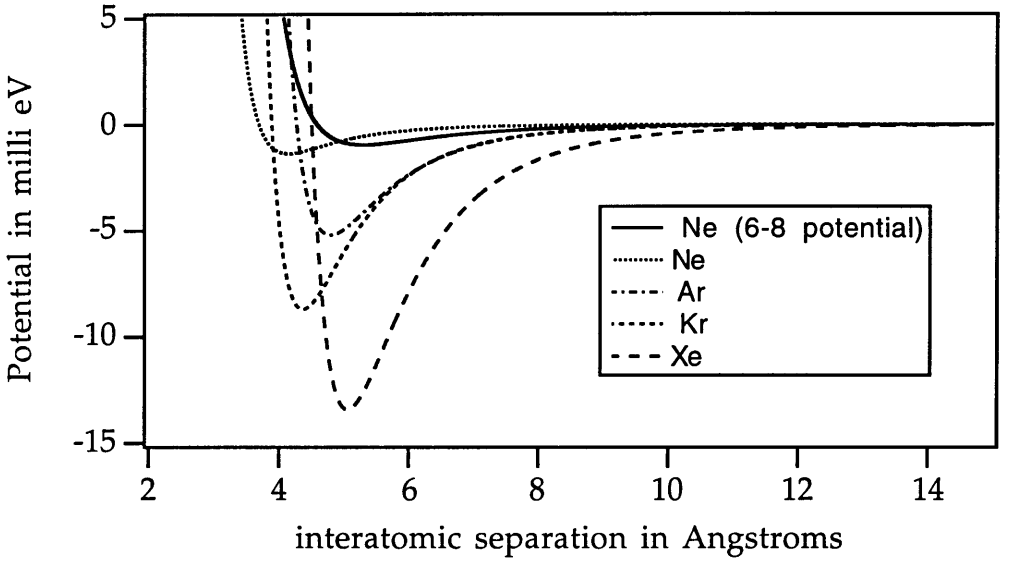

Figure 6.2: Interatomic potentials for sodium-noble gas molecules.

We can integrate the straight line trajectories through these potentials to find the semiclassical phase shift as a function of impact parameter. The resulting phase shifts are shown in Figure 6.3. It is clear from the form of the potential that the phase shift gets very large for small impact parameter, and will be increasing in magnitude like at least b^{-7} for small b.

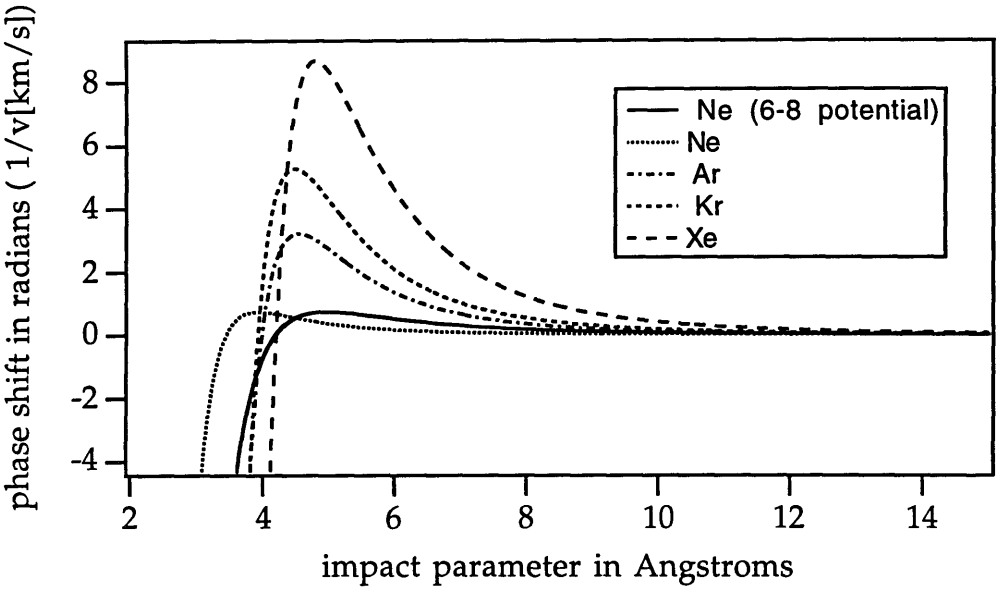

Figure 6.3: Semiclassical phase shift as a function of classical impact parameter. The phase shifts shown are calculated for a 1000 m/s center of mass collision velocity, using the potentials shown in Figure 6.2.

To find the forward scattering amplitude, we must integrate the weighted trigonometric functions of these phase shifts over all impact parameters. The integrands of the real and imaginary parts of the scattering amplitude are shown in Figure 6.4 for the case of an argon target. The rapidly changing phase shift at small impact parameter causes rapid oscillations in the integrand. These rapid oscillations will prevent a simple numerical integration.

For the imaginary part of the forward scattering amplitude, the oscillations of the integrand are due to the square of the sine of the phase, so they will average to a positive value (see figure 6.4). For small impact parameters, we can replace the square of the sine with its average value of 1/2. We then break the integral up by integrating over two ranges. The first is out from zero to an impact parameter where the phase is still falling rapidly, but from where a numerical integration becomes possible for the correct expression of the integrand. In this first range of impact parameters, we replace $\sin^2$ with 1/2, yielding an integral that is solved analytically. From the end of the first range out to infinity, the full integrand is integrated numerically. This is similar to the Schiff-Landau-Lifshitz approximation.

For the real part, the rapid oscillations of the integrand are symmetric about zero. This allows the first integration range discussed in the evaluation of the imaginary integral to be set to zero. The outer range is integrated numerically.

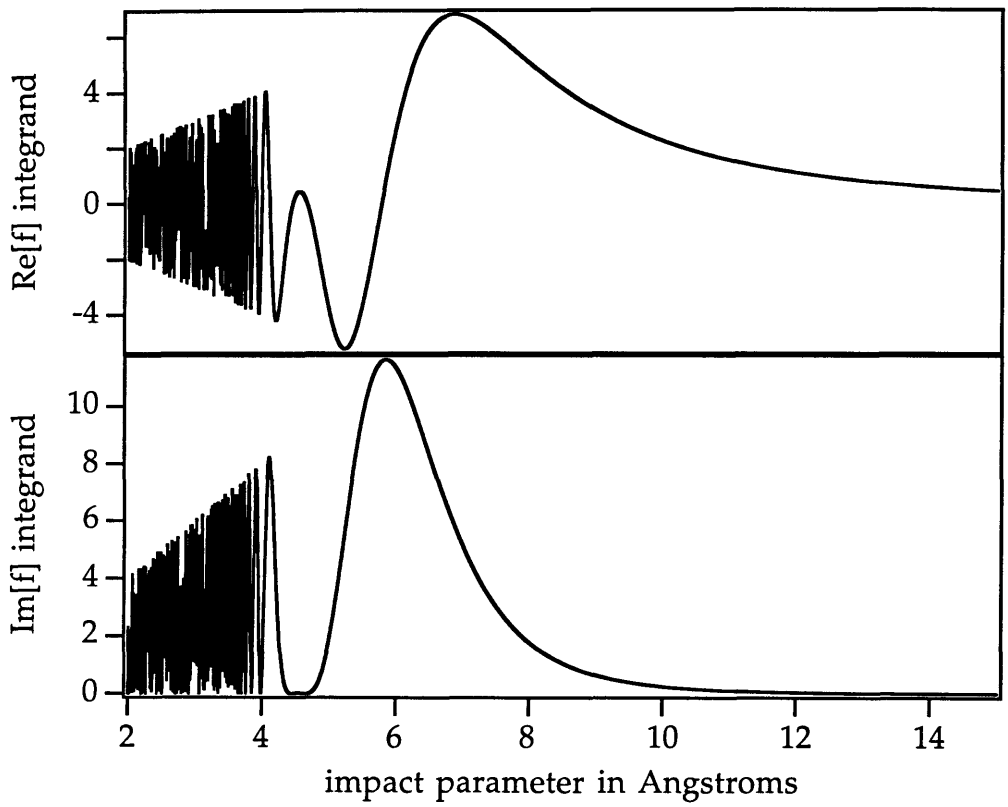

Figure 6.4: Behavior of the integrands for the real and imaginary parts of the scattering amplitude. The rapidly oscillating behavior at small impact parameter averages to zero for the real integrand and to a positive value for the imaginary integrand. The parameters are for the sodium-argon system colliding at 1 km/sec.

Velocity average of the transmission and phase shift

The atomic beam used in the interferometer has a velocity width of 10% FWHM. This, along with the thermal velocity distribution of the target gas provide a center of mass velocity distribution that we must average over. There is an interesting feature in the realized phase shift and attenuation of the interference due to this average. The measured transmission of the sodium beam must be averaged over this distribution which we choose to perform in k space. Given that the probability distribution in k space is $P(k)$, the measured transmission is

$$T_{measured} = \int P(k)T(k)dk$$
$$= \int P(k)e^{-\frac{4\pi}{k}n\,\mathrm{Im}(f(k,0))}dk$$

When we look at the effect of the average on the phase, things are a little more complicated. The attenuation will depend on the wave vector of the atom, so for reasonably large attenuations, there will be a different surviving velocity distribution. This should produce behavior that will not follow a simple linearly increasing phase shift and optical density with column density of the target.

To compute the phase shift we must average the k-vector dependent phase shift over P(k).

$$\varphi(k) = \frac{2\pi}{k}n\,\mathrm{Re}(f(k,0))$$

$$\varphi_{measured} = \arctan\left[\frac{\int P(k)\sqrt{T(k)}\sin\varphi(k)dk}{\int P(k)\sqrt{T(k)}\cos\varphi(k)dk}\right]$$

The decrease in interfering amplitude is governed by a more complex function than the standard expression for the first order coherence function mentioned in section 3.4.

$$A_{Int} = \sqrt{\left(\int P(k)\sqrt{T(k)}\sin\varphi(k)dk\right)^2 + \left(\int P(k)\sqrt{T(k)}\cos\varphi(k)dk\right)^2}$$

It should be noted that the basic formula for the average phase shift in the interferometer worked perfectly well at the level of precision in this experiment. The additional transmission factor may lead to additional information about the energy dependence of the collision process in experiments with enough extra intensity to measure the phase shift at larger attenuations.

6.3 Attenuation

The attenuation of the beam can be measured in two ways. The first and most obvious way is to record the reduction in intensity of a beam that is transmitted through the gas target. We performed this experiment by sending the first and minus first order diffracted beams of a single grating diffraction pattern through the two sides of the interaction region (the zeroth order beam was aligned to run into the end of the mylar foil). By measuring

the reduction of one beam relative to the other, we can determine the attenuation per amount of column density in the sample. The differential pumping ratio of the gas cell is reflected in the relative reduction of the attenuated and nominally unattenuated beams. The reduction of the nominally unattenuated beam represents a gas target that is the entire main chamber at a lower pressure than the gas cell.

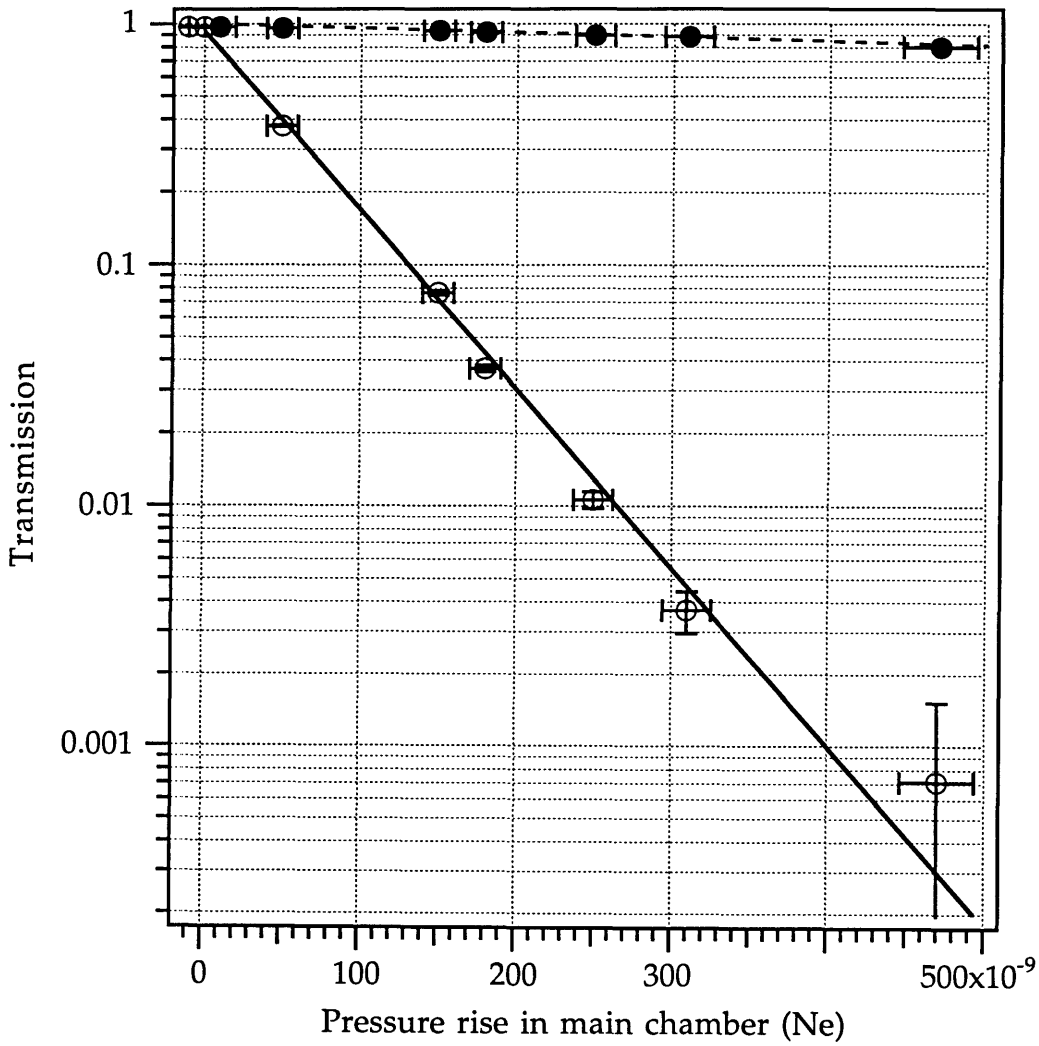

Figure 6.5: Transmission of the attenuated (open circles) and nominally unattenuated (closed circles) beams. The lower axis in the pressure rise in the main chamber, and is proportional to the column density of the target. The ratio of the exponential fits implies a differential pumping ratio of 600.

One problem arises when we want to know the absolute number of atoms in the gas target. We monitor the rise in the main chamber's pressure on a Bayard-Alpert type ionization gauge. The rise in main chamber pressure is

proportional to the column density of the target. Any absolute measurement depends on the accuracy of the ionization gauge, corrections for the response of the gauge to the particular target gas, and the differential pumping ratio of the target. We trust the ionization gauge to about 25% of its reading. The only reference we have for the corrections for gas type have scatter in the values for a given gas of 5% to 40%. This makes any absolute measurement of the size of the imaginary part of the cross section difficult without much more care applied to the measurement of the column density of the target.

Another way to measure the attenuation is to monitor the interference amplitude of the interferometer as a function of pressure rise in the main chamber. This measurement has less good statistics that the previous measurement because there are three amplitude gratings in the beam instead of one (so the signal is reduced), but you win a lot of that back because you are only attenuating the amplitude of the scattered wave function, so the loss of interfering amplitude goes down by a factor that is the square root of the intensity transmission factor. The problems of pressure measurement still remain, but this wound up being the best way to measure the ratio of the real and imaginary parts of the scattering amplitude.

6.4 Phase shifts

As outlined in section 6.1, the phase shift of the interferometer is proportional to the column density of the gas target multiplied by the real part of the scattering amplitude. The same problems with target density measurements remain, and the relative sizes of the different real parts for different gas targets suffer from not knowing the gauge calibrations. The phase shift of the interferometer as a function of main chamber pressure rise is shown in Figure 6.6.

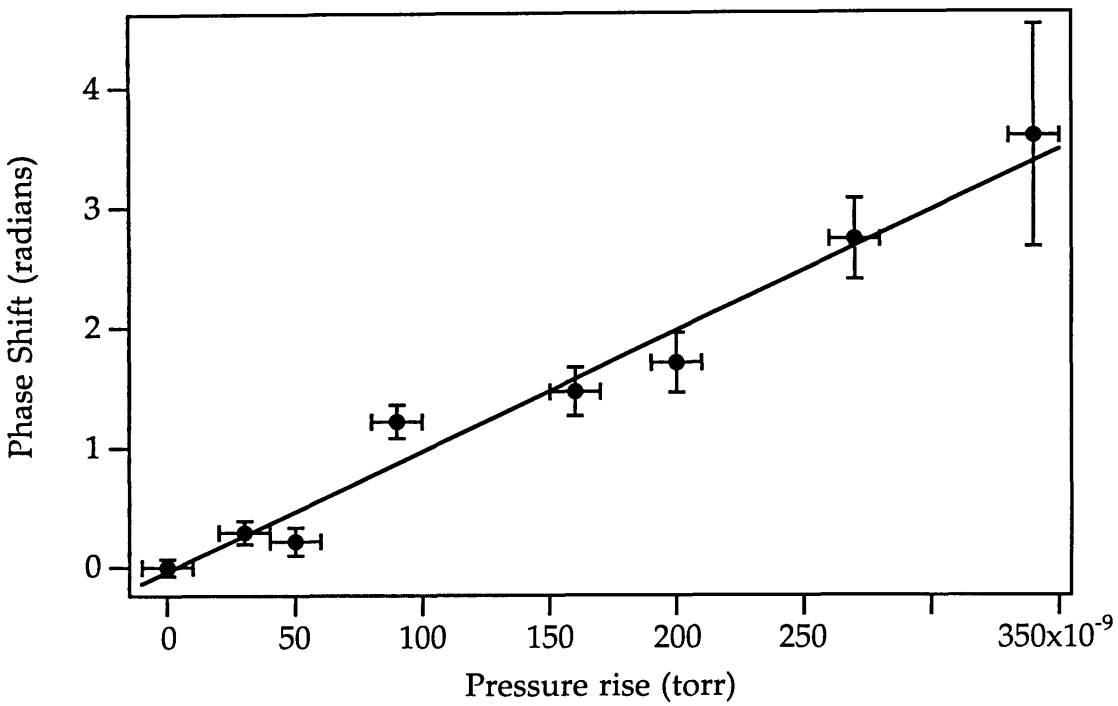

Figure 6.6: Phase shift versus pressure rise in the main chamber. The horizontal axis is the pressure rise in the main chamber, and is proportional to the column density of the gas target. The linear fit minimizes the chi-squared for both dimensions.

To determine the phase shift for a given pressure rise, the interference pattern is recorded for a given pressure rise in the main chamber. The phase shift is measured with respect to the mean of the phases of interference patterns taken before and after with no gas in the target cell. The time constant for evacuating the gas from the target after a measurement has been made is a few seconds, allowing fast changes between gas and no gas in the target cell.

6.5 Ratio of the real to imaginary part of f(k,0)

From the measurements described above, we can experimentally determine the ratio of the real to imaginary parts of the scattering amplitude.

Ratio of attenuation to phase shift

The first method uses a combination of the intensity attenuation measurement and the phase shift experiment. We combine the results of our fits of transmission versus column density and of phase shift versus column density. The column density measurements are not calibrated, but we

assume that they are repeatable. These two quantities are combined as follows:

$$\frac{\Delta\varphi/n}{\frac{1}{2}\ln[T(n)]/n} = \frac{\frac{2\pi}{k}\mathrm{Re}[f(k,\theta=0)]}{\frac{1}{2}\frac{4\pi}{k}\mathrm{Im}[f(k,\theta=0)]} = \frac{\mathrm{Re}[f(k,\theta=0)]}{\mathrm{Im}[f(k,\theta=0)]}$$

On the first line, the numerator is the slope of the line fitting the phase shift as a function of pressure rise, from Figure 6.6. The denominator is one half of the decay constant from the fit shown in Figure 6.5.

Ratio of interfering amplitude to phase shift

There is another way to determine the ratio of real to imaginary parts of the scattering amplitude that does not rely on the repeatability of the ion gauge. This involves fitting the natural log of the interfering amplitude as a function of phase shift. Each quantity is determined from the same interference scan, and therefore at the same time with the same gas target parameters. This method also takes advantage of attenuating only the amplitude in one beam, so that the interference amplitude decreases like the square root of the intensity transmission. The decay constant from a fit to this data is exactly the ratio we are interested in. Figure 6.7 shows the fitting procedure for this method when applied to neon and helium.

A fitting procedure that minimizes the total chi-squared for error bars in both dimensions was used. The algorithm was supplied by a standard numerical simulation library [PTV92].

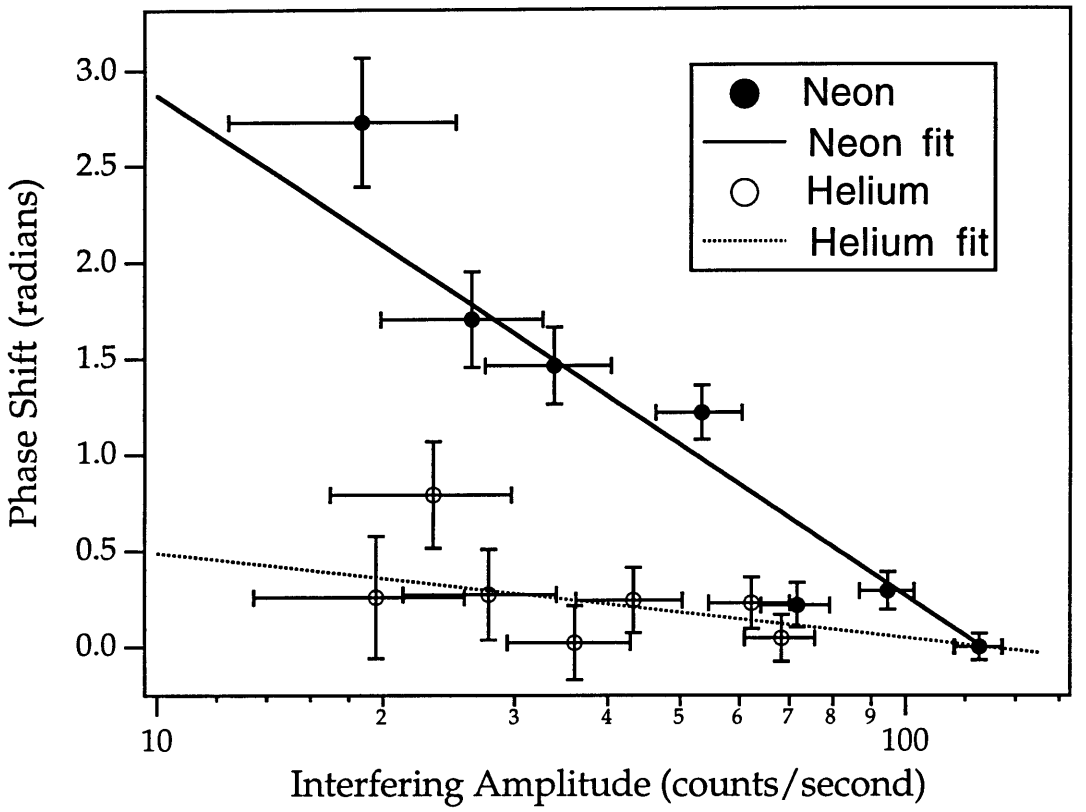

Figure 6.7: Phase shift versus the amplitude of the interference fringes for helium and neon. The slope of the fit on a semi-log plot as shown here is minus the ratio of the real to imaginary parts of the forward scattering amplitude.

It is interesting to make a rough comparison of the relative real and imaginary parts of the forward scattering amplitude between helium and neon target gasses. This comparison is limited by uncertainties in the ionization gauge corrections and gauge accuracy to approximately 30% relative errors. The imaginary parts of the forward scattering amplitude, and therefore the total cross section, are the same. The real parts of the forward scattering amplitudes, however, are different by a factor of ten. This difference in the real parts would never have been seen by counting particles in the forward direction. In this case, they look the same in an attenuation experiment.

The results of the various scattering models and our best experimental determination of the ratio of the real to the imaginary parts of the scattering amplitude are shown in Table 6.1. By comparing these results with theory, we can say several qualitative things about the scattering we have observed. The interaction with helium looks most like a hard sphere (the ratio being

very close to zero). The large ratio of real to imaginary part for neon can be explained by the fact that the positive phase shift is never larger than one radian, allowing a large accumulation of the real part in the semiclassical integral. The remaining three gasses have phase shifts that vary more quickly with impact parameter, and reach much larger positive values. This produces ratios that are much more like the pure long range interaction, which has a phase shift that varies like $b^{-(n-1)}$, accumulating large amounts of phase shift at small impact parameter.

All of the molecular target gasses have ratios that are considerably lower than that predicted for a pure long range attractive potential from dipole-dipole interactions. The prediction for r^{-8} (dipole-quadrapole) attraction gives a lower ratio of 0.48 from the r^{-n} results of section 6.2. We are currently attempting to model these results, but are hampered by a lack of atom-molecule potentials.

	He	Ne	Ar	Kr	Xe
$\frac{\Delta\varphi/n}{\frac{1}{2}\ln[T(n)]/n}$	0.08(4)	1.13(10)	0.75(10)	0.81(7)	0.72(7)
$\frac{\Delta\varphi}{\ln[A_l]}$	0.19(7)	1.13(11)	0.78(9)	0.97(10)	0.64(11)
C_6 only	0.72	0.72	0.72	0.72	0.72
6-12 potential		1.12	0.71	0.68	0.69
6-8 potential		1.33			

Table 6.1a: Table of the ratio of real to imaginary parts of the forward scattering amplitude for sodium-noble gasses. The results are from the experiments and the theoretical models discussed in this chapter.

	H_20	NH_3	CO_2	N_2
$\frac{\Delta\varphi}{\ln[A_l]}$	0.66(7)	0.62(5)	0.65(6)	0.57(4)
C_6 only	0.72	0.72	0.72	0.72

Table 6.1b: Table of the ratio of real to imaginary parts of the forward scattering amplitude for sodium-molecules. The results are from the experiments and the theoretical models discussed in this chapter.

7 The Talbot effect

This chapter will cover the first demonstration of the Talbot effect with matter waves. In contrast to previous experiments with diffractive atom optics elements, which were all demonstrated in the far field, this is a near field interference effect. This deals with near field images produced by amplitude diffraction grating.

7.1 Theory

The self imaging of periodic structures in the near field was discovered by Talbot [TAL36] and von Laue [LAU48], and first explained by Rayleigh [RAY81]. The basic effect is that an amplitude diffraction grating illuminated by a monochromatic plane wave source produces high quality images of itself at a series of locations downstream in the near field. These locations are integer multiples of a distance called the Talbot length, given by p^2/λ, where p is the grating period and λ is the wavelength of the plane wave. The phase of the image flips by 180 degrees at each successive image. There are also images with other periods at different distances downstream which have been recently explained by Clauser [CLR92].

I will now give a plausibility argument for why the length has the value that it does. The argument will refer to the geometry in Figure 7.1. If there is a plane after the grating that has an image that has amplitude oscillations with the same period p as the grating, you would expect the length difference of the paths from the two radiators distance p apart to change by λ when you move a distance p at the image plane. This means that the path length difference must be half of the wavelength. By looking at the geometry in Figure 7.1 we can see that

$$\left(L+\frac{\lambda}{2}\right)^2 = L^2 + p^2$$

By assuming that the wavelength is much smaller than the grating period, and therefore also L (a small angle approximation), we can expand the square and arrive at

$$L_{Talbot} = \frac{p^2}{\lambda}.$$

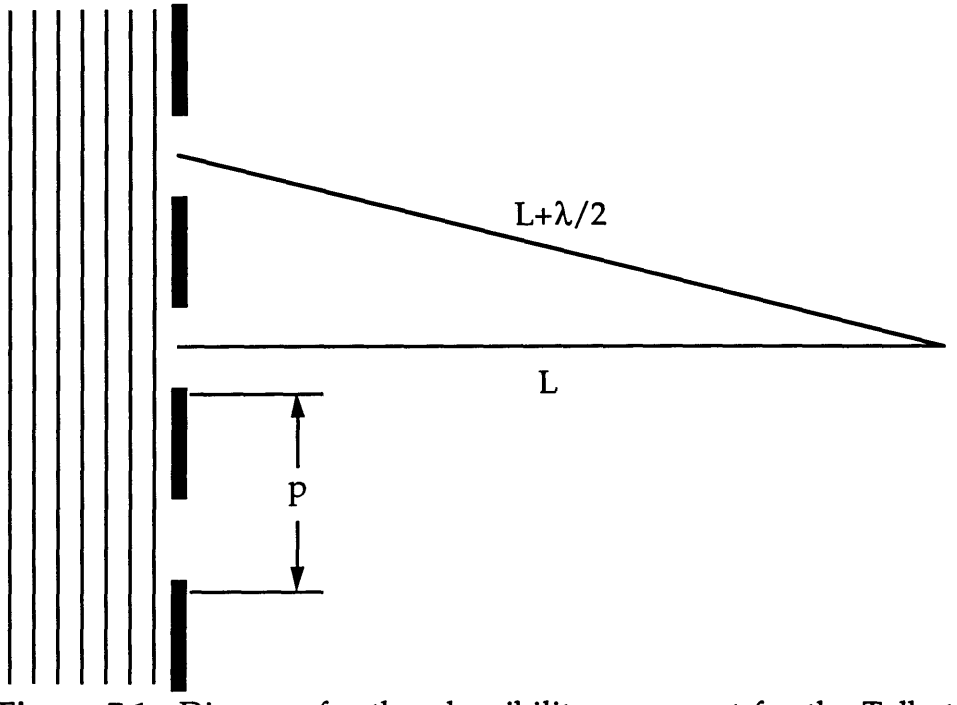

Figure 7.1: Diagram for the plausibility argument for the Talbot length. A plane wave with wavelength λ arrives from the left.

In the experiment, we masked the image of the grating with another amplitude grating and translated the masking grating to produce a fringe pattern. This near field detection is the same as the basic near field detection process in the interferometer (sections 1.1 and 3.3). There will be high contrast fringes only at multiples of the Talbot length. By varying the separation of the imaging grating and the detection grating, we can analyze the contrast of the Talbot image at various separations.

We have modeled this situation using a coherent ray tracing algorithm that was developed to model the interferometer [TUR92,TKP93]. This algorithm performs a coherent sum of the amplitudes for each path through a succession of planes located at various distances down the model beam line.

The model was run with an extended source, and propagated through, in turn: the collimators, the imaging grating, and the detection grating a variable distance downstream. The transverse position of the detection grating was moved across the beam line, and the total flux as a function of position was recorded. The contrast of these fringes is shown in Figure 7.4. These results show high contrast images for multiples of the Talbot length, as expected.

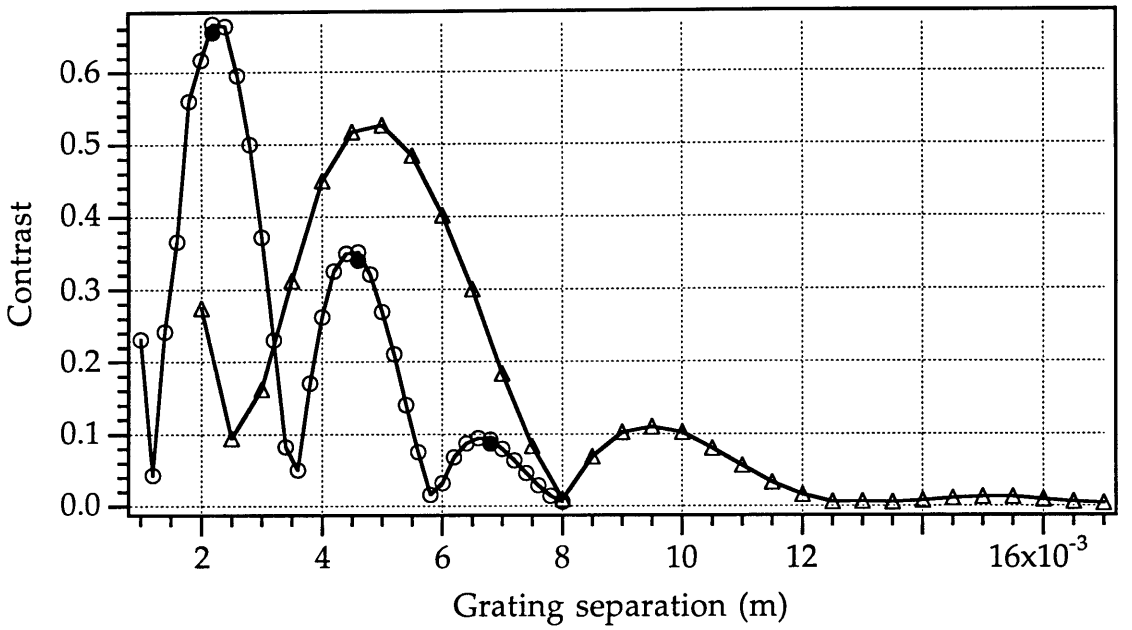

Figure 7.2: Calculated contrast of the transmitted intensity as a function of the separation between the gratings. Open markers are calculated with a monochromatic source for 200 nm (circles) and 300 nm (triangles) period gratings. The filled points were calculated with a polychromatic source.

7.2 Experimental setup

We realized this experiment by replacing the interaction region in the interferometer with an assembly that holds another grating just upstream from the second interferometer diffraction grating (Figure 7.3). This holder allows the distance that the new grating is upstream of the second grating to be varied. The transverse position of the second grating can be moved with a piezo-electric transducer (PZT) (this PZT is the same one that is used in the position servo for the interferometer).

The total transmitted intensity is recorded on the detector. This intensity will display a fringe pattern with respect to displacement of the second grating if there is a Talbot image present.

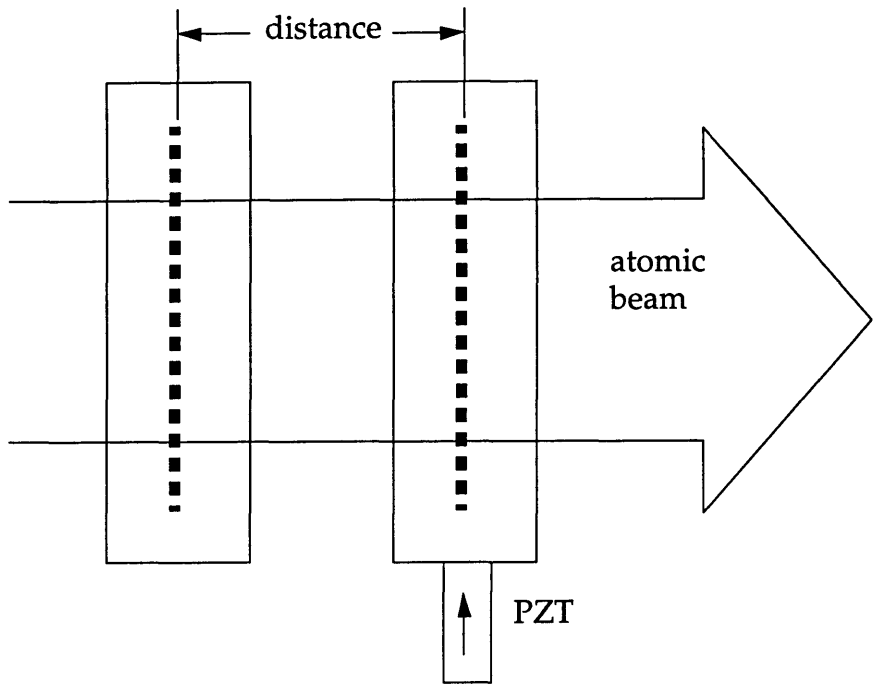

Figure 7.3: The experimental setup for the Talbot experiment. The distance between the gratings can be varied, and the total transmission of the atomic beam with respect to the piezo-electric transducer (PZT) position is recorded.

7.3 Experimental results

We used gratings of the same period for the first and second gratings. In this case we expect to see high contrast fringes when we translate the PZT at integer multiples of the Talbot length. We then expect the transmitted intensity as a function of PZT position to show high contrast fringes when the gratings are separated by integer multiples of the Talbot length.

The number of transmitted atoms as a function of the PZT position is shown in Figure 7.4. This represents the first demonstration of the Talbot effect with atoms.

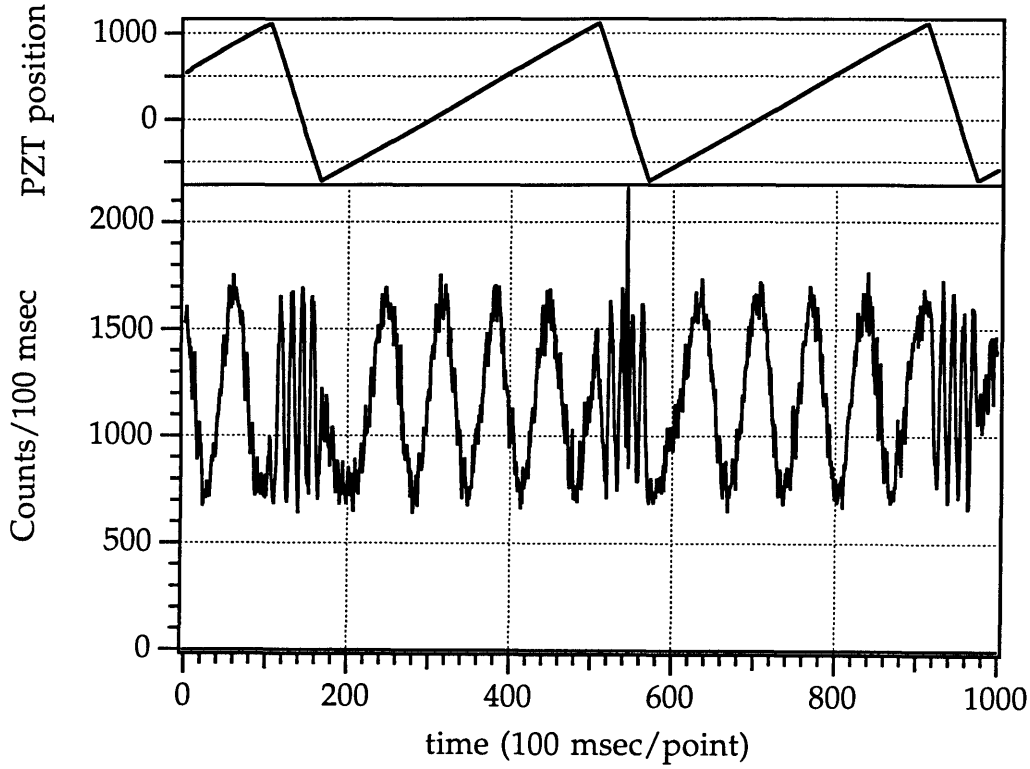

Figure 7.4: Demonstration of the Talbot effect with atoms. The transmitted atomic beam is correlated with relative PZT position. This data was taken with 200 nm period gratings at approximately two Talbot lengths.

We have performed this experiment with 200 nm and 300 nm period gratings. These two periods yield Talbot lengths of 2.4 mm and 5.5 mm respectively. The distance between the gratings was varied, and the contrast of the fringe pattern recorded at each location. We were able to vary the separation of the gratings from 3.5 mm to 11 mm. The minimum separation was imposed by the grating mounting system we use. The experimental results are shown in Figure 7.5.

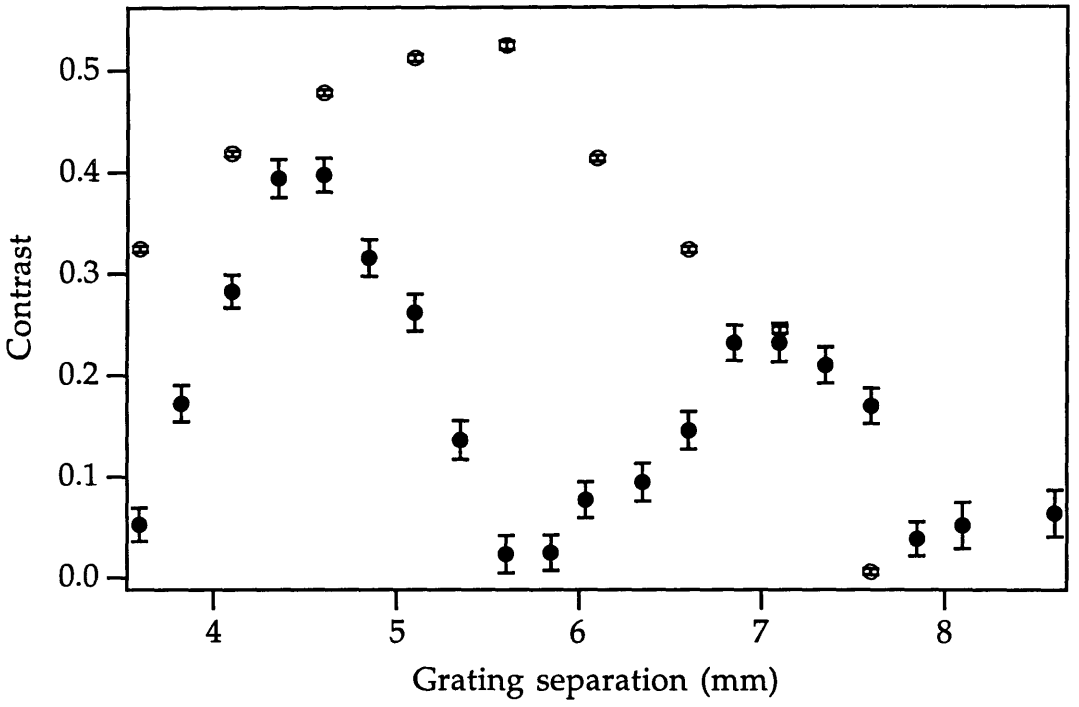

Figure 7.5: Experimental contrast as a function of grating separation for 200 nm (filled circles) and 300 nm (open circles) period gratings.

8 Molecular diffraction

This chapter will cover our first results with molecular optics. The first section will describe the production of an intense molecular beam of Na_2. The second section will cover the diffraction of these sodium dimers. The chapter will end with short discussions of the relative dimer fraction and speed in the beam, and the response of our detector to the molecules.

8.1 Molecular beam production

We produced an intense molecular beam of sodium dimers using the source described earlier in this thesis. We used high carrier gas pressures, high reservoir temperatures (750 Celsius), and nozzle temperatures that were close to the temperature of the reservoir to enhance the population of sodium dimers in the beam. The atoms were removed from the beam with resonant light forces. The maximum fraction of dimers was realized with no temperature gradient across the source.

The problem remains of removing all of the sodium atoms from the beam, to leave only the sodium dimers. This was accomplished with the use of a "pushing laser" located between the collimation slits. Because of the required frequency stability, we locked the laser frequency to our atomic beam.

The laser lock

The laser locking system is the same as described in Phil Gould's thesis [GOU79], but it has been many years since the system has been used, so I will briefly describe it here. The laser we used for these experiments was a Coherent model 599 standing wave laser operating at 589.2 nm. The light is transported to the experiment with a single mode polarization preserving fiber. A schematic of the optics outside the machine are shown in Figure 8.1.

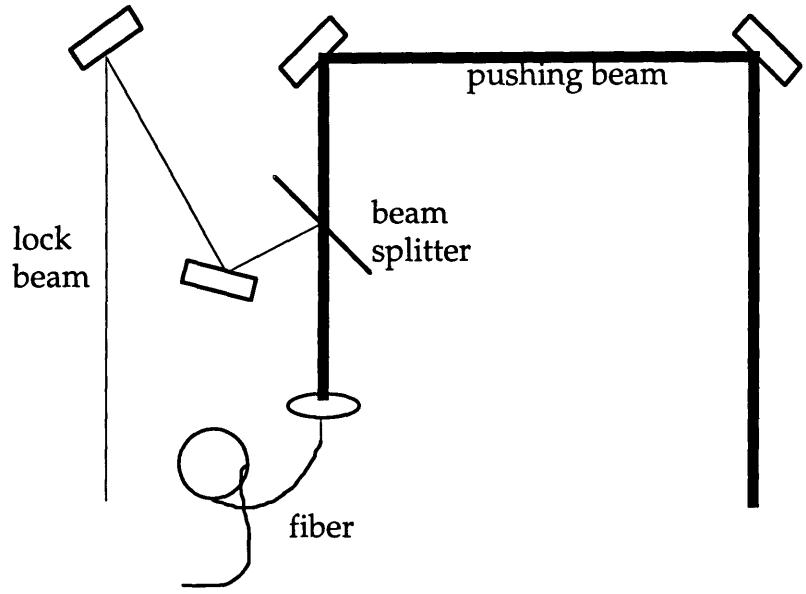

Figure 8.1: Optical layout at the beam machine.

A small portion of the laser beam is split off and intersects the atomic beam at right angles to the nominal beam direction (Figure 8.2). The intersection occurs after the beam skimmer, and before the first collimation slit where the beam still has a large angular divergence. This large angular divergence from a relatively small source means that the transverse velocity of an atom is correlated with its transverse position.

The laser frequency that a given atom sees is changed by the Doppler shift, which is the portion of the atomic velocity along the laser beam multiplied by the wave vector of the laser light. This shift coupled with the correlation of atomic position and transverse velocity means that for a given laser frequency, only one transverse position along the laser beam will have atoms that are in resonance, and are scattering light.

This fluorescence is imaged onto a split photodiode that is located above the atomic beam and has the two diodes oriented along the laser beam direction. The imaging system and photodiode can be translated along the laser beam, allowing the selection of a given frequency shift from the free space atomic frequency.

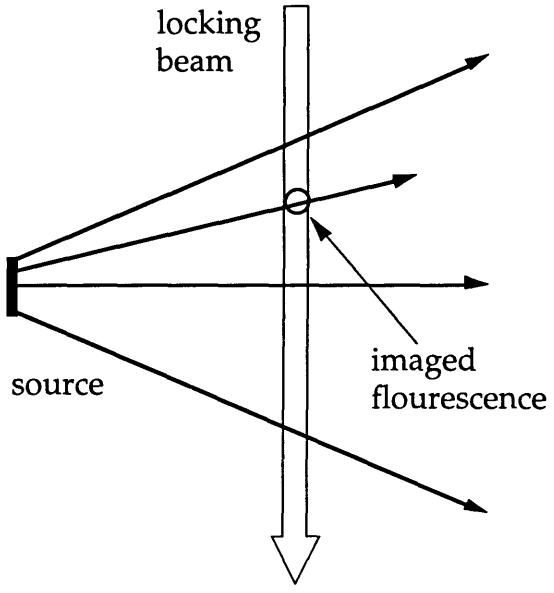

Figure 8.2: The fluorescence laser locking system. The area of imaged fluorescence is collected onto the split photodiode located above the page. The location of the imaged region can be translated along the laser beam, changing the Doppler shift.

The difference of the split photodiode signal is filtered with a low pass filter and fed back to the laser to complete a lock loop. By using the difference signal, the sensitivity to stray light, laser intensity fluctuations, and atomic beam fluctuations, is greatly reduced. This difference signal produces a dispersion line shape, making the lock easy to implement.

We lock to the stretched state transition, F=2 to $P_{3/2}$,F'=3. The laser has 1.713 GHz sidebands that are created with a resonant electro-optical modulator. This frequency makes the repumping resonant with the F=1 to $P_{3/2}$,F'=2 transition. When we scan this laser across the two ground state hyperfine state, we see four lines which are shown in Figure 8.3.

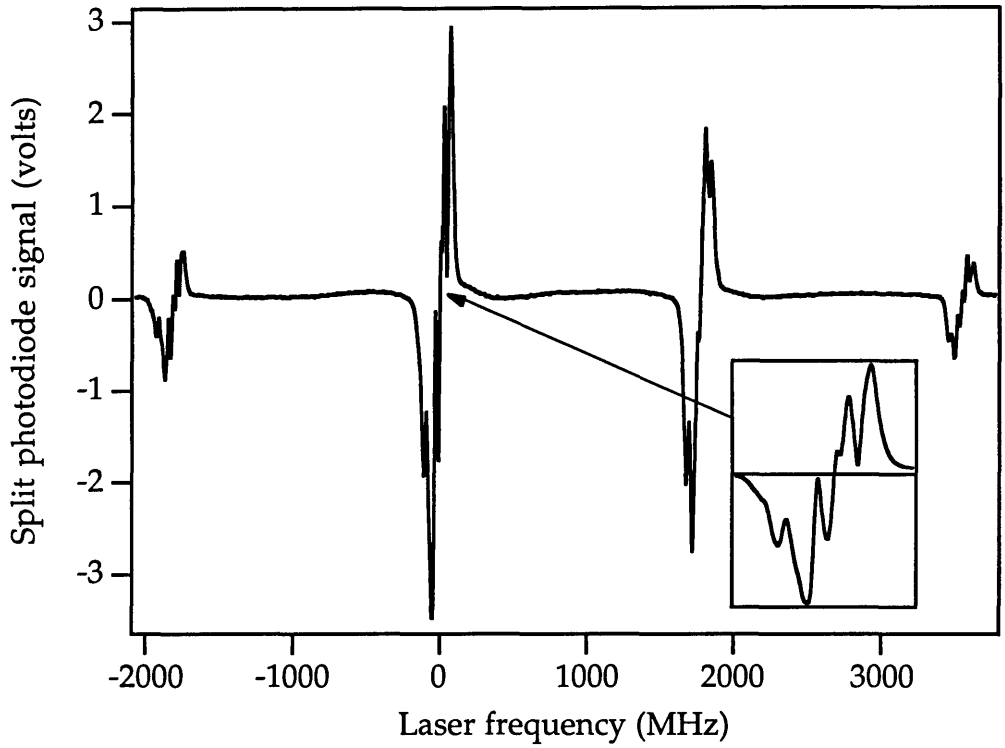

Figure 8.3: Signal from the split photodiode after amplification. The laser is scanned across the two hyperfine levels of the ground state, which are separated by 1.77 GHz. The structure inside the lines is from the hyperfine structure of the P3/2 upper state. The inset shows the structure of the largest line.

The pushing laser

The atoms are removed from the beam with resonant light forces. The atoms absorb photons and the associated momentum from a "pushing laser beam". The spontaneous emission of the atoms averages to zero net momentum change, so the atoms are shoved to the side by the laser (Figure 8.4). The molecules have no strong optical transition at the same frequency as the sodium atoms, so they are not shoved out of the beam. The pushing laser intercepts the atomic beam between the two collimation slits.

In addition, there is a knife edge formed be a razor blade mounted on a translation stage directly before the laser beam. This knife edge prevents sodium atoms from being shoved so that they make it through the second slit. Even though these atoms will have the wrong transverse momentum to make it to the detector on the beam line, if there is a diffraction grating directly after the second collimation slit, the atoms will be diffracted back into the beam line, complicating the interpretation of our diffraction data.

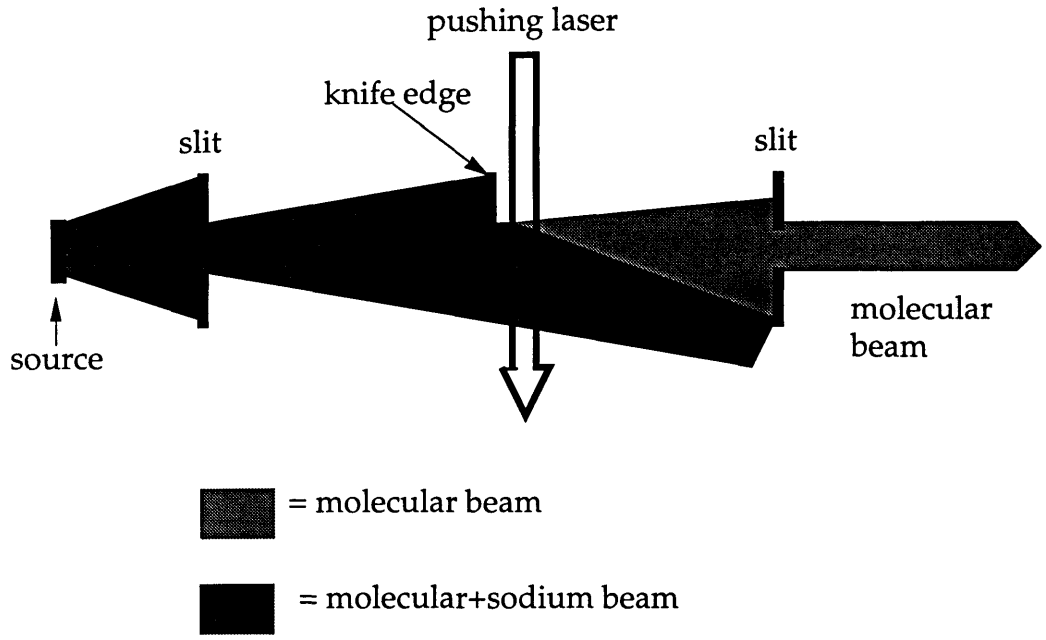

Figure 8.4: Removal of the sodium atoms from the beam. The pushing laser imparts a transverse momentum to the sodium atoms, which fail to arrive at the second collimation slit.

8.2 Diffraction of molecules

One beauty of amplitude diffraction gratings is that the really don't care what type of particles they are diffracting (providing the particles will fit through the slots). Therefore, we are in a position to extend our matter wave optics and interferometry to molecules.

The molecules in a seeded supersonic beam have nearly the same velocity as the sodium, so they have twice the deBroglie wavelength, and half the diffraction angle. This would yield a separation of the diffracted orders at the detector plane that is roughly the same size as our detected beam width. In order to increase their diffraction angle we have changed the carrier gas in the source, and decreased the period of the diffraction gratings.

The velocity of the beam should be given approximately by $\sqrt{5kT/m_{carrier}}$, where $m_{carrier}$ is the mass of the carrier gas. By using krypton as the carrier gas, we were able to slow the mean velocity down to 750 m/s from the 1000 m/s we get with argon, agreeing closely with the square root of the carrier gas mass difference. This gives us 4/3 as much diffraction angle as we get with the argon carrier gas.

We have performed the molecular diffraction experiment with 200, 140, and 100 nm period diffraction gratings, and krypton as well as argon as a carrier gas. All that I will discuss here is the data from the 100 nm period gratings, because it is the most impressive. The separation of the diffracted orders of the sodium atoms is so wide with the 100 nm period gratings that we can see the molecules appearing as peaks between the diffracted atomic beams (Figure 8.5). We fit this type of pattern by adding a molecular diffraction pattern to the atomic pattern in our fitting function.

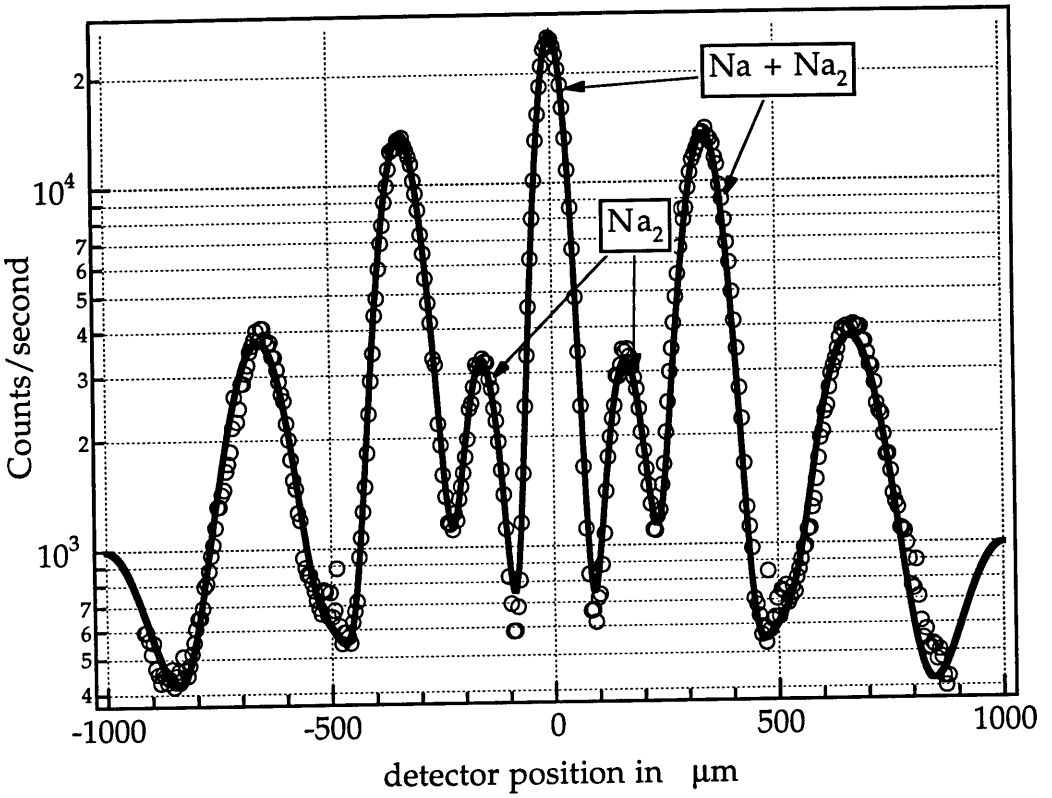

Figure 8.5: Diffraction of sodium and sodium dimers by a 100 nm period diffraction grating. The fit indicates 16.5% of the intensity is molecules.

There is one danger in identifying the small peaks with half the diffraction angle as molecules. The same sort of structure could be produced by irregularities in the grating that have twice the nominal grating period, as has been observed due to the grating bars collapsing against each other in pairs [KSS88]. This failure mode is common in weak gratings.

In order to make sure that the small peaks were only sodium dimers, we took the data in Figure 8.5 and then immediately afterwards turned on the

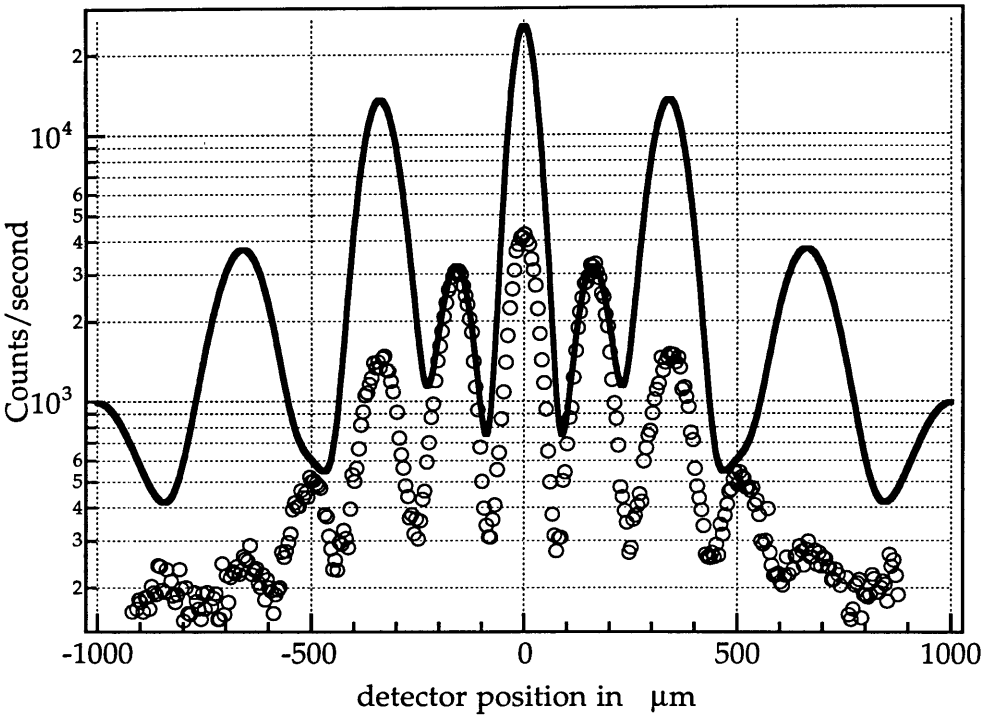

Figure 8.6a: Diffraction with only the molecules remaining in the beam when the pushing laser turned on. The fit is the same as in Figure 8.4, indicating that the small orders were entirely molecules.

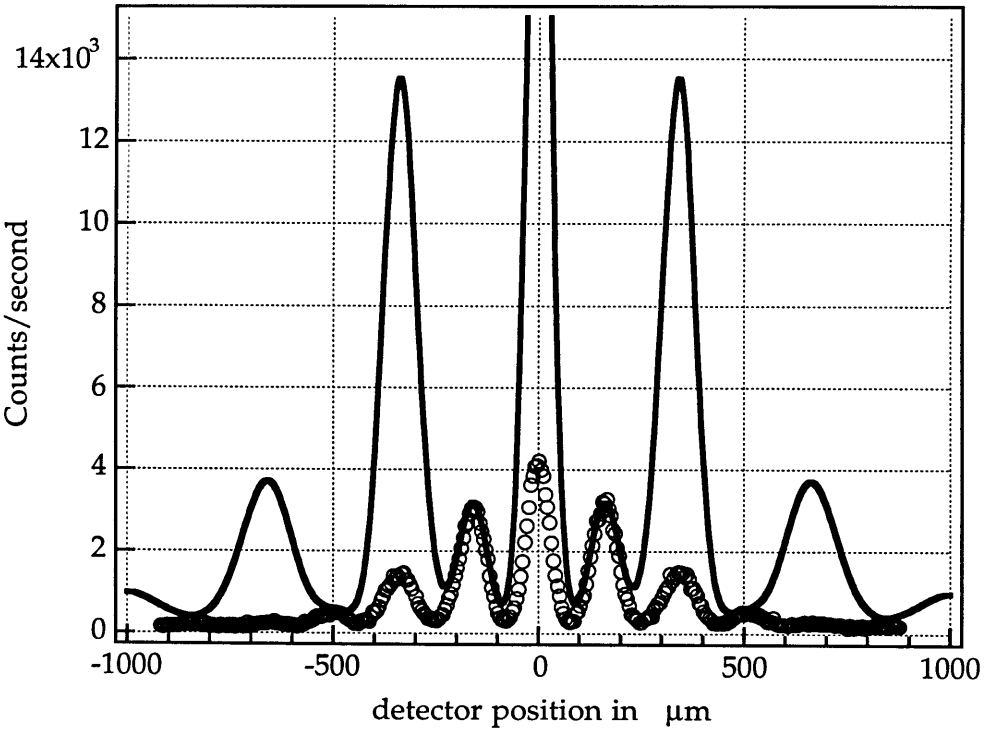

Figure 8.6b: The same data as Figure 8.5a on a linear scale.

pushing laser beam. This removed only the sodium atoms, and resulted in the data shown in Figures 8.6a and 8.6b. These figures also includes the fit from Figure 8.5, showing that the small peaks were entirely molecules.

8.3 Relative velocity of the monomers and dimers, dimer fraction

By fitting the diffraction patterns that contain both sodium monomers and dimers like the one shown in Figure 8.4, we can investigate the relative velocities of the two constituents. Any amount that the velocities are different represent different behaviors in the supersonic expansion. This is called a velocity slip for the entrained species. We see indications of velocity slip that increases with decreasing carrier gas pressure. This data is shown in Figure 8.7.

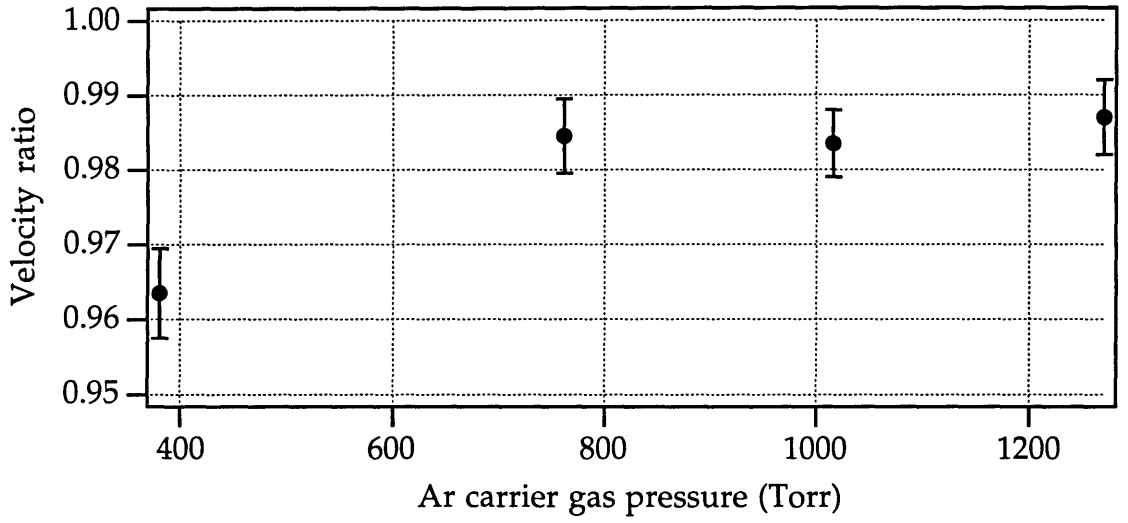

Figure 8.7: The ratio of the dimer velocity to the monomer velocity in our beam as a function of carrier gas pressure. The dimers show significant velocity slip at low source pressure.

We have also looked at the fraction of dimers in the beam as a function of source temperature. The data we have is preliminary, but show a definite enhancement of the dimer fraction with increasing source temperature, increasing source pressure, and decreasing temperature difference between the nozzle and reservoir in the source. The data shown in Figure 8.8 shown the fraction of dimers (by recorded intensity) in our beam as a function of the mean of the reservoir and nozzle temperatures. This data is complicated by the fact that the mean temperature is correlated with a decreasing temperature difference between the reservoir and nozzle.

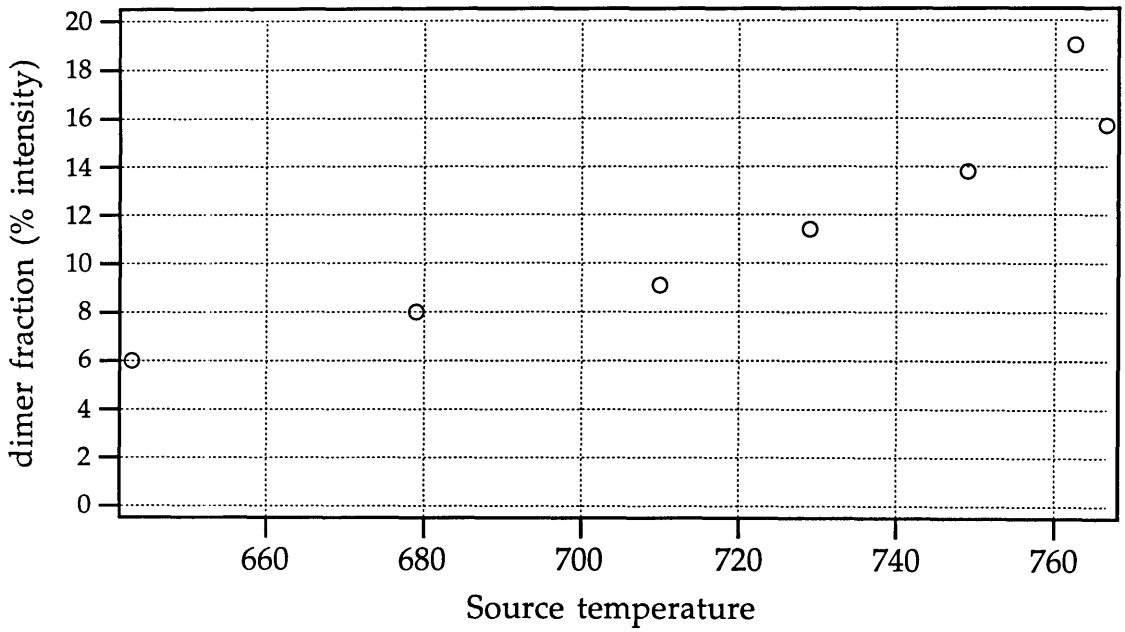

Figure 8.8: Fraction of dimers (by detected intensity) in our beam versus nominal source temperature. The temperature is the mean of the nozzle and reservoir temperatures.

8.4 Do we get one or two counts on the detector?

An interesting question at this point is how many counts are registered on our detector for each sodium dimer. If the sodium dimers ionize and are ejected as ionized molecules, we should see one count. It we are seeing a sodium ion the question is whether the other sodium atom is ejected as a neutral or an ion, giving two counts per molecule with a short time delay between counts.

To investigate this, we have built a system to analyze the spectrum of time delays between count arrivals. For single atoms that are arriving randomly at a constant rate, the distribution of delays between counts will follow a exponential decay as a function of delay time. The decay constant will be the inverse of the mean count rate. This results from integrating a constant probability per unit time for when the next count arrives.

To record the distribution of time delays between count arrivals, we start a timer when an atom arrives, turn it off when the next atom arrives, and then read out the result of the timer. We implement this by generating a gate signal and then send it to a counter on one of the computer data acquisition boards. This gate signal has a length that is the time between two successive counts. The digital circuit for generating this gate is shown in Figure 8.9.

This circuit is just a divide by two counter that counts 0, 1, 0, and then disables itself on the trailing edge of the second pulse, until the reset line is pulsed. After gating the counter in the computer with the output of this circuit, we make the time to digital conversion by reading out the counter and multiplying by the counting time base.

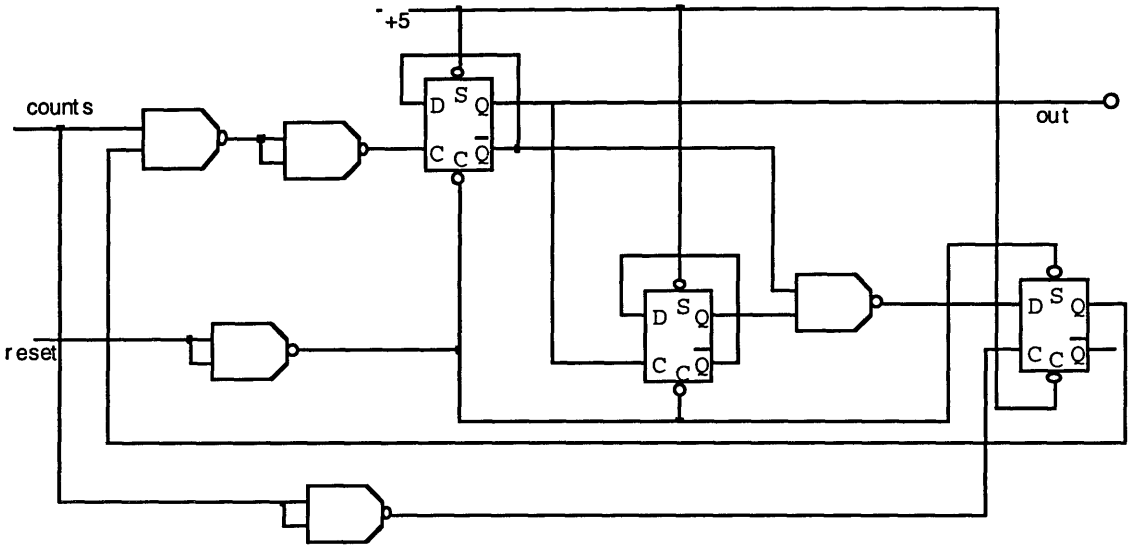

Figure 8.9: The digital circuit for producing a gate that has the length between two successive count arrivals.

Figure 8.10 shows the distribution of time delays that we see from the background count rate from the hot wire detector. The data in the figure were taken with a background count rate of 120 count per second, and the decay constant of the exponential in the fit agrees with this count rate. We do not understand the large number of count delays at 0.4 milliseconds. This feature is reproducible and only appears when there is no atomic or molecular beam striking the detector. We have checked for ringing on the detector signal line, that could produce such a feature, and have found none.

When we study the spectrum of time delays when we have sodium dimers striking the detector, we see two new features, shown in Figure 8.11. The first is an exponential decay that matches our constant count rate of 240 counts per second. The second feature is a steeper decay at short time delays. We attribute this to two sodium ions being produced from a single sodium dimer, and infer that the time constant of the decay reflects the time response of the detector wire. The additional area under the second feature is about 4%. Unfortunately, to assign the different features with confidence, we should

have a mass filter on our detector to discriminate between sodium ions, dimer ions, and other ions from the background.

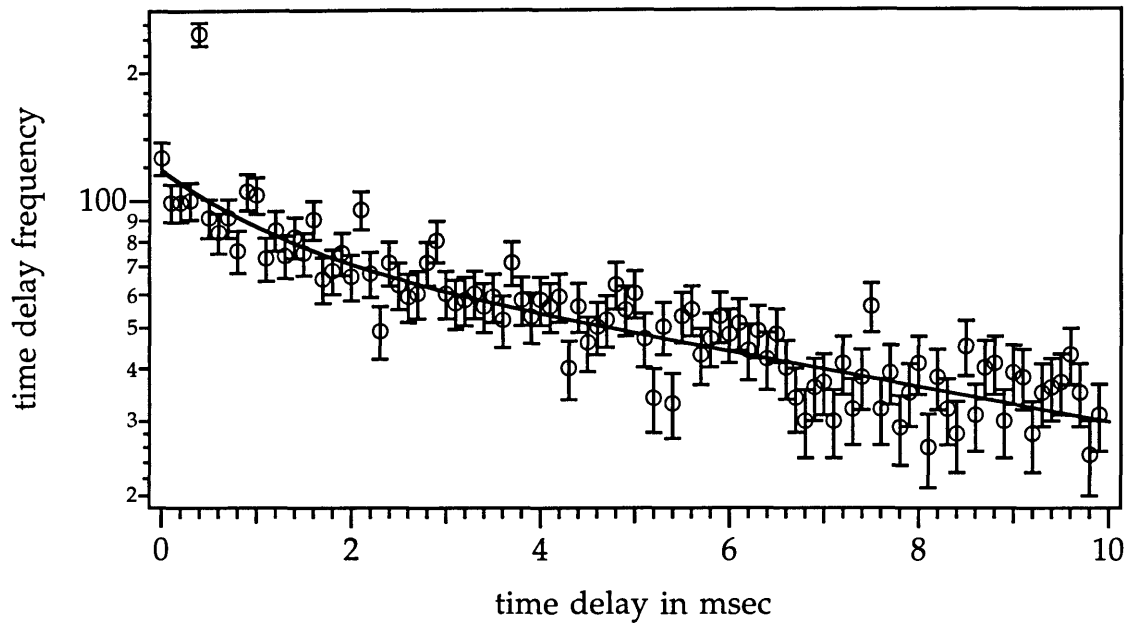

Figure 8.10: Distribution of delays between successive counts from the hot wire detector's background.

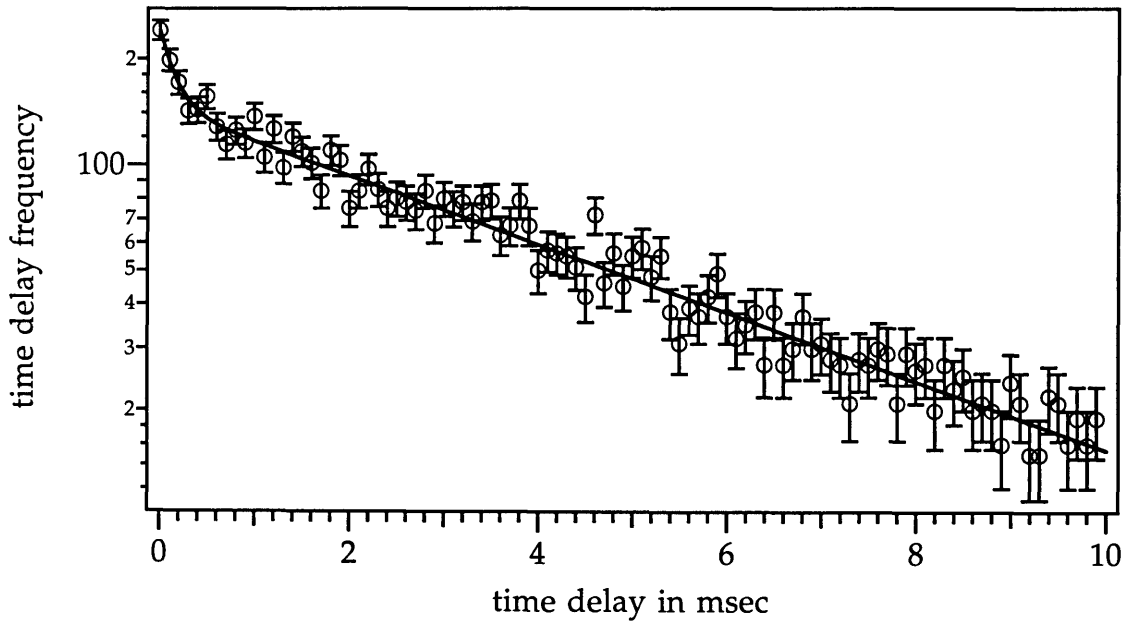

Figure 8.11: Distribution of delays between successive counts from the molecular beam. Note the increased probability of short time delays.

9 Future experiments

This chapter is a short list of experiments that the interferometer is well suited for. All of the experiments except for the investigation into molecular polarizabilities are in various stages of preparation.

9.1 The Aharonov-Casher phase shift

There has been a lot of interest recently in a phase shift proposed by Aharonov and Casher [AHC84], which is similar in flavor to the Aharonov-Bohm effect [AHB59]. This phase shift occurs when a neutral particle with a magnetic moment passes through an electric field. An experimental investigation of this phase shift was carried out with a neutron interferometer and an unpolarized neutron beam [COK89].

The existence of this phase shift can be seen from a Lorentz transformation. If the particle moving through an electric field E with a velocity v, it will see a magnetic field in its rest frame that is proportional to vE/c. The magnetic moment will interact with the magnetic field, producing a phase shift. This phase shift will be proportional to velocity, so as discussed in section 3.4, if the interaction is applied for a given length in the interferometer, the phase shift will be independent of velocity. For certain orientations of the dipole, there will be no classical force on the particle [ANA89].

We plan to perform the experiment with an optically pumped beam of sodium atoms in our interferometer. The atomic beam will be optically pumped with the beam that plays the role of the "locking beam" in the molecular beam preparation described in section 8.1. Magnetic guide fields will define the direction of the optically pumped atoms through the interferometer and interaction region.

The interaction region will have the same design as used for the polarizability measurement, and is shown in Figure 4.2. The septum will be held at a large voltage, and the side plates will be grounded. The electric fields will be directed in opposite directions in either beam of the interferometer, producing a net phase shift between the beams. There will also be a large amount of phase shift from the Stark shift that will be the same for each beam to within how well we can balance the two sides of the interaction region.

An applied voltage of 5 kV on the septum will produce a 1 radian phase shift in the interferometer when we change the sign of the voltage. We will also be able to change the direction of the dipole (the optically pumped atom) with respect to the interaction region fields. This will allow us another systematic reversal, and the opportunity to test the directional dependence of the interaction. It appears that a 10% measurement of the magnitude and angular dependence of the phase shift should be realizable.

9.2 Berry's phase

Another possible experiment is the explicit measurement of the Berry phase [BER84] of the wave function of the sodium beam. We will apply three magnetic fields at the interaction region. The first is a bias field that is directed along the y axis (across the interferometer). The second is the septum magnetic field the arises from passing a current down the septum, through the interferometer. This field is the same as used in the magnetic rephasing experiment described in chapter 5. The third field is produced by a screw winding around the interaction region that produces a field in the x-y plane (across the interferometer) that rotates once along the interaction region.

This combination of fields will produce total magnetic phase shifts that are the same for both beams. If the atoms follow the fields, however, they will traverse paths in angle that have different solid angles, yielding a phase shift

$$\Delta\varphi_{geometric} = m_F \Delta\Omega_{evolution}$$

where $\Delta\Omega_{evolution}$ is the difference in the solid angles of the paths swept out by the magnetic field on the two sides of the interferometer.

A key feature of this arrangement of fields is that there is no Berry phase for combinations of the magnetic fields that do not include both the septum and screw fields. This will allow us to separate out any phase shifts from mis-

matching of the lengths of the field vectors on either side. The solid angle difference can be varied by changing the relative size of the field components. The dependence of the phase on magnetic moment projection can be tested by optically pumping the beam into different Zeeman states, including one with no projection along the field axis.

9.3 Inertial sensitivities

The interferometer is an accelerometer. Accelerations cause the gratings to appear at different transverse positions when the atoms arrive. The phase shift from a transverse acceleration is

$$\Delta\varphi = \left[\frac{2\pi\tau^2}{p}\right]a$$

where the transit time between gratings is τ and p is the grating period. This gives a one radian phase shift for 0.09 m/s^2.

The interferometer is also a very sensitive gyroscope. This sensitivity to rotations is just the response to the Coriolis acceleration. With work to deal with long term drifts, the current version of the interferometer should be able to demonstrate a sensitivity of approximately $2x10^{-7}$ radians/second ($2x10^{-3}$ Earth's rate) in one hour of integration time.

9.4 Molecular interference

A straightforward extension of the molecular diffraction experiment described in chapter 8 is the demonstration of a molecular interferometer. The same molecular beam preparation techniques would be used along with three of the diffraction gratings. All of the infrastructure that has been built up for the atom interferometer could be used for realization of a molecular interferometer.

One slight difficulty with this experiment would be the fact that there would be no clear signature in the interference pattern that molecules instead of atoms were the interfering particles. This could be addressed by interacting with the split beams inside the interferometer with some laser light that is resonant with the atoms. This could be split off of the pushing laser beam. By demonstrating that this destroyed the interference pattern in the interferometer containing only atoms it would be clear that when the

interference pattern did not degrade that the interfering particles are molecules.

9.5 Molecular polarizabilities

A first application of a molecular interferometer could be a measurement of the tensor electric polarizability of the sodium dimer. The same style of interaction region as was used in the sodium polarizability measurement could by used.

The sodium dimer has an electric polarizability that is roughly the same size as the sodium atom, but is different by a factor of two for fields applied in the plane of the molecule versus out of plane. A first generation experiment without any further modifications would measure the average of the in plane and out of plane polarizabilities. Later generations of the experiment would select the rotational state and orientation of the molecule to measure the independent components. It may be possible to employ the different phase shifts applied to molecules in different states in an experiment where the contrast of the interference pattern is modulated. This would be very similar to the magnetic rephasing experiment described in chapter 5.

References

[AHB59] Aharonov, Y., D. Bohm, "Significance of Electromagnetic Potentials in the Quantum Theory",*Phys. Rev.* **115**, 485 (1959).

[AHC84] Aharonov, Y., A. Casher, "Topological Quantum Effects for Neutral Particles",*Phys. Rev. Lett.* **53**, 319 (1984).

[ANA89] Anandan, J., Interactionof a Dipole with the Electromagnetic Field: Quantum Interference, Classical Limit, and Field Equations, 3rd Int. Symp. Foundations of Quantum Mechanics Tokyo, 1989), pp. 98.

[BER84] Berry, M. V., *Proc. Roy. Soc. A* **392**, 45 (1984).

[CAL75] Chang, B. J., R. Alferness, E. N. Leith, "Space-invariant achromatic grating interferometers: theory",*Applied Optics* **14**, 1592 (1975).

[CAM91] Carnal, O., J. Mlynek, "Young's double slit experiment with atoms: A simple atom interferometer",*Phys. Rev. Lett.* **66**, 2689 (1991).

[CLA92] Personal communication with John Clauser

[CLR92] Clauser, J. F., M. reinsch, "New Theoretical and Experimental Results in Fresnel Optics wiht Applications to Matter-Wave and X-Ray Interferometry",*App. Phys. B* **54**, 380 (1992).

[COK89] Cimmino, A., et al., "Observation of the Topological Aharonov-Casher Phase Shift by Neutron Interferometry",*Phys. Rev. Lett.* **63**, 380-383 (1989).

[COW75] Colella, R., A. W. Overhauser, S. A. Werner, "Observation of Gravitationally Induced Quantum Interference",*Phys. Rev. Lett.* **34**, 1472 (1975).

[DFS72] Düren, R., A. Frick, C. Schlier, "Glory undulations of some alkali-molecule systems",*J. Phys. B* **5**, 1744 (1972).

[DRS68] Düren, R., G. P. Raabe, C. Schlier, "Exact Potential from Scattering Measurements: Alkali-Rare Gas Systems",*Z. Phys.* **214**, 410 (1968).

[EKP92] Ekstrom, C. R., D. W. Keith, D. E. Pritchard, "Atom Optics Using Microfabricated Structures",*App. Phys. B* **54**, 369 (1992).

[ERT93] Personal communication with W. Ertmer

[ESS30] Estermann, I., O. Stern, "Diffraction of Molecular Beams",*Z. Phys.* **61**, 95 (1930).

[FAP99] Fabry, C., A. Perot, *Ann. Chim. Phys.* **16**, 115 (1899).

[FIZ62] Fizeau, H., *Ann. Chim. Phys.* **66**, 429 (1862).

[GAL81] Gottscho, R. A., R. Ahmad-Bitar, W. P. Lapatovich, I. Renhorn, D. E. Pritchard, "Global analysis of the NaNe eximer band systems: A molecule between Hund's cases",*J. Chem. Phys.* **75**, 2546 (1981).

[GOU79] Gould, P. L., "Momentum Transfer to Atoms by Absorption and Emission of Radiation" PhD, MIT (1979).

[HAZ74] Hall, W. D., J. C. Zorn, "Measurement of alkali-metal polarizabilities by deflection of a velocity-selected atomic beam",*Phys. Rev. A* **10**, 1141 (1974).

[KAC91] Kasevich, M., S. Chu, "Atomic Interferometry using Stimulated Raman Transitions",*Phys. Rev. Lett.* **67**, 181 (1991).

[KAS92] Kasevich, M. A., "Atom Interferometry in an Atomic Fountain" PhD, Stanford (1992).

[KEI91] Keith, D. W., "An Interferometer for Atoms" PhD, MIT (1991).

[KET91] Keith, D. W., C. R. Ekstrom, Q. A. Turchette, D. E. Pritchard, "An Interferometer For Atoms",*Phys. Rev. Lett.* **66**, 2693 (1991).

[KOH83] Klein, A. G., G. I. Opat, W. A. Hamilton, "longitudinal Coherence in Neutron Interferometry",*Phys. Rev. Lett.* **50**, 563 (1983).

[KSS88] Keith, D. W., M. L. Shattenburg, H. I. Smith, D. E. Pritchard, "Diffraction of Atoms by a Transmission Grating",*Phys. Rev. Lett.* **61**, 1580 (1988).

[KWG83] Kaiser, H., S. A. Werner, E. A. George, "Direct Measurement of the Lontgitudinal Coherence Length of a Thermal Neutron Beam",*Phys. Rev. Lett.* **50**, 560 (1983).

[KWR91] Kasevich, M., et al., "Atomic Velocity Selection Using Stimulated Raman Transitions",*Phys. Rev. Lett.* **66**, 2297 (1991).

[LAU48] Lau, E., *Ann. Phys.* **6**, 417 (1948).

[MAC92] Mach, L., *Zeitschr. f. Instrkde* **12**, 89 (1892).

[MAS62] Maier-Leibnitz, H., T. Springer, "An Interferometer for Slow Neutrons",*Z. Phys.* **167**, 386 (1962).

[MIB78] Miller, T. M., B. Bederson, "Atomic and Molecular Polarizabilities-A Review of Recent Advances" in *Advances in Atomic and Molecular Physics*(Academic Press, 1978), vol. 13, pp. 1-55.

[MIB88] Miller, T. M., B. Bederson, "Electric Dipole Polarizability Measurements" in *Advances in Atomic and Molecular Physics*(Academic Press, 1988), vol. 25-60, pp. 37.

[MIC82] Michelson, A. A., "Interference Phenonena in a new Form of Refractometer",*Phil. Mag.* **13**, 236 (1882).

[MIM87] Michelson, A. A., E. W. Morley, *Phil. Mag.* **24**, 449 (1887).

[MOD54] Mollenstedt, G., H. Duker, "Frensnelscher interferenzversuch mit einem Biprisma fur ekektronenwellen",*Naturwissenschaften* **42**, 41 (1954).

[MPV91] Miniatura, C., et al., "A longitudinal Stern-Gerlach interferometer: the <<beaded>> atom",*J. Phys. II* **1**, 425 (1991).

[MSM74] Molof, R. W., H. L. Schwartz, T. M. Miller, B. Bederson, "Measurements of electric polarizabilities of the alkali-metal atoms and the metastable noble-gas atoms",*Phys. Rev. A* **10**, 1131 (1974).

[MSS53] Marton, L., J. A. Simpson, J. A. Suddeth, "Electron Beam Interferometer",*Phys. Rev.* **90**, 490 (1953).

[MSS54] Marton, L., J. A. Simpson, J. A. Suddeth, "An Electron Interferometer",*Rev. Sci. Instr.* **25**, 1099 (1954).

[OHA88] O'Hanlon, J. F., *A User's Guide to Vacuum Technology* (Wiley, 1988).

[PTV92] Press, W. H., S. A. Teukolsky, W. T. Vetterling, B. P. Flannery, *Numerical Recipes in C: The Art of Scientific Computing* (Cambridge University Press, 1992).

[RAY81] Rayleigh, L., *Phil. Mag.* **11**, 196 (1881).

[RKW91] Riehle, F., T. Kisters, A. Witte, J. Helmcke, C. J. Borde', "Optical Ramsey Spectroscopy in a Rotating Frame: Sagnac Effect in a Matter-Wave Interferometer",*Phys. Rev. Lett.* **67**, 177 (1991).

[RSS93] Rieger, V., K. Sengstock, U. Sterr, J. H. Müller, W. Ertmer, "Atom-interferometric determination of the dc-Stark shift of the Mg-intercombination line",*Opt. Comm* **99**, 172 (1993).

[RTB74] Rauch, H., W. Treimer, U. Bonse, "Test of a Single Crystal Neutron Interferometer",*Phys. Lett.* **47A**, 369 (1974).

[RZB75] Rauch, H., et al., "Verification of coherent spinor rotation for fermions",*Phys. Lett.* **54A**, 425 (1975).

[SAK85] Sakurai, J. J., *Modern Quantum Mechanics* (Addison-Wesley, 1985).

[SSM92] Sterr, U., K. Sengstock, J. H. Müller, D. Bettermann, W. Ertmer, "The Magnesium Ramsey Interferometer: Applications and Prospects",*App. Phys. B* **54**, 341 (1992).

[SST92] Shimizu, F., K. Shimizu, H. Takuma, "Stark Phase Shift and Deflection in the Ultracold Atomic Interferometer",*Jpn. J. Appl. Phys.* **31**, L436 (1992).

[TAL36] Talbot, H., *Phil. Mag.* **9**, 401 (1836).

[TPK92] Turchette, Q. A., D. E. Pritchard, D. W. Keith, "Numerical model of a multiple-grating interferometer",*JOSA B* **9**, 1601 (1992).

[TUR91] Turchette, Q. A., "Numerical Model of a Three Grating Interferometer for Atoms" SB, MIT (1991).

[WEI93] Weiss, D. S., "A Precision Measurement fo the Photon Recoil of an Atom using Atomic Interferometery" PhD, Stanford (1993).

[WSC79] Werner, S. A., J. Staudenmann, R. Colella, "Effect of the Earths Rotation on the Quantum Mechanical phase of the Neutron",*Phys. Rev. Lett.* **42**, 1103 (1979).

[ZEN91] Zender, L., *Zeitschr. f. Instrkde* **11**, 275 (1891).

Acknowledgments

Now the time has come to thank everyone who has helped with the work in this thesis, or helped me through my graduate career.

The people who deserve the first thanks are my parents Janice and Philip Ekstrom. They have supported me in all ways and instilled in me curiosity and a love of discovery. My wife Gretchen has been a constant source of support and tolerance to the demands of the lab.

I have had the pleasure of working on the experiment with a large number of extremely competent people without whose help this work would not have happened. They are all good friends as well as co-workers. David Keith was the driving force behind the first demonstration of the atom interferometer. The experiment still bears the marks of our Led Zeppelin fueled building frenzies. Bruce Oldaker was a calming influence on me and the lab, trying to create order from the chaos. The current interferometer crew is a great group: Mike Chapman, Troy Hammond, Jörg Schmiedmayer, Richard Rubenstein, and Stefan Wehinger. All of these people have contributed to the high quality of life on the experiment, helping to make the work enjoyable and possible. I enjoyed working with you all.

The interferometer has benefited from the efforts of the many undergraduates whom I have worked with. They are: Quentin Turchette, Garth Zeglin, John Berberian, Amrit Pant, Eliot Quaterat, Richard Pengelly, and Bridget Tannian.

Dave Pritchard's lab is a great place to do physics, learn, and meet new friends. Dave has provided large amounts of guidance and taught me to quickly think through a physics problem to filter what is worth spending time thinking about or working on. I hope that I have also learned something about "taste" in experiments from his examples. He has managed to keep us all funded and surrounded with a steady stream of interesting people in a stimulating environment.

Carol Costa is our group secretary and always knows just how to get something done at MIT. Peggy Berkovitz is our wonderful graduate secretary. She seems to always make graduate life simpler.

There are two other experiments in Dave's lab that are populated with great folks. The neutral trap crowd have been good compatriots and generous with their lasers that we use in some of our experiments. Wolfgang Ketterle has been a great source of ideas and help in the lab. Kris Helmerson always had time to help someone else, and probably had a good idea about how to solve your problem. Mike Joffe is a good friend, and valuable source of practical lab techniques. The rest of the crowd have been great: Alex Martin, Michael Andrews, and Min Xiao.

The ICR gang have provided help with problems electronic, and broadened the horizons of the lab by using atoms other than sodium. I enjoyed talking about obscure physics with Vasant Natarajan, and audio with Kevin Boyce. I have enjoyed the rest of the gang as well: Frank DiFilippo, Eric Cornell, Mike Bradley, and Abe Stroock.

The friendships I have gained from the Pritchard group extend beyond people now in the lab. Warren and Debbie Moskowitz still invite crowds of Pritchard group people up to they're house for wonderful parties. Rick Stoner an Brian Stewart are great friends as well.

I have benefited from knowing and working with many of the graduate students in the Kleppner group. I must thank Robert Lutwak for lab hints, computer support, and conversations over coffee in the morning. Jeff Holley, Scott Paine, and Peter Chang, from the same experiment, were always friendly and helpful.

I must also acknowledge the rest of the Kleppner group that I have overlapped with: Mike Kash, George Welsh, Hong Jiao, Michael Courtney, Barbara Hughey, and Tom Gentile.

In closing, thanks to all of you for making my years as a graduate student something that I will be able to look back on happily and feel that it was all worth while. I would do it again because of you.